NUMERICAL STUDY OF THE DYNAMIC PROCESSES IN VOLCANIC ERUPTIONS: BUBBLE DYNAMICS AND VOLATILES DIFFUSION

A Dissertation
Presented to
The Academic Faculty

by

Yanqing Su

In Partial Fulfillment
of the Requirements for the Degree
Doctor of Philosophy in the
School of Earth and Atmospheric Sciences

Georgia Institute of Technology
May 2017

Copyright © 2017 by Yanqing Su

NUMERICAL STUDY OF THE DYNAMIC PROCESSES IN VOLCANIC ERUPTIONS: BUBBLE DYNAMICS AND VOLATILES DIFFUSION

Approved by:

Dr. Christian Huber, Advisor
School of Earth and Atmospheric Sciences
Georgia Institute of Technology

Dr. Josef Dufek
School of Earth and Atmospheric Sciences
Georgia Institute of Technology

Dr. Andrew Newman
School of Earth and Atmospheric Sciences
Georgia Institute of Technology

Dr. Zhigang Peng
School of Earth and Atmospheric Sciences
Georgia Institute of Technology

Dr. Jingfeng Wang
School of Civil and Environmental Engineering
Georgia Institute of Technology

Date Approved: March 3rd, 2017

To my family.

ACKNOWLEDGEMENTS

I thank my advisor Dr. Christian Huber, for his guidance, support and encouragement throughout my stay at Georgia Tech. I also want to express my gratitude to my committee: Dr. Josef Dufek, Dr. Andrew Newman, Dr. Zhigang Peng, and Dr. Jingfeng Wang. I am grateful to my colleagues at Georgia Tech: Dr. Babak Shafei, Dr. Caroline Bouvet de Maisonneuve, Dr. Andrea Parmigiani, Dr. Wim Degruyter, Dr. Társilo Girona, Dr. Salah Faroughi, and Hamid Ghazizadeh Karani.

I thank Leslie Hayden for assistance with electron microprobe analysis, Brad Ito and Marsha Lidzbarski for support using the Stanford-USGS SHRIMP-RG. I also thank Dr. Paul Wallace, Dr. Jacob Lowenstern and Dr. Tom Sisson, as well as Editor Dr. André Revil and Reviewer Dr. Yang Liu for their helpful comments on my journal publications.

This dissertation is based upon work primarily supported by the National Science Foundation (NSF EAR-1144957 and CAREER Grant No. 1454821). This work used Comet and Bridges on the Extreme Science and Engineering Discovery Environment (XSEDE), which is supported by National Science Foundation grant number ACI-1053575.

Finally, I thank my husband Shuozhi Xu, who have accompanied me with love during my studies, as well as my parents and my brother, who have backed me throughout the course of my PhD.

TABLE OF CONTENTS

LIST OF TABLES

LIST OF FIGURES

SUMMARY

Volcanic eruption releases gases and aerosols (e.g., sulfur compounds) to the atmosphere, impacting climate for up to several years. While most research efforts of volcanologists to date have been devoted to unraveling the eruptive activity and formation of volcanoes, the understanding of volatiles diffusion during volcanic eruption is still preliminary, largely due to the lack of robust computational tools for magma dynamics during volcanic eruption at the necessary time and length scales. On the other hand, magmatic processes, from the production of melts in the upper mantle to their crystallization or eruption at the surface, are dominated by dynamic processes in deep Earth that are not directly observable, limiting the direct measurement of these processes through geological fieldwork. This dissertation includes three main parts: (i) a non-equilibrium bubble growth models are developed to assess the role of bubble dynamics and volatile kinetics in "excess sulfur" problem (Chap. 2) and the implication of the volatile diffusion profile after eruptions on magma ascent history (Chap. 3); (ii) a new bubble dynamics model that accounts for hydrodynamical interactions (deformation, coalescence) between bubbles are established (Chap. 4); (iii) the dynamical response of saturated porous media to transient stresses is studied using the lattice Boltzmann method with four different porous media topologies (Chap. 5). It is anticipated that the findings in this dissertation will improve physical understanding of volatile degassing, bubble dynamics, and saturated porous media in response to transient changes of stresses.

CHAPTER I

INTRODUCTION

1.1 Motivation

Volcanic eruptions can be extremely hazardous, and a single explosive volcanic eruption can cause catastrophic destruction of life and property. Volatiles can be the direct causes of some of the hazards, e.g., the global temperature drop and regional temperature anomalies after Mt. Pinatubo eruption in 1991 [58] and the 1600 AD Huaynaputina eruption in Peru [35], and several large atmospheric and agriculturic pollution episodes after the eruption of Laki from 1783 to 1984.

Many volcano observatories worldwide measure volcanic plume emissions as part of their operational monitoring efforts. As "telegrams from Earth's interior" [164], studying volatile can aid in forecasting and understanding of volcanic unrest.

In this dissertation, the focus is placed on how volatiles species partition between melt, crystals and gas bubbles under various conditions (during storage of magma at shallow depth or ascent to the surface) and how volatile degassing impacts eruptions. In this chapter, I will introduce the role of volatiles in volcanic eruptions as well as the most abundant volatile species involved, and present an overview on various measurement and detection methods. The climatic impact from volcanic eruptions due to degassing of SO_2 is also briefly mentioned. The central questions addressed in the dissertation and its structure are discussed at the end of the chapter.

1.1.1 Volatiles in volcanic eruptions

Magma, initially formed by partial melting of upwelling mantle materials, is a mixture of solids, melts, and volatiles. The mechanical and chemical interactions between these phases control the physical and chemical evolution of magmas as they transit through the crust. Among these phases, volatiles are of great importance in volcanic eruptions as they provide the driving force for magma ascent and eruption. The abundances of volatile species in the

primordial melts is controlled by the tectonic environment (subduction, extension, etc.).

In the environment of subduction zone, volatiles are produced by dehydration of subducting slab as shown in Fig. 1.1 [222]. Upon subducting, the slab can lose free water through porous sedimenets when the temperature is higher and reaching 200–400 °C. Then, the volatile (dominantly aqueous H_2O) that is being expelled can be added to the fore-arc mantle and to hydrate the fore-arc mantle via the breakdown of serpentine minterals (storage of hydrous phase). The hydrated mantle then rises upward due to the corner flow advection caused by subducting slab, and volatiles can be exsolved when their concentration equals the volatiles concentration, and further volatiles can be degassed into the atmosphere in volcanic eruptions [222].

Volatile species tend to be incompatible with crystal phases and hence remain mostly dissolved in the melt until they reach saturation and start to exsolve (deeper for CO_2 compared to water). After degassing and expulsion from their magma host, these volatiles species are cycled back to the atmosphere [89].

Volatile degassing fundamentally controls volcanic eruption magnitudes and styles by affecting the magma viscosity, buoyancy, and compressibility. [56, 59, 191, 207]. The melt viscosity mainly depends on composition, temperature and dissolved water content, as the latter controls the degree of polymerization in the melt [175]. The stress applied by decompressing bubbles on the surrounding melt can also lead to melt fragmentation, a condition for explosive eruptions [223]. Studying the fate of volatiles during exsolution is therefore a central goal of physical volcanology.

Volcanic eruptions are rich in various types of volatiles, including H_2O, CO_2, SO_2, H_2S, nitrogen, chlorine, fluoride, and noble gases (He, Ar, Ne, Kr, Xe) [59,191,207]. Their abundance varies in different types of magma. Some of these species can have an effect on climate once released to the atmosphere and some are toxic to life. Dissolved volatile concentrations in magmas are typically estimated by analysis of melt inclusions. Melt inclusions (MIs) are tiny beads of silicate melt trapped in phenocrysts during crystal growth. Their composition is assumed to represent that of the silicate melts at the time of entrapment. Erupted magmas lose their volatiles because of degassing during eruption, but silicate melt

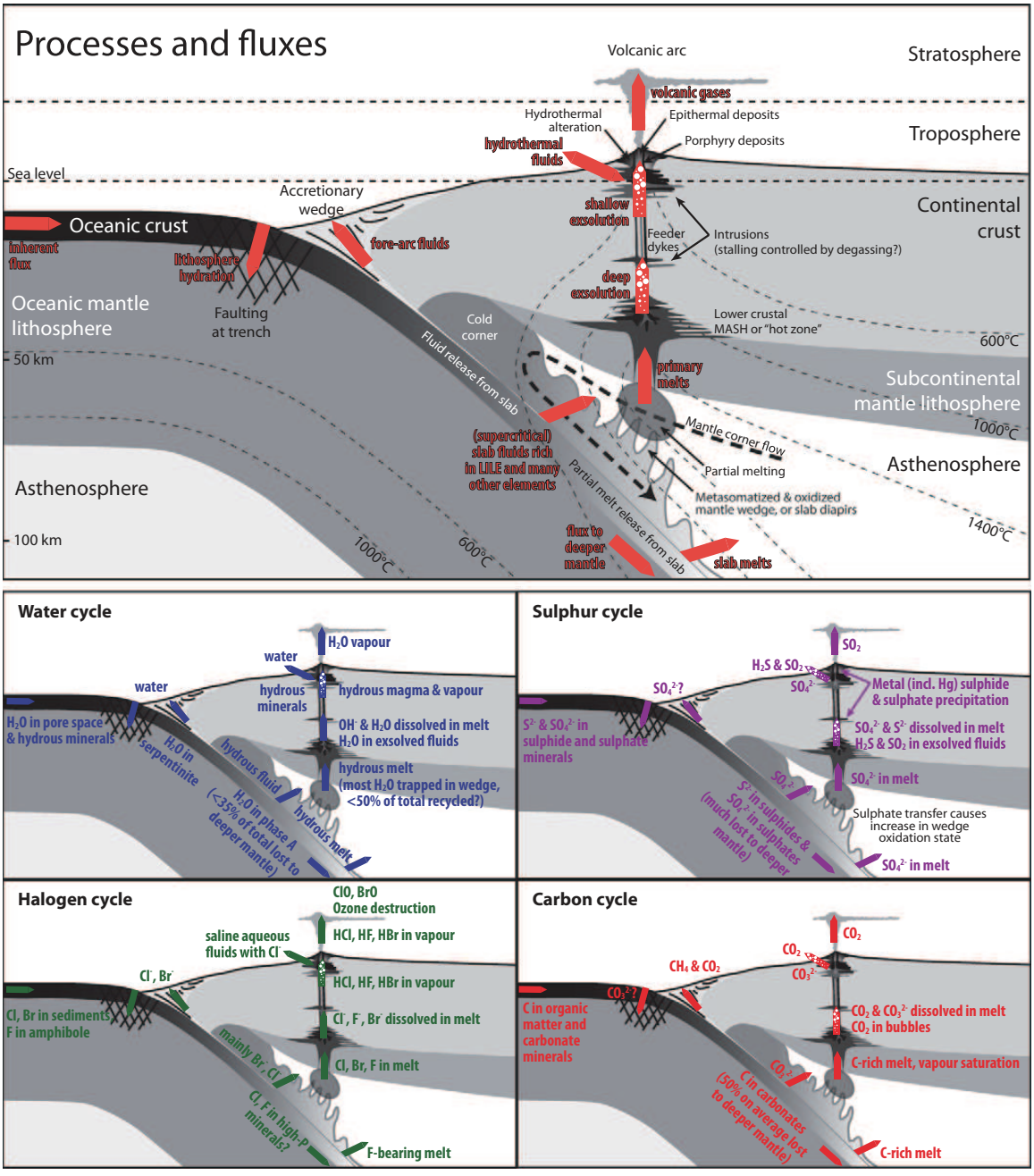

Figure 1.1: Volatile cycling in subduction zone (Fig. 1 in Ref. [222]).

inclusions can maintain their original dissolved volatile concentrations because their rigid host crystal serves as a pressure vessel during decompression. In this section, I will present some facts about H_2O, CO_2, SO_2, which are the volatiles that I have studied or will study in the future.

1.1.1.1 H_2O

H_2O is the primary volatile species in most magmas [207]. One can trace the source of water within magmas by measuring the oxygen isotopic composition of these magmas. It was found that water in subduction zone magmas is mostly related to the dehydration of the downgoing slab, while it may involve recycling and deep storage within the mantle for hot spots volcanism [174, 185, 192]. Water is structurally bound to the aluminosilicate networks in the form of OH^- groups or as H_2O molecules when dissolved in the melt [123]. From many MIs (melt inclusions) sampled from different magmas, water concentration in melt phase span a range from below 1 wt.% to above 10 wt.% with the highest water concentration measured in arcs. For rhyolitic magmas, the water concentration is typically 3–7 wt.%. For basaltic magma, the value is lower, 0.2–1 wt.% for OIBS (ocenanic island basalts) and < 0.4–0.5 wt.% for MORBS (mid-ocean ridge basalts) [39]. The gas saturation curves for basalt and rhyolite at different depths are shown in Fig. 1.2. Water saturation depends on the melt composition and pressure. For rhyolitic magma, its saturation depth is 1 kbar to 2.5 kbar; for basaltic magma, it is 2 to 5 kbar. Hence, melts tend to be saturated with water at shallow pressure in arcs [207]. Once the water concentration exceeds its solubility (either because of decompression or crystallization), bubbles nucleate once a finite activation energy is overcome.

H_2O exerts a first order control on bubble growth dynamics due to the fact that it is the fastest diffusing major volatile species in silicate melts [224]. H_2O influences bubble growth in another way by affecting melt viscosity. By adding 2 wt.% H_2O into originally H_2O free magma, the magma viscosity can drop off by several orders of magnitude according to Giordano et al. [60].

1.1.1.2 CO_2

As the second most abundant species dissolved in magmas, the CO_2 content in the mantle is estimated to be 180 $\sim$ 1100 ppm [165], which makes the mantle the largest reservoir of carbon on the Earth [33]. It dissolved in the melt as molecular CO_2 (in rhyolite) and CO_3^{2-} (in basalt) or both species (in andesite and dacite) [43]. For silicic magmas, the melt concentration in CO_2 is quite low and often below detection limits. For basaltic magma, CO_2 is relatively abundant with 50–400 ppm for MORBs and 2000–6500 ppm for OIBs [135]. Due to the much lower solubility of CO_2 as compared to H_2O (Fig. 1.2), arc basalt can be sautrated with CO_2 at greater crustal depths [3]. Wallace [207] suggested that the CO_2 content in basaltic magma could be used to infer the initial volatile saturation depth of magma if the saturation pressure < 5 kbar, because little is known about the solubility of CO_2 at pressure > 5 kbar.

1.1.1.3 Sulfur

SO_2 is often considered the third most abundant volatile species released during volcanic eruptions. Considerable work has been done with sulfur due to its role on on atmospheric radiative balance and climate after large explosive eruptions [168,177] and on the formation of ore deposits [135]. For silicic magma, the S concentration in the melt is typically below 200 ppm. For basaltic magma, the value is higher with 80–1500 ppm for MORBs and 2000–6500 ppm for OIBs [135]. Sulfur speciates in the melt mostly under the form of S^{2-} or SO_4^{-2} [88,212]. Correspondingly, the dominant vapour phases are H_2S and SO_2 [25]. Unlike H_2O and CO_2, the system redox state can alter the relative abundance of these two species. The concentration of sulfur ranges typically from $\sim$ 1000 ppm to $\sim$ 40 ppm considering magmas with S_iO_2 contents ranging from 45 to 75 wt. % [102].

Sulfur is experimentally and thermodynamically confirmed to partition strongly into vapor phase in intermediate to silicic oxidized magma, especially when the temperature is below 900 °C [90,167,168]. The sulfur bubble/melt partition coefficient ($K_d = C_{s,bubble}/C_{s,melt}$) is 1 for basalt, $\sim$ 10 for andesite, $>$ 100 for rhyolite [31].

1.1.2 Measurements of volatiles

Volcanic volatile emission surveillance involves a combination of multidisciplinary activities, including direct sampling (Giggenbach bottles), groundbased or airborne ultraviolet spectroscopy (correlation spectrometer (COSPEC) and successors), ground-based infrared spectroscopy (Fourier transform spectroscopy and other infrared spectroscopic analyzers), electrochemical sensing, spaceborne methods, and petrological approaches to characterizing volatile abundances and emissions. The larger releases of volcanic volatiles to the atmosphere defy synoptic measurements from the ground. Here, I briefly introduce three methods that are widely used for explosive eruptions,

- Petrological method is the frequently utilized method that derives the volatile amount based on melt inclusion (MI) sampled from eruptions [38].

$$M_{\text{gas}} = 2M_{\text{magma}}F_{\text{melt}}(C_{\text{MI}} - C_{\text{MG}}) \tag{1.1}$$

  in which F_{melt} is the melt mass fraction. C_{MI} and C_{MG} are the volatile concentration from MI and matrix glass (MG), respectively. C_{MI} is regarded to be representative of the volatile concentration in the pre-eruptive magma. C_{MG} is considered as the the volatile concentration after eruption. By comparing these two quantities, this method provides an estimate for the degassing yield of an eruption. This method is widely applied because it provide a means to estimate the historic eruptions. It requires samples that contain pristine melt inclusions [49].

- Ice-core (IC) sulfur measurement is considered to be able to preserve the targeted deposited volatile species after travelling through the stratosphere [226]. The accuracy of this method is severely hindered by the ability to date ancient eruptions and the contamination related to simultaneous eruptions. The reliable signal for volcanic sulfur deposition can be dated back to $100 \sim 400$ ka [200, 226]. The overall Sulfur budget is also difficult to retrieve from ice core data and is highly model dependent.

- Romote sensing (RS) includes near-vent detection and satellite instrument (e.g., TOMS from 1978–2006) measurements. It directly measures the volatile content in volcanic

plumes. This method does not consider the volatile entrained by the fallout. Thus, it shows a minimum amount of volcanic volatile release. This method provides a fast measurement of the volatile content from volcanic eruption, typically in a few minutes for an explosive eruption. This method is only available over the last decades.

H_2O and CO_2, which are the principal components of volcanic gases, are challenging to measure accurately because of the high, and in the case of H_2O, rapidly varying, atmospheric background concentrations. Thus, more efforts in detecting volcanic gases are put on SO_2. The reasons for focusing measurements on SO_2 are that (1) the background levels are very low in the atmosphere (typical mixing ratios are ~ 1 ppbv), while mixing ratios in volcanic plumes can easily exceed 1 ppmv, and (2) several strong absorption bands for SO_2 are found in the ultraviolet and infrared regions of the spectrum [135].

1.1.3 Climate impact from volcanic eruptions

For explosive eruptions, the intensity of volcanic eruptions can be classified according to the volcanic explosivity index (VEI). This index, denoted as k, extends from 0 to 8, and is defined as,

$$k = \log_{10} M - 4, \tag{1.2}$$

where M is the volume (m^3) of erupted magma. Larger eruptions tend to occur less frequently, and the occurrence rate λ decays with VEI [155, 179],

$$\log_{10} \lambda = 2.83 - 0.79k \tag{1.3}$$

For example, the Mt. Pinatubo eruption in 1991 is characterized by a VEI of 6, a magnitude of eruption that is observed only every hundreds of years [210].

Volcanic eruptions greatly impact the regional and global climate as the sulfide aerosols formed from the SO_2 released deflect the sunlight and decrease the fraction of solar radiation that reaches the Earth's surface. A schematic graph of SO_2 transport is shown in Fig. 1.3(a) [65]. After being injected into the stratosphere by large explosive eruptions, SO_2 is transformed into sulfide aerosols and with a residence time that extends for years. According to observation of Total Ozone Mapping Spectrometer (TOMS) from 1978 to 2001,

a yearly average of 1.3 Mt SO_2 was detected from eruptions with VEI from 3 to 7 [22, 155]. As presented in Fig. 1.3(b), a statistical study of 122 subduction zone volcanoes and 16 non-subduction zone volcanoes concluded that larger eruptions shall load more SO_2 into the atmosphere [128, 155], following the empirical correlation

$$\log_{10} M_{SO_2} = 0.75k - 0.21, \tag{1.4}$$

where mass of SO_2, M_{SO_2}, is in kilotons. Effusive eruptions can contribute comparably the same amount of SO_2 as explosive eruptions according to Refs. [18, 22].

Large explosive eruptions, especially super eruption, like Toba, can exert large anomalies on global climate. A well studied case on sulfur release is the eruption of Mt. Pinatubo in 1991. The stratospheric umbrella come out of Pinatubo was reported to reach 35 km above the sea level. About $17 \sim 20$ Tg of dispatched SO_2 spent almost 3 weeks and was transported globally in the atmosphere [19, 65, 158]. Observations demonstrated greatly increased optical depth, 5% growth of the global albedo, and the decreased net energy flux only recovered background levels in March 1993 [124, 135, 159, 184, 214]. Toba (71 ka) was thought to be able to emit hundreds times more sulfur than Pinatubo (1991), and it could have played an important role on ancient climate [28].

1.2 Dissertation objectives and structure

The main objectives of this dissertation are advancing the understanding of volatile degassing process [188, 189]. In particular, I want to answer two questions. Can one use volatiles (sulfur in particular) to better understand the dynamics of volcanic eruptions? And, can one use the kinetics of degassing to better constrain magma ascent conditions during volcanic eruptions? In addition, I have also worked on understanding how bubbles deform under shear flow, and how saturated porous media respond to transient stress deformation [75, 76]. Specific objectives of this dissertation, along with the dissertation structure are:

- In Chap. 2, a new numerical model is established to quantify the amount of sulfur being degassed from silicic arc magmas. The release of large amounts of sulfur to the

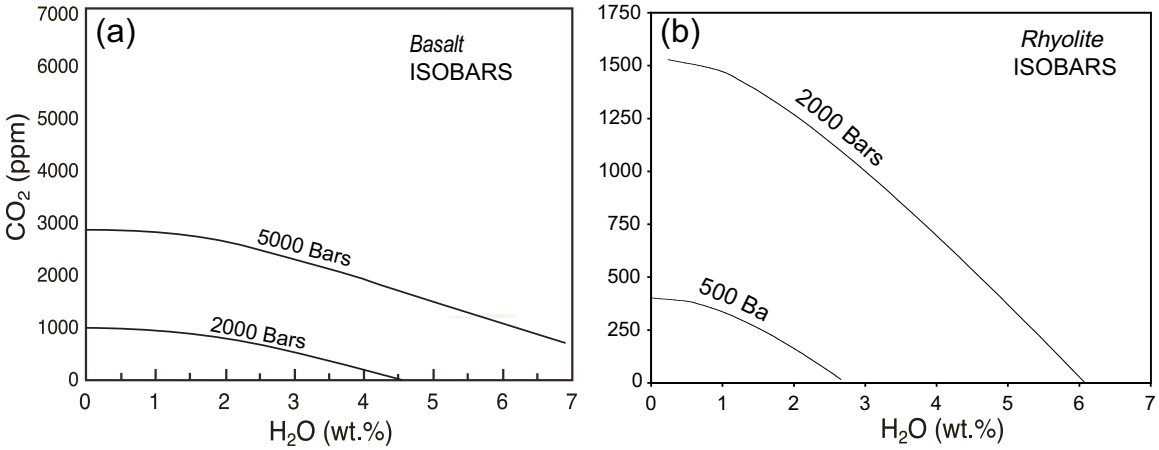

Figure 1.2: Solubility of H_2O and CO_2 in (a) basalt and (b) rhyolite (calculated with VolatileCalc [129]).

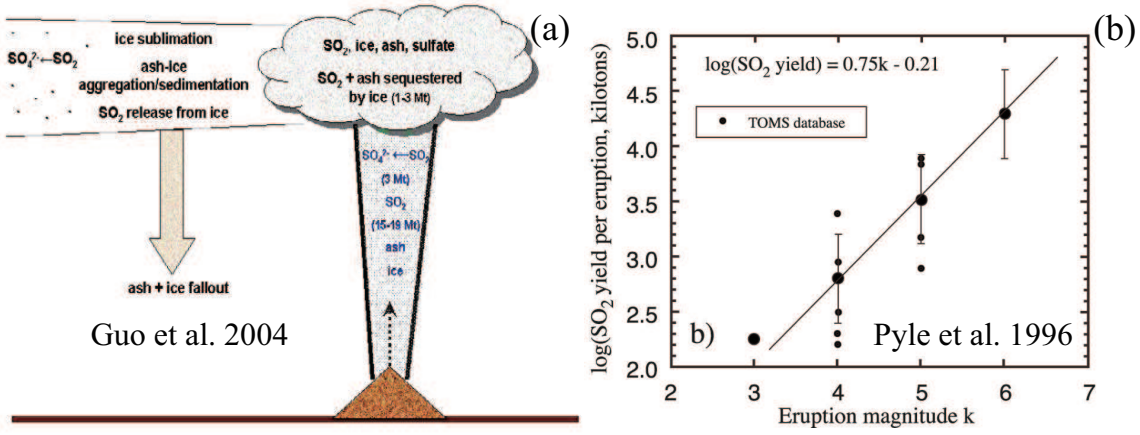

Figure 1.3: (a)Schematic of sulfur transportation of Pinatubo (Figure 1 in Ref. [65]). (b) Average SO_2 release vs. the eruption magnitude (Figure 3 in Ref. [155]).

stratosphere during explosive eruptions affects the radiative balance in the atmosphere and consequentially impacts climate for up to several years after the event. Providing quantitative estimates for the processes that control the mass balance of sulfur between melt, crystals and vapor bubbles is needed to better understand the potential sulfur yield of individual eruption events and the conditions that favor large sulfur outputs to the atmosphere. The processes that control sulfur partitioning in magmas are (1) exsolution of volatiles (dominantly H_2O) during decompression (first boiling) and during isobaric crystallization (second boiling), (2) the crystallization and breakdown of sulfide or sulfate phases in the magma and (3) the transport of sulfur-rich vapor transport (gas influx) from deeper unerupted regions of the magma reservoir. Vapor exsolution and the formation/breakdown of sulfur-rich phases can all be considered as closed system process where mass balance arguments are generally easier to constrain, whereas the contribution of sulfur by vapor transport (open system process) is more difficult to quantify. The ubiquitous "Excess Sulfur", which refers to the much higher sulfur mass released during eruptions than what can be accounted for by the melt inclusion data (petrologic estimate), reflects the challenges in closing the sulfur mass balance between crystals, melt and vapor before and during a volcanic eruption. In this chapter, I quantify the relative importance of closed and open system processes for silicic arc volcanoes using kinetic models of sulfur partitioning during exsolution. The calculations show that crystallization-induced exsolution (second boiling) can generate a significant fraction of the "Excess Sulfur" observed in crystal-rich arc magmas. This result does not preclude vapor migration to play an important role in the sulfur mass balance, but rather points out that second boiling (in-situ exsolution) can provide the necessary yield to drive the excess sulfur to the levels observed for these eruptions. In contrast, recharges of magma releasing sulfur-rich bubbles are necessary and most likely the primary contributor to the sulfur mass balance in silicic crystal-poor units. Finally, the model is applied to the Cerro Galan super-eruption in Argentina (2.08 Ma), and the results show the importance of second boiling in releasing a large amount of sulfur to the atmosphere during the eruption of large crystal-rich ignimbrites. This

chapter represents the work published in Ref. [189].

- In Chap. 3, I performed numerical simulations spannig a wide range of conditions (eruption durations, magma decompression paths, and pre-eruptive volatile compositions), to answer whether the volatile diffusion profiles around bubbles can be used to go better constrain magma decompression rates. Magma ascent rate is one of the key parameters that controls volcanic eruption style, tephra dispersion, and volcanic atmospheric impact. Many methods have been employed to investigate the magma ascent rate in volcanic eruptions and most rely on equilibrium thermodynamics. The study focuses on the effects of the total magma ascent time, the non-linearity of decompression paths, and the influence of different initial CO_2/H_2O content on the post-eruptive H_2O and CO_2 concentration profiles around bubbles within the melt. Results show that, under most circumstances, volatile-diffusion profiles do not constrain a unique solution for the decompression rate of magmas during an eruption, but, instead, provide a family of decompression paths with a well-defined trade off between ascent time and non-linearity. An important consequence of my analysis is that the common assumption of a constant decompression rate (averaged value) tends to overestimate the actual magma ascent time. This chapter represents the work published in Ref. [188].

- In Chap. 4, the behavior of exsolved bubbles of gas governs the style and intensity of volcanic eruptions. Although, several studies have focused on bubble growth from a silicate melt over the last decades, the models that have been proposed are based on a suite of assumptions that limits their applicability to low vesicularity magmas. These assumptions are: (1) bubbles are monodispersed and distributed as a periodic array, (2) there are no confining boundaries that prevent/limit growth, (3) bubbles remain spherical at all times and (4) bubbles do not interact hydrodynamically (no diffusion coarsening, no coalescence). At high vesicularity, such as those inferred from pumice samples, bubble-bubble interactions and bubble deformation by shear often become significant and these idealized models offer limited insight into the coupling between

the melt and bubbles as magma approaches a possible fragmentation level.

In this study, a new bubble dynamics model that alleviates most of these limiting assumptions is proposed. The novelty of my model is that it allows the study of evolution of a suspension of bubbles over a wide range of vesicularity and accounts for hydrodynamical interactions (deformation, coalescence) between bubbles while they grow, deform under shear flow conditions and exchange mass by diffusion coarsening (Ostwald ripening). The model is based on a lattice Boltzmann method for free surface flows. As such, it assumes an infinite viscosity contrast between the exsolved volatiles and the melt. My model allows coalescence when two bubbles approach each other because of growth or deformation. The parameter (disjoining pressure) that controls the coalescence efficiency, i.e., drainage time for the fluid film between the bubbles, can be set arbitrarily in my calculations. I decided to calibrate this parameter by matching the measured time for the drainage of the melt film across a range of Bond numbers (ratio of buoyancy to surface tension stresses) with laboratory experiments of a bubble rising to a free surface. After a description of the model and validations for bubble growth, Ostwald ripening and bubble deformation in simple shear conditions, I discuss how bubble orientation and deformation in a suspension is influenced by the presence of other bubbles over a range of Capillary numbers (ratio of shear to surface tension stresses). By designing specific laboratory experiments, the proposed model can be calibrated to reproduce accurately the physics of suspensions during the ascent of magma to the surface during an eruption. I plan on performing new experiments to calibrate the role of shear stresses on coalescence. This chapter represents the work published in Ref. [76].

- In Chap. 5, the lattice Boltzmann method is used to study the dynamical response of saturated porous media to transient stresses. I use pore-scale flow simulations with four different porous media topologies to study the effect of pore geometry and pore-size distribution on the dynamic response to transient pore-pressure forcing. I find a good agreement with published theoretical work for all but one medium that

exhibits the broadest pore-size distribution and therefore the largest degree of pore-scale heterogeneity. The results suggest the presence of a resonance peak at high frequency where the discharge, and therefore the effective permeability, is significantly amplified compared to their values around the resonant frequency. Two possible explanations have been suggested. This chapter represents the work published in Ref. [75].

- Chap. 6 summarizes the significant findings and overall contribution of this dissertation. Additional work and future research directions that build upon this dissertation are discussed.

CHAPTER II

SULFUR DEGASSING IN VOLCANIC ARC MAGMAS

Volcanic eruptions release more SO_2 than what is assumed to be stored in the magma that erupts, a phenomenon coined as the excess sulfur paradox [5, 206]. The assumed quantity of sulfur stored in a magma body prior to the eruption is computed from the composition of melt inclusions trapped within crystal phases before the onset of the eruption. The first report of this mismatch between observed S release and melt inclusion data sets came from the eruption of El Chichon volcano (1983), where the total ozone mapping spectrometer (TOMS) data was used in comparison with data derived from melt inclusions.

Shinohara [177] summarized in total 31 eruptions and quantified this excess S release (defined as the ratio of sulfur measured from remote sensing or ice cores to that constrained from melt inclusions) in eruptions spanning a range of tectonic settings (spreading ridge, hot spot, and subduction zone), magma composition (basalt, andesite, dacite and rhyolite) and explosion styles (effusive to explosive). Excess sulfur values vary from 1 to about 100, with subduction zone explosive volcanism generally populating the high end of the spectrum. Thus, the accuracy of the petrological method has been questioned as it tends to underestimate the S yield from eruptions. An explanation for the discrepancy relates to the presence of a pre-eruptive volatile phase where a portion of the S is already stored by the time the melt inclusion forms [206]. As of yet, this conceptual idea has never been tested quantitatively with kinetic models that include the main processes related to degassing and bubble growth, as well as recent experimental constraints on S kinetics and partitioning in silicic magmas. In this chapter, two numerical models for (1) syn-eruptive degassing (first boiling) and (2) isobaric crystallization degassing (second boiling) are introduced to quantity the excess sulfur phenomenon for silicic subduction zone volcanism. Other possible sources for excess sulfur, including (3) the crystallization and breakdown of sulfide or sulfate phases in the magma and (4) the transport of sulfur-rich vapor transport (gas influx) from

deeper unerupted regions of the magma reservoir are discussed as well for their role in sulfur degassing in closed system and open system. The content of this chapter has been published in Ref. [189]. The numerical scheme designed in this chapter is shown in Appendix A and Appendix B.

2.1 Introduction

Sulfur species are frequently monitored at active volcanoes because they are detected more accurately in the atmosphere than H_2O and CO_2 [135]. They can strongly impact the climate for years through the formation of aerosols [120,172]. The amount of sulfur released to the troposphere and stratosphere can be significant during explosive eruptions at arc volcanoes [168, 177]. There are three independent ways to estimate the mass of volatiles released during volcanic eruptions: (1) remote sensing (RS) methods based on spectroscopy, available for the past 3 decades [109], (2) sulfur record in ice-cores (IC) which are limited to the past few tens of thousands of years [226], and (3) a comparison between melt inclusion (MI) and groundmass glass (GG) compositions (petrological estimate) [2, 57, 58]. All three methods have limitations; RS is probably the most reliable but is available only for the last 3 decades; IC data suffer from a lack of spatial and temporal resolution; melt inclusions may leak or trap a partially degassed melt. When comparing these different estimates, a consistent signal appears where melt inclusion data generally underestimate the amount of sulfur outgassed by 1 to 2 orders of magnitude especially in silicic arc-volcanoes, a deficit referred to as "excess sulfur" [5, 30, 34, 38, 41, 57, 58, 67, 109, 113, 122, 140, 166, 170, 171, 173, 177, 178, 187, 195, 196, 206, 209].

One way to express excess sulfur is to compare the difference between the mass of total released SO_2 per km^3 of magma and the mass of SO_2 per km^3 of magma that could be supplied by degassing during the eruption [206]. Another way to express excess sulfur is to calculate the ratio of the total amount of sulfur released to the atmosphere and the amount of released sulfur measured by the traditional petrologic method [177], which I will refer here to as the excess sulfur ratio. Both approaches have advantages under different applications and should be thought as complementing each other. The first definition of excess sulfur

is advantageous in that it provides an absolute estimate of the mass of the missing sulfur reservoir, but it relies on the ability to constrain the initial sulfur concentration in the melt pre-decompression. The second approach, proposed and followed here provides a relative measure of the missing sulfur reservoir. And this method could give a possible large uncertainty when the sulfur concentration concentrations in the groundmass could be below analytical detection limits in eruptions of relatively low-temperature. I show in Sec. 2.2.1 that the excess ratio is independent of the initial sulfur content of the magma, which is often one of the most poorly constrained parameters that these excess metric rely on.

The sulfur released to the atmosphere during an eruption is delivered by an exsolved volatile phase in the magma. The delivery of sulfur to gas bubbles can occur in four possible ways (Fig. 2.1) [18, 167, 177, 206, 210]. The first three are closed-system processes and can be constrained from (non-equilibrium) thermodynamics: first boiling (decompression-driven exsolution, contributing to $M_{s,b}^{dec}$), second boiling (crystallization-induced exsolution under quasi-isobaric conditions, contributing to $M_{s,b}^{MR}$) and the breakdown of S-bearing minerals (sulfide or sulfates depending on the redox state of the magma, contributing to both $M_{s,b}^{MR}$ and $M_{s,b}^{dec}$). The excess sulfur ratio (E) generated in a closed-system magma body is defined as,

$$E = \frac{M_{s,b}^{MR} + M_{s,b}^{dec}}{M_{s,MI} - M_{s,GG}} \tag{2.1}$$

where $M_{s,b}^{MR}$ is the mass of sulfur in bubbles in the magma reservoir and $M_{s,b}^{dec}$ is the contribution from syn-eruptive decompression [177,206]. The denominator, defined as the amount of sulfur measured from traditional petrologic estimates, is calculated as the difference in sulfur concentration between MI and GG. In order to interpret the excess sulfur ratio E in terms of dynamical processes, I need to obtain a better understanding of each term in Eq. 2.1. However, it is worth noting that Eq. 2.1 is only valid for closed systems, while magma chambers are known to be open systems. I therefore correct this expression to account for the transport of S-rich volatiles from new magma recharge or degassing from an underlying crystal mush which can also contribute to the sulfur mass balance via the term

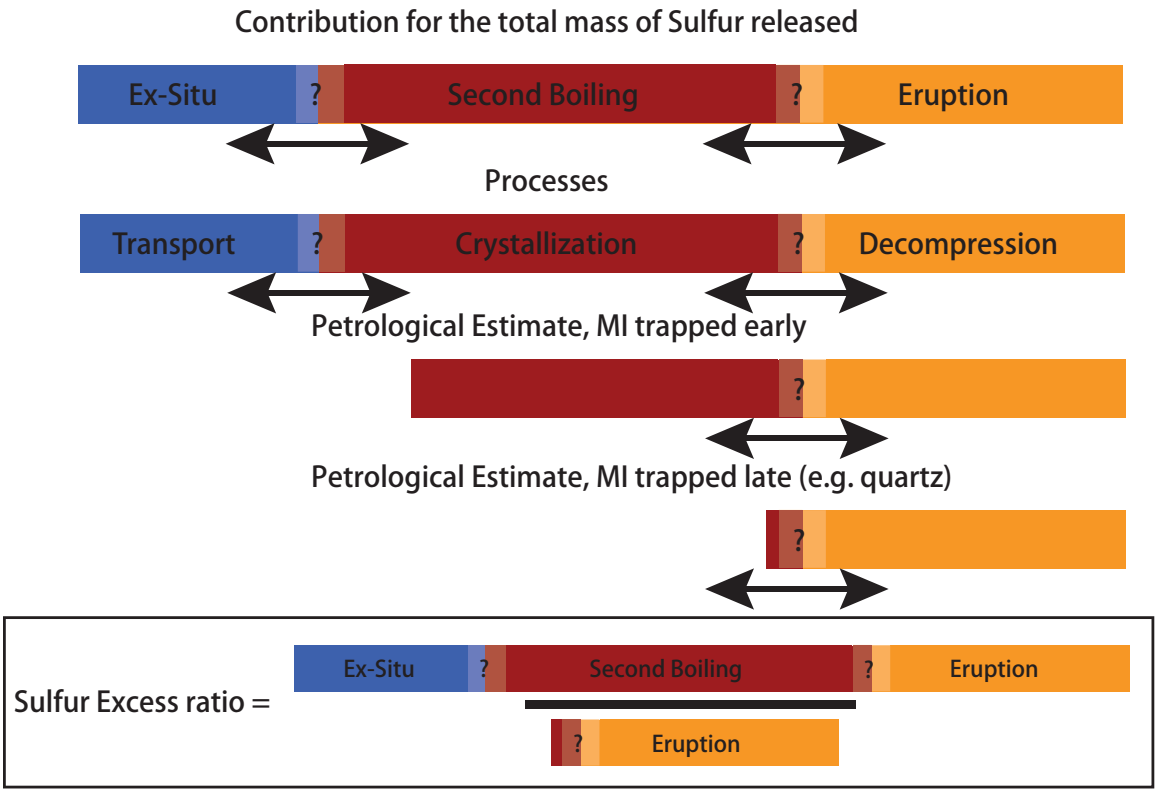

Figure 2.1: The different contributions to the sulfur mass balance in volcanic gases and their relation to the excess sulfur. Lengths of the bars represent the amount of sulfur emitted from volcanic eruptions (not drawn to exact scale, for representational purpose only). The top four bars have its own title above them. The first bar illustrates schematically the three different contributions to the sulfur uptake by vapor bubbles in magmas and list the three contributions to the total amount of sulfur that is emitted during a single eruption. The processes associated with each contribution are listed in the second bar just below. The third and fourth bars represent the relative amount of sulfur uptake when MI used in traditional petrological estimate is early or late. The bottom panel is a cartoon illustration of Eq. 2.1 when there is large excess sulfur.

M_s^{Open}

$$E = \frac{M_{s,b}^{MR} + M_{s,b}^{dec} + M_s^{Open}}{M_{s,MI} - M_{s,GG}}. \tag{2.2}$$

Quantifying the relative importance of the open-system contribution is more challenging because it requires constraints on the size and composition of the un-erupted magma source as well as mechanical models for the transport and accumulation of these volatiles in the magma column. By first quantifying the closed-system sources, I propose to evaluate what is the minimum portion of the entire sulfur mass balance carried by open-system sources, e.g., transport from un-erupted magma. Within this context, I propose two novel kinetic models of bubble growth and uptake of sulfur (Fig. 2.2) to assess the relative importance of the various S-degassing processes in building up the excess sulfur. Unless stated otherwise, the conditions of the calculations in this work are set up for typical silicic arc magmas.

2.2 Methods

2.2.1 Insight into the excess sulfur ratio from equilibrium mass balance

In a closed system, the mass of sulfur is conserved and partitioned in up to three phases,

$$C_m^0 = C_m^{MI}(1 - X_b^{MI} - X_c^{MI}) + C_b^{MI} X_b^{MI} + C_c^{MI} X_c^{MI}, \tag{2.3}$$

where the subscripts m, b, and c refer to melt, bubble, and crystals, respectively, while the superscripts MI and 0 refer to the concentration of sulfur in the respective phase at the time melt inclusions are trapped and at the liquidus, respectively; X is the mass fraction of the phase considered. From Eq. 2.3, I retrieve the well-known three phases version of the law for equilibrium crystallization,

$$\frac{C_m^{MI}}{C_m^0} = \frac{1}{D_c X_c^{MI} + D_b X_b^{MI} + (1 - X_c^{MI} - X_b^{MI})}, \tag{2.4}$$

$$C_b^{MI} = \frac{K_b C_m^0}{D_c X_c^{MI} + D_b X_b^{MI} + (1 - X_c^{MI} - X_b^{MI})}, \tag{2.5}$$

where $K_s = C_b^{MI}/C_m^{MI}$ is the sulfur vapor/melt partition coefficient (assumed constant in this simple argument, but varied in the numerical calculations below). I now consider two cases. In the first case, there is either no exsolution or alternatively $K_s = 0$ and the vapor phase does not fractionate sulfur and the crystal/melt partition coefficient for sulfur $K_s^* = 0$

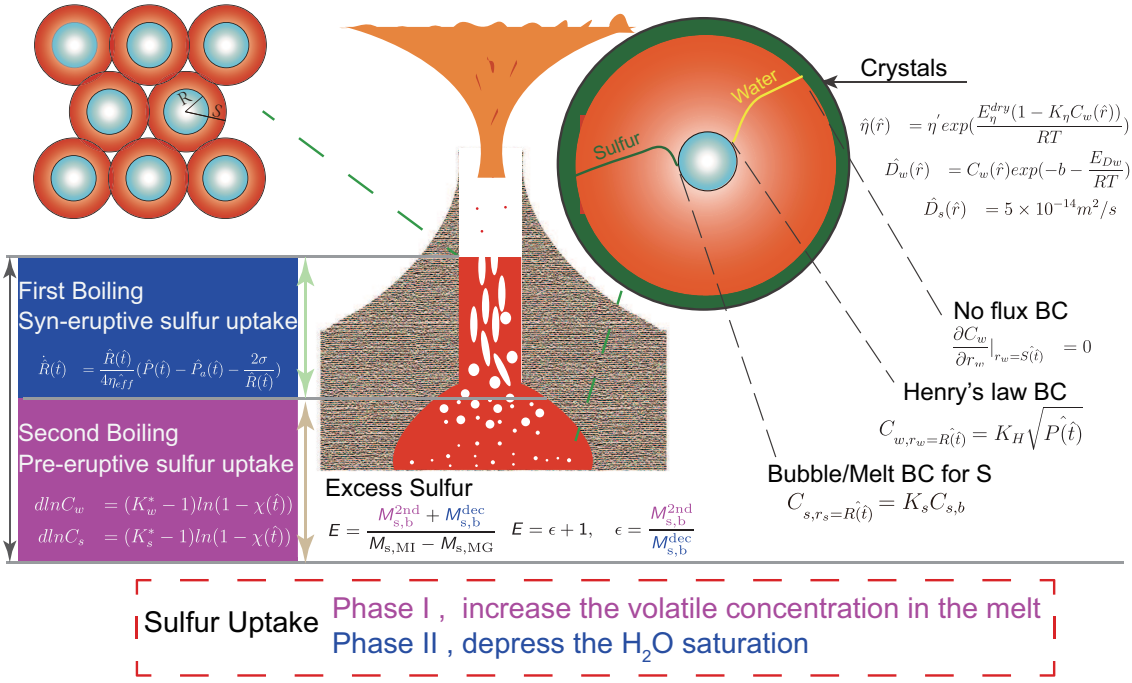

Figure 2.2: Schematic diagram for my numerical models. The upper left diagram shows the bubble growth during ascent in the conduit (decompression) and the upper right shows the bubble growth in the shallow magma chamber (second boiling). Each bubble lies at the center of a spherical melt shell. The effect of crystallization is accounted for by reducing the diffusion distance (I remove an outer layer of the melt shell with a volume equivalent to the amount of crystals that formed. I assume that both H_2O and sulfur species are incompatible with the crystal phases. Different boundary conditions (BC) between simulation cells and BCs for H_2O and sulfur at the bubble/melt interface are illustrated in the diagram.

(see justifications later in Sec. 2.2.3) which, considering for example 30 wt.% crystallization yields a relative increase in sulfur concentration in the melt of

$$\frac{C_m^{MI}}{C_m^0} \approx 1.42. \tag{2.6}$$

If, on the other end, vapor exsolution takes places concurrently with crystallization (2^{nd} boiling) and assuming that the magma is water-saturated near the liquidus, about 2 wt.% water would exsolve over the crystallization of 30 wt.% of the magma assuming an equilibrium process. In that context, assuming a vapor-melt partition coefficient for sulfur of $K_s = 100$ and using Eq. 2.5, I get

$$\frac{C_m^{MI}}{C_m^0} \approx \frac{1}{3}. \tag{2.7}$$

In other words, the presence of a vapor phase, in which sulfur is strongly compatible, decreases significantly the mass of sulfur in the melt (here about 4 times). This shows the importance of considering the presence of a vapor phase during crystallization for the partitioning of sulfur. Using these estimates to infer directly an excess sulfur ratio (as I define it in Eq. 2.1) can be done under a set of simplifying assumptions.

The excess sulfur ratio can be reframed as

$$E = 1 + \frac{C_b^{MI} X_b^{MI}}{C_m^{MI}(1 - X_b^{MI} - X_c^{MI}) - C_g(1 - X_b^p - X_c^p)}, \tag{2.8}$$

where C_g is the average concentration of sulfur in the GG and the superscript p refers to various phases mass fractions in the pumice or scoria. Using my kinetic calculations I can replace the denominator by

$$C_m^{MI}(1 - X_b^{MI} - X_c^{MI}) - C_g(1 - X_b^p - X_c^p) = f \times C_m^{MI}(1 - X_b^{MI} - X_c^{MI}), \tag{2.9}$$

where f is an efficiency factor that introduces a kinetic limitation to syn-eruptive sulfur degassing, this factor will be determined by numerical calculations of decompression degassing in a later section.

The excess sulfur ratio then becomes

$$E = 1 + \frac{K_s X_b^{MI}}{f(1 - X_b^{MI} - X_c^{MI})} \tag{2.10}$$

where E is independent of the initial sulfur concentration in the primordial melt, which is an important advantage of the definition of E compared to an absolute excess mass of sulfur, as the primordial (pre-degassing) sulfur concentration in the melt is hard to constrain. Basically, Eq. 2.10 shows that the factors that lead to large possible excess sulfur ratio are (1) a high mass fraction of the exsolved vapor X_b^{MI}, (2) a lower the mass fraction of residual melt $1 - X_b^{MI} - X_c^{MI}$ at the time of the entrapment of the melt inclusions, and (3) a low efficiency of syn-eruptive sulfur degassing f due to kinetic limitations.

As an example, assuming that the magma contains initially about 6 wt.% of volatiles, I find that 2 wt.% vapor is exsolved ($X_b^{MI} = 0.02$) after the crystallization of 30 wt.% crystals ($X_c^{MI} = 0.3$). Using an average $K_s = 100$ and $f = 0.1$, I get $E \sim 30$ (see Fig. 2.3), which shows that second boiling and kinetically-limited degassing during syn-eruptive decompression can lead to large excess ratio values and that the excess ratio under these assumptions does not depend on the initial composition of the melt explicitly.

These equilibrium mass balance calculations are not meant to quantify the contribution of various sulfur degassing processes, but they are helpful to highlight some of the features that control the excess sulfur. This model however suffers from the lack of kinetics, f is unknown and assumes that the sulfur partition coefficient K_s between bubble and melt is constant whereas K_s is a composition dependent value and will evolve as the magma crystallizes. Thus, more sophisticated calculations are required. For this purpose, I propose two kinetic multiphase vapor bubble growth models. The first model, focused on syn-eruptive (decompression) degassing (Sec. 2.2.2.1) is designed mainly to characterize the kinetic degassing limitation factor f. The second model involves sulfur kinetics within a three phase magmas (crystals, melt, and vapor bubbles) during near isobaric conditions. In this case, degassing is there promoted by the crystallization of mostly anhydrous phases (Sec. 2.2.2.2). These models offer one the benefit of studying kinetics as well as using composition dependent partition coefficients in Fig. 2.2.

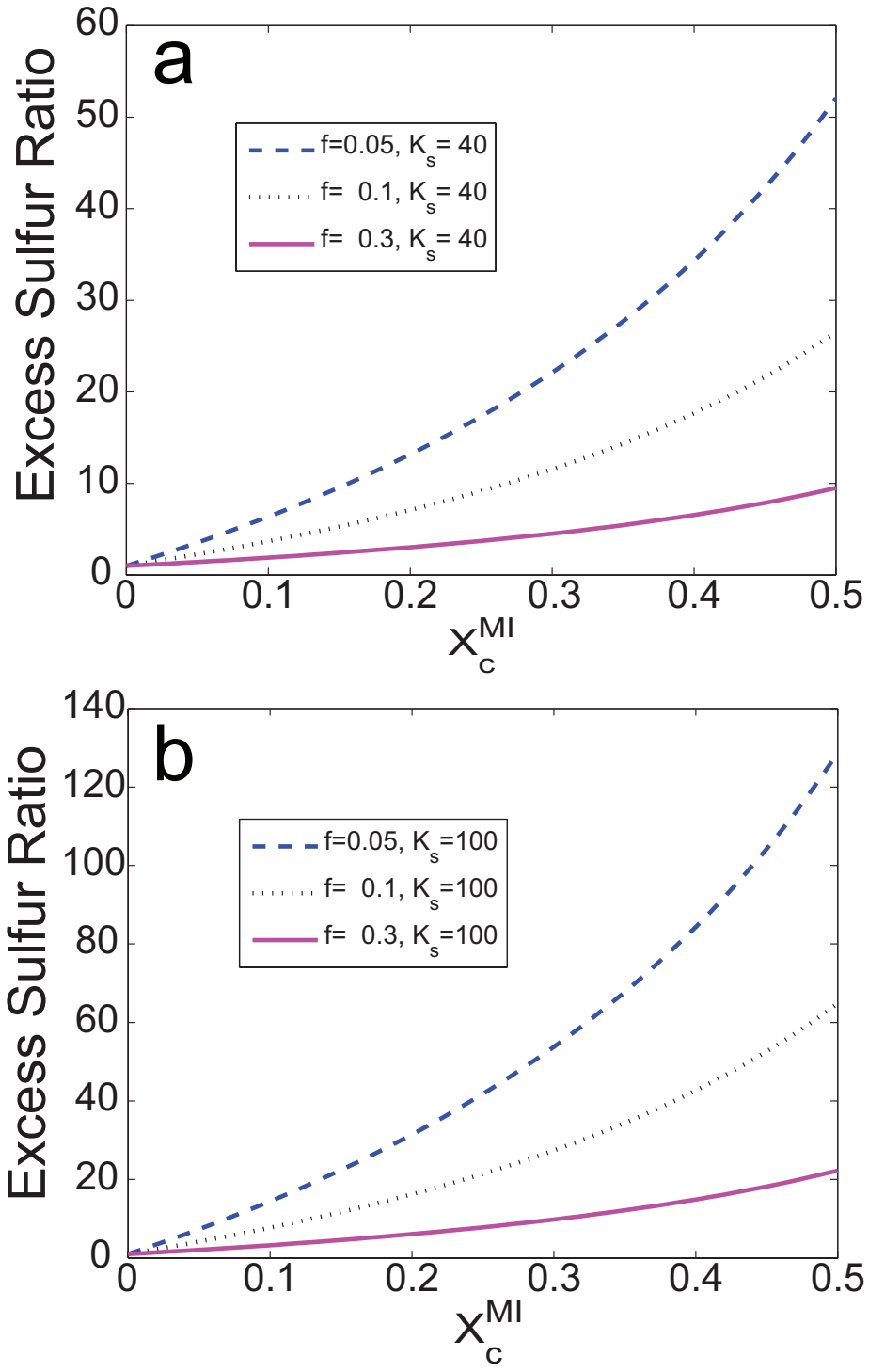

Figure 2.3: The effect of the syn-eruptive degassing efficiency f and the vapor/melt partition coefficient on the excess sulfur ratio as function of crystal content X_c^{MI} at the point where the melt inclusion is trapped. These trends are computed from the equilibrium model in Eq. 2.10.

2.2.2 Numerical models for sulfur kinetics in magmas

The numerical models are extensions to previous work on bubble dynamics and H_2O kinetics [44, 97], where sulfur is added as an additional diffusing species. Sulfur speciation is not explicitly taken into account in my model. As shown in Fig. 2.2, the bubbles are spherical with a uniform radius $\hat{R}(\hat{t})$. Each bubble is surrounded by a melt shell of radius $\hat{S}(\hat{t})$. In the following, hatless variables are dimensionless unless specified otherwise. Bubbles grow by diffusion and decompression. Nucleation is not considered here, because these kinetic bubble growth models cannot account for it. At the start of each simulation, bubble seeds (4 vol.% of the whole system) are set in a periodic array and no secondary nucleation event is considered. Although secondary nucleation can occur during syn-eruptive decompression, it is unlikely to play a major role during second boiling where the growth is slow enough to approach equilibrium conditions for water. From my numerical simulations, the error in sulfur mass balance related to the assumption of an initial 4 vol.% vapor is at most < 2 wt.% of the overall sulfur mass budget and it is therefore insignificant compared to the error bars associated with measured excess sulfur ratio. The mass of volatiles and momentum in and around bubbles are conserved. The pressure in bubbles $\hat{P}(\hat{t})$ is calculated from the bubble mass and an ideal gas law. The ideal gas law is applicable in the conduit and the shallow magma chamber when the pressure is 50–250 MPa and temperature is up to 900 °C [29]. I solve the transport of dissolved H_2O from the melt to the bubble's interface where the melt-bubble boundary condition for H_2O concentration follows Henry's law and the boundaries between neighbor melt shells are set to no-flux conditions. H_2O diffusivity depends on temperature (here fixed) and H_2O concentration [154].

My goal is to solve for a simplified version of sulfur kinetics in silicic melts and better constrain the partitioning of sulfur between melt and bubbles during bubble growth by first boiling and second boiling. I do not consider the presence of anhydrite, or sulfide phases in the magma and their effects on sulfur partitioning at this stage due to that anhydrite is rare in volcanic units because anhydrite saturation occurs at high sulfur concentrations in the silicate melt (although has been seen by [108], [27], and [20]). The sulfur concentration at anhydrite saturation (SCAS) in silicate melts decreases with increasing degree of melt

polymerization (i.e., from mafic to felsic composition), and decreasing temperature and pressure. At the average depth of upper crustal reservoirs (P = 200 MPa), for hydrous magmas, the typical SCAS values would be $\sim$ 5000 to 10000 ppm for basaltic melts, $\sim$ 2000 ppm for andesitic melts, $\sim$ 1000 ppm for dacitic melts, and $\sim$ few hundred ppm for rhyolitic melts [10, 23, 24, 87, 220, 221]. Magmatic sulfides also occur in some arc magmas [7, 31, 113, 202, 211]; however, their abundance is generally low and/or their occurrence is largely limited to inclusions within other crystal phases, probably due to the fact that most of the sulfur is dissolved in the silicate melt as oxidized sulfate species. Further discussion on the effect of sulfur-bearing minerals is shown in Sec. 2.2.3.

Sulfur changes its oxidation state over a narrow range of fO_2 (i.e., NNO and NNO+1) from S^{2-} dominated to S^{6+} dominated and most arc magmas are characterized by fO_2 between NNO and NNO+2 log units [88, 91]. If fO_2 is low enough to allow sulfur to be dominantly present as sulfide species in the melt, saturation in pyrrhotite would occur in various hydrous arc magmas at: $\geq$ 600 ppm for basaltic melts, $\sim$ 350 ppm for andesitic melts, $\sim$ 250 ppm for dacitic melts, $\sim$ 150 ppm for rhyolitic melts [87, 169, 221]. The influence of these S-bearing minerals will be re-evaluated in Sec. 2.3.3.

As I do not explicitly account for these S-bearing phases in sulfur partitioning, I treat it as a trace element, and its diffusivity $\hat{D}_s$ (5×10^{-14} m^2/s) is set to be consistent with values measured in silicic magmas (dacite to rhyolite) [46]. The partition coefficient K_s between the bubble and the melt is kept constant, but I use different values to bracket the range of published data ($K_s = 40$ and $K_s = 600$) [90, 169, 221]. The equations that describe sulfur kinetics therefore reduce to,

$$\frac{\partial C_s}{\partial \hat{t}} + v_m \frac{\partial C_s}{\partial \hat{r_s}} = \frac{1}{\hat{r_s}^2} \frac{\partial}{\partial \hat{r_s}} \left(\hat{r_s}^2 \hat{D}_s \frac{\partial C_s}{\partial \hat{r_s}} \right) \tag{2.11}$$

$$C_{s,r_s=\hat{R}(\hat{t})} = K_s C_{s,b} \tag{2.12}$$

$$\frac{\partial C_s}{\partial r_s}|_{r_s=\hat{S}(\hat{t})} = 0, \tag{2.13}$$

where C_s and $C_{s,b}$ are the sulfur concentration within the melt and bubble, respectively; $C_{s,r_s=\hat{R}(\hat{t})}$ is the sulfur concentration within the melt at the bubble/melt interface; v_m is the velocity of the melt-bubble interface [44].

2.2.2.1 Syn-eruptive decompression model

The goal of the syn-eruptive degassing calculations is to estimate the efficiency factor f in Eq. 2.7. In these calculations, I seeded the magma with a similar amount of exsolved volatiles bubbles (4 vol.%). This value is consistent with other models of bubble growth during eruptions [44, 97, 154]. The initial nuclei can be either S-free or be equilibrated with the melt. Calculations show that the former S-free nuclei can lead to smaller f factor in Eq. 2.9 and larger excess sulfur ratio as compared to S-equilibrated nuclei. Reported results in this chapter are based on the latter case. I neglect nucleation events during the rise of magma in the conduit in these calculations, as do all other kinetic models for volatile exsolution.

I introduce $\tau_{\rm dec} = \hat{P}_i/\dot{\hat{P}}$ as the time scale for the decompression. $\dot{\hat{P}}$ is a constant decompression rate, while $\hat{P}_i$ is the initial magma chamber pressure. Three other time scales emerge from my model, the viscous time scale $\tau_{\rm vis} = 4\hat{\eta}_i/\hat{P}_i$, the diffusive time scale for H_2O $\tau_{\rm dif} = \hat{R}_i^2/\hat{D}_{wi}$ and for sulfur $\tau_{\rm dif} = \hat{R}_i^2/\hat{D}_{si}$. Three dimensionless numbers arise from these time scales. The first two characterize the diffusion efficiencies for H_2O and sulfur ($\Theta_{Dw} \gg \Theta_{Ds}$), and the last one represents the hydrodynamic response of bubble growth Θ_V to syn-eruptive eruptions [44, 97],

$$\Theta_{Dw} = \frac{\tau_{\rm dif,w}}{\tau_{\rm dec}} = \frac{\hat{R}_i^2\dot{\hat{P}}}{\hat{D}_{wi}\hat{P}_i} \qquad \Theta_{Ds} = \frac{\tau_{\rm dif,s}}{\tau_{\rm dec}} = \frac{\hat{R}_i^2\dot{\hat{P}}}{\hat{D}_{si}\hat{P}_i} \qquad \Theta_V = \frac{\tau_{\rm vis}}{\tau_{\rm dec}} = \frac{4\hat{\eta}_i\dot{\hat{P}}}{\hat{P}_i^2} \tag{2.14}$$

in which $\hat{\eta}_{\rm eff}$ is the effective viscosity which includes the dependence of melt viscosity on H_2O concentration [98, 154]. In most of my decompression simulations, the ranges for Θ_{Dw}, Θ_{Ds} and Θ_V are around $10^{-4} \rightarrow 10^{-1}$, $10^{-1} \rightarrow 10^{2}$ and $10^{-5} \rightarrow 10^{-2}$, respectively. The flowchart of this scheme is shown in Appendix A, and the related notation list is shown in Appendix C.

In order to constrain the role of syn-eruptive decompression on the efficiency of sulfur extraction from the melt, I define the apparent bubble-melt partition coefficient of sulfur as the magma reaches the vent (atmospheric pressure)

$$\langle K_d \rangle = C_{s,bubble}/\langle C_{s,melt} \rangle \tag{2.15}$$

where $C_{s,bubble}$ and $\langle C_{s,melt}\rangle$ are the sulfur concentration in the bubble and the average sulfur concentration in the melt, respectively. The variation of $\langle K_d\rangle$ as function of decompression rates, typical of silicic eruptions (Fig. 2.4, 10^4 Pa/s $\leq \dot{\hat{P}} \leq 10^7$ Pa/s) [197], highlights three regimes for sulfur and H_2O kinetics. At low decompression rates ($< 10^5$ Pa/s), the diffusion time scales for H_2O and sulfur are shorter than the decompression time scale, consequently, $\langle K_d\rangle$ approaches the actual partition coefficient. At intermediate decompression rates, sulfur uptake by bubbles is kinetically-limited, but H_2O can reach near equilibrium conditions because its diffusion coefficient is 3 orders of magnitude greater than sulfur. Lastly, at high decompression rates ($> 10^6$ Pa/s), H_2O and sulfur diffusion are both transport limited and the chemical composition of the bubble remains close to that before syn-eruptive decompression (here initial equilibrium state at $\hat{P}_i$). Generally, the syn-eruptive sulfur uptake by bubbles is kinetically-limited for explosive eruptions, and I find that under decompression rates consistent with explosive silicic eruptions (10^6 Pa/s $\leq \dot{\hat{P}} \leq 10^7$ Pa/s), only a less than about 10% of the total sulfur has time to degas to nearby bubbles, and consequently that for explosive eruption of silicic magmas the efficiency factor f is close to 0.1.

2.2.2.2 Second boiling model

During second boiling, the driving force for exsolution is the crystallization of anhydrous phases at relatively constant pressure. Crystallization drives the melt composition to be supersaturated in H_2O. In all simulations of crystallization-driven exsolution, the ambient pressure $\hat{P}_a$ is set to a constant value of 200 MPa. Because of the three coexisting phases (crystals, melt, and bubbles), two additional partition coefficients are needed to constrain the mass balance of H_2O and sulfur species between the melt and solid phases K_w^* and K_s^*. The partitioning equations act as a source ($K_w^* < 1$ and $K_s^* < 1$) or a sink term ($K_w^* > 1$ and $K_s^* > 1$) for the H_2O and sulfur in the melt in my main conservation equations (The flowchart of this scheme is shown in Appendix B and Appendix C).

$$d\ln C_w = (K_w^* - 1)\, d\ln\left(1 - \chi(\hat{t})\right) \tag{2.16}$$

$$d\ln C_s = (K_s^* - 1)\, d\ln\left(1 - \chi(\hat{t})\right). \tag{2.17}$$

As discussed previously, I assume that no S-bearing minerals are present in the magma,

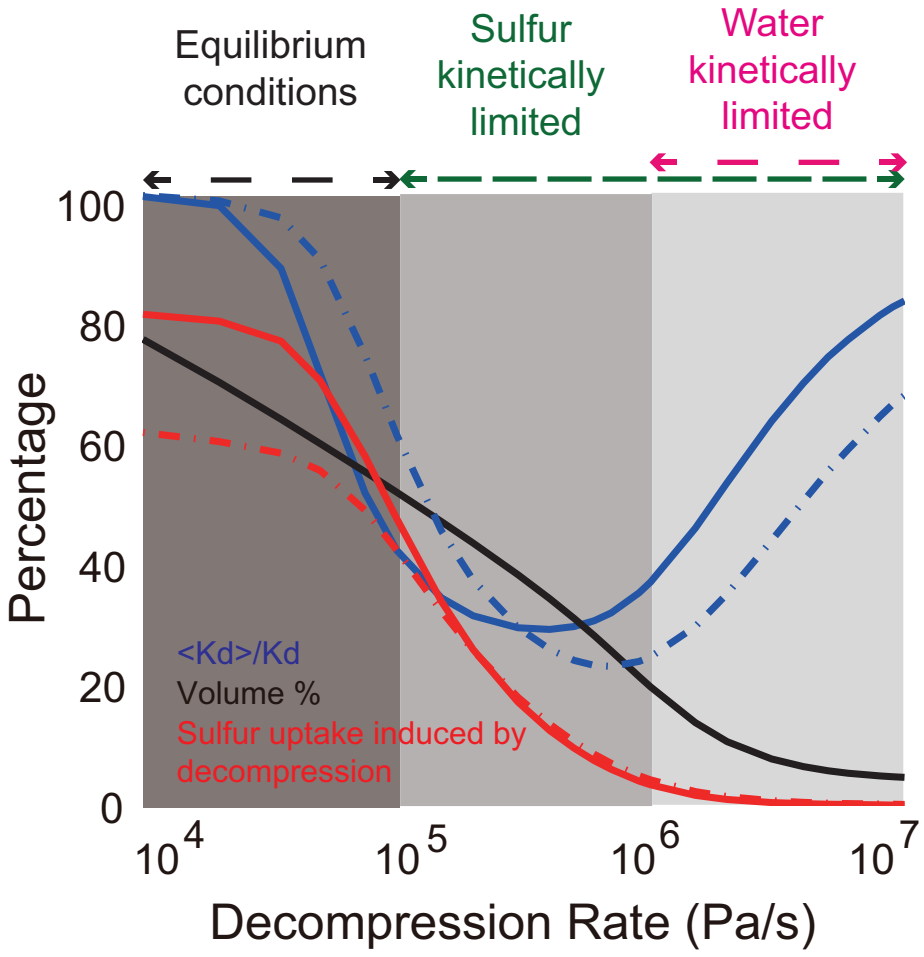

Figure 2.4: Degassing of sulfur during syn-eruptive silicic eruptions. $\langle K_d \rangle / K_d$ (blue), bubble volume fraction (black) and the weight percent of the sulfur degassed in melt (red) at the end of decompression as a function of the imposed constant decompression rates. For these calculations, I set the initial H_2O and sulfur concentrations are 6 wt.% and 1000 ppm, respectively. The bubbles and the melt are assumed to be in chemical equilibrium initially before decompression starts. The range of partition coefficient K_d (= 40 for dashed line; = 600 for solid line) does not impact significantly the efficiency of decompression on sulfur degassing.

and set K_w^* and K_s^* to 0 (see more details below). I assume that the crystallization rate $\dot{\chi} = d\chi/dt$ is constant, but varying it would not impact my results as long as the time scale for crystallization $\tau_{\rm x} = \Delta\chi/\dot{\chi}$ is much longer than the viscous and diffusion time scales ($\tau_{\rm vis}$ and $\tau_{\rm dif}$). $\Delta\chi$ is the crystallization interval over which second boiling occurs (starts when the first bubble nucleates). Again, three dimensionless parameters emerge from the ratios of the crystallization, diffusion, and hydrodynamic growth time scales,

$$\Theta_{Dw}^* = \frac{\tau_{\rm dif,w}}{\tau_{\rm x}} = \frac{\hat{R}_i^2\dot{\chi}}{\hat{D}_w\Delta\chi} \qquad \Theta_{Ds}^* = \frac{\tau_{\rm dif,s}}{\tau_{\rm x}} = \frac{\hat{R}_i^2\dot{\chi}}{\hat{D}_s\Delta\chi} \qquad \Theta_V^* = \frac{\tau_{\rm vis}}{\tau_{\rm x}} = \frac{4\hat{\eta}_i\dot{\chi}}{\hat{P}_i\Delta\chi}. \tag{2.18}$$

In volcanic systems, Θ_{Dw}^* and Θ_V^* are on the order of $10^{-10} \rightarrow 10^{-12}$ when $\tau_{\rm x} \approx 1000$ yrs. If the crystallization rate is slow, then to a good approximation H_2O diffusion, which is much faster than sulfur diffusion, can be considered at equilibrium. This allows one to simplify the kinetic equations for H_2O diffusion, and it makes the calculations much more efficient. However, because Θ_{Ds}^* (10^{-7}) is 3 orders larger than Θ_{Dw}^*, I still consider sulfur kinetics in all simulations. I note however that all three dimensionless terms Θ imply that $\tau_{\rm x} \gg$ other time scales which justifies my simplified assumption for a linear crystallization rate. The two conservation equations for H_2O and sulfur in the melt are modified to include the source term (Eqs. 2.16 and 2.17) associated with the fractionation of H_2O and sulfur between the melt and newly formed crystal phases. I assume that the vapor/melt partition coefficient K_s for sulfur becomes higher as the crystallinity increases, i.e., K_s increases as the melt evolves from a dacitic to a rhyolitic composition [90, 169, 221]. A linear trend of K_s is applied to parametrize the effect of the melt composition on the partition coefficient for sulfur,

$$K_s(\hat{t}) = 70 + 1060\Delta\chi(\hat{t}) \tag{2.19}$$

thus $K_{s1} = 70$ at the beginning of second boiling (dacitic melt), and $K_{s1} = 600$ when $\Delta\chi = 50$ vol.% as the melt becomes rhyolitic. The range of partition coefficients for sulfur is motivated by experimental data [90, 169, 221].

In the second boiling simulations, I also start the calculations with 4 vol.% water vapor and assume that the vapor bubbles and the melt are initially in chemical equilibrium with respect to sulfur. This would present an upper bound for the efficiency of sulfur to

partition into bubbles and it is important to calculate how this assumption impacts my estimates for the excess sulfur ratio. Comparing kinetic calculations assuming (1) equilibrium sulfur content in the initial bubble fraction and (2) no sulfur in the bubble prior to subsequent bubble growth, I obtain an overestimate the mass of sulfur contained in bubbles post second-boiling of at most 1.5 wt.% after 10 wt.% crystallization and only 1.2 wt.% after 45 wt.% crystallization. Moreover, calculations that start with a smaller initial vapor volume fraction, e.g., 1 vol.%, do not affect my results significantly and the error associated with bypassing the nucleation process in my simulation remains of the order of a percent of the overall mass balance for sulfur. For second boiling, where crystallization is the driving force behind exsolution, it is safe to assume that bubble growth dominates the exsolution process over new nucleation events.

2.2.3 The influence of sulfur-bearing minerals on sulfur partitioning

In the isobaric degassing model (Sec. 2.2.1 and Eq. 2.17 in Sec. 2.2.2.2), I assumed the bulk partition coefficient of sulfur K_s^* between solid phases and melt to be zero. This simplification is motivated by the assumption that all crystals produced in my model are sulfur-free, and no crystals such as sulfide or anhydrite are formed. Sulfides (or sulfates depending on oxygen fugacity) are common, even in silicic magmas, but generally as a minor phase ($\ll 1$ modal %) or sometimes trapped within other minerals (which prevents further interactions with the melt and vapor). In this section, I discuss the merits and limitations of this ($K_s^* = 0$) assumption and discuss how sulfur partitioning would be affected by the presence of S-bearing phases under different scenarios. In Fig. 2.5, I consider schematically different evolution paths for the sulfur concentration in the melt during the crystallization of silicic magmas. I explore various scenario depending on the initial sulfur concentration (below and above the sulfide saturation limit C_s'), and the timing of the onset of water vapor exsolution during crystallization. I take sulfide as an example for S-bearing minerals in this conceptual argument, but it could apply similarly to sulfates. I define χ_c as the critical crystallinity at which vapor bubbles exsolve and χ_s as the crystallinity when the sulfur concentration in the melt reaches saturation with respect to sulfides.

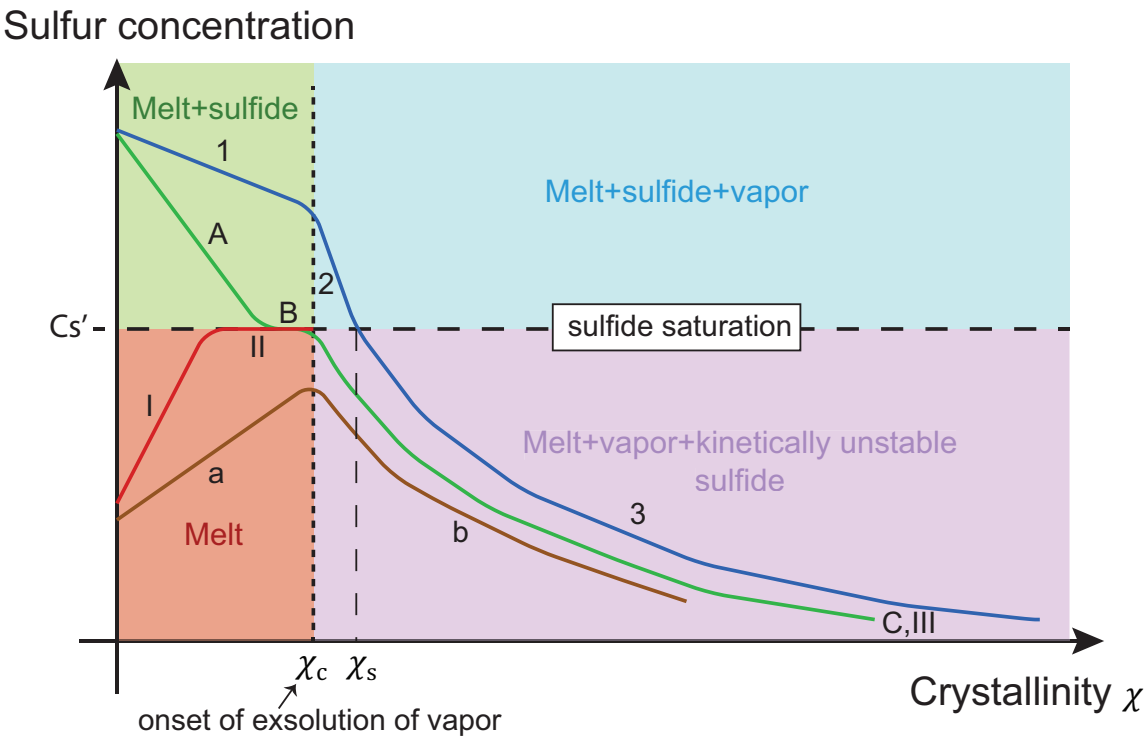

Figure 2.5: A qualitative description of the different evolution paths for the sulfur concentration in the melt during the crystallization of silicic magmas.

1. Magmas with initial sulfur content below the solubility of sulfides ($C_0 < C'_s$).

   (a) Path a-b-c in Fig. 2.5. The sulfur concentration in the melt remains below the solubility of sulfur (a-b). As the magma crystallizes S-free phases and before it becomes saturated with water, the S-content dissolved in the melt increases. As the melt becomes saturated with water at χ_c, sulfur strongly partitions into to growing bubbles and the melt sulfur concentration drops with crystallinity. This is the case I studied with my isobaric degassing model.

   (b) Path I-II-II in Fig. 2.5 where $\chi_s < \chi_c$. Initially, crystallization leads to an increase in sulfur concentration in the melt as for the previous case up to χ_s. In this particular scenario, however, the solubility of sulfur is reached at lower crystal content than that for water ($\chi_s < \chi_c$). After the exsolution of vapor bubbles, the sulfur content decreases below C'_s (the solubility of sulfides) and sulfur mass transfer results in an uptake of sulfur by vapor bubble from the melt and possibly a flux of sulfur from sulfide breakdown back into the melt. The latter process may be kinetically-limited and may lead to the transient coexistence (out of equilibrium) of vapor bubbles and sulfides in the magma.

2. Magmas with an initial sulfur concentration above the solubility of sulfides ($C_0 > C'_s$).

   (a) $\chi_s < \chi_c$ (A-B-C). As the sulfur concentration in the melt is initially above the solubility of sulfides, sulfides crystallize out of the magma from the onset and lead to a decrease in sulfur content in the melt. The sulfur content in the melt decreases to C'_s before the exsolution of water vapor (χ_c). After χ_c, water vapor takes up sulfur from the melt and the melt concentration decreases below the solubility of sulfides which leads to a chemical disequilibrium and the breakdown of sulfides during subsequent exsolution (similar to path I-II-III).

   (b) $\chi_c < \chi_s$ (1-2-3). Sulfides form from the onset, but either the sulfur content in the melt is large enough or the amount of dissolved water is large enough that the sulfur concentration remains above C'_s as second boiling starts (χ_c). In this particular scenario, the three phases, melt+sulfides+vapor, can coexist and

exchange sulfur up until the end of the path 2. The concurrent crystallization of sulfides and exsolution of water vapor leads to an significant decrease in sulfur in the melt, down to C'_s. From then on (path 3) the net mass flux of sulfur is towards the vapor phase only, because sulfides are no longer at equilibrium with the melt.

Depending on the kinetic rate of sulfide breakdown there are two configurations under which vapor bubbles and sulfides can co-exist. First, they can coexist transiently (if the breakdown is slow), see paths b, C, 3, III in Fig. 2.5. In this context, the sulfides are not growing and the partitioning of sulfur between the melt and the vapor phase follows the assumption sulfur being incompatible with the crystal phases and compatible only with vapor. The second possibility, is to start with a magma that contains a large amount of sulfur (significantly above the solubility of sulfides) and enough water so that $\chi_c < \chi_s$. In that case the vapor and sulfide phases can coexist in an equilibrium state over a finite range of crystallinity (see path 2 in Fig. 2.5). That range in crystal content is most likely narrow, because both sulfides and vapor will consume rapidly the sulfur contained in the melt to a point where it decreases below the solubility of sulfides.

In my simulations of sulfur partitioning during second boiling, I focus on the most common paths b, C, 3 or III where the only phase actively extracting sulfur from the melt is vapor. This is not without saying that some sulfides can survive and be present along those paths, but they are not growing (sequestering more sulfur as crystallization proceeds) and they either decompose and deliver back their sulfur into vapor (either via the melt or if they are wetting directly to bubbles) or will keep some sulfur trapped in a sulfide phase that will not contribute to the measured sulfur released to the atmosphere.

2.3 Sulfur degassing in magmas

2.3.1 Syn-eruptive sulfur degassing

Decompression-driven exsolution and degassing are inherent to eruptions. Syn-eruptive sulfur exsolution is explicitly accounted for in the definition of the excess sulfur ratio (Eq. 2.1) and therefore cannot be the cause for the large excess sulfur ratio. However, its overall

contribution to the sulfur mass balance is important because it will provide constraints on the contribution from other process. To this end I use the bubble growth model described in Sec. 2.2.2.1. It is commonly accepted that water exsolution is transport-limited during bubble growth under explosive eruption conditions (fast decompression rates) [97]. The aim of my calculations is to quantify the amount of sulfur that can partition into bubbles during decompression. As an illustration of the results, I discuss a calculation inspired by the 1991 eruption at Mt Pinatubo (silicic magma and rapid ascent rate [141]). Starting with ~ 4 vol.% of pre-eruptive magmatic vapor phase, my model predicts that a maximum of 15 percent of the total SO_2 released in the atmosphere (for Pinatubo, 20 Mt [18]) can be accounted for by decompression at a decompression rate around $5 \times 10^5 \sim 10^6$ Pa/s. Generally, I find that the syn-eruptive degassing of H_2O and, in particular, sulfur by bubbles is kinetically-limited during the ascent of magmas for explosive eruptions due to the short available time and the low diffusion coefficient of sulfur species in silicic magmas [46] (Fig. 2.4). My modeling results indicate that at least 80% of the total sulfur released during explosive silicic eruptions comes from an existing vapor phase before the eruption even starts, consistent with findings of [167,206,210]. As a consequence of this kinetic limitation, a mass balance argument based on equilibrium partitioning between melt and vapor bubbles (Eq. 2.15) would severely overestimate the amount of sulfur that is extracted from the melt during an eruption.

2.3.2 The contribution from pre-eruptive sulfur degassing by second boiling

Since syn-eruptive decompression is inefficient for extracting sulfur out of the melt and is considered in the definition of the excess sulfur, another process must control its partitioning into vapor bubbles before the eruption. Crystallization of anhydrous mineral phases under close to isobaric conditions (second boiling) appears as an excellent candidate because: (1) the crystallization process is slow (controlled by the cooling rate of the magma body) and therefore less likely to be diffusion-limited even for sulfur and (2) arc silicic magmas are typically volatile saturated around their liquidus temperatures in sub-volcanic magma reservoirs [207]. The excess sulfur in a closed system defined in Eq. 2.1 can be recast in a

more compact and traditional form

$$E = \epsilon + 1, \quad \epsilon = \frac{M_{s,b}^{MR}}{M_{s,b}^{dec}} \approx \frac{M_{s,b}^{2nd}}{M_{s,b}^{dec}} \tag{2.20}$$

if I assume that the process that leads to pre-eruptive sulfur loading into bubbles in second boiling, thus $M_{s,b}^{MR} \approx M_{s,b}^{2nd}$. my calculations indicate that if the crystallization interval in the presence of a volatile phase is $>$ 20 vol.% then second boiling can account for a factor of 10 or greater of excess sulfur ratio (E) (Fig. 2.6). I find that most of the range of excess sulfur ratio measured for silicic explosive eruptions can be produced by up to about 20 vol.% crystallization in a volatile-saturated magma reservoir. This does not preclude other processes to play a role on the sulfur accumulation in bubbles before the eruption, but highlight that closed-system processes associated with second boiling are able to close the sulfur mass balance in crystal-rich ($>$ 20 vol.%) silicic eruptions in arcs. From a dynamical standpoint the relative importance of second boiling also depends on the ability of the magma to retain its vapor bubbles during crystallization. On the basis of multiphase numerical calculations, I observe that vapor bubbles can accumulate in crystal-poor regions due to hydrodynamic interactions among bubbles and convective currents when magma crystallinity remains $<$ 50 vol.% [42, 77, 78, 145, 146].

There is an additional fundamental consequence to second boiling on the melt inclusion record. This argument will affect the predicted excess sulfur because it impacts M_s^{MI} in Eq. 2.1, which is the amount of sulfur in the magma at the time melt inclusions are trapped. Under volatile saturated conditions, the melt becomes more S-depleted as crystallization proceeds (as expected from Fig. 2.5) and my calculations show that low temperature mineral phases (e.g., quartz) will sample a melt that is significantly depleted in sulfur. These trends have been reported for a single eruption event when comparing MIs in different hosts (Fig. 2.7a) [38, 207]. There are two plausible explanations for the negative-correlation between SiO_2 and sulfur in a given magmatic system: (1) the crystallization of S-rich phases such as anhydrite or sulfides and (2) the removal of sulfur by vapor bubbles during second boiling. Interestingly, the decrease in sulfur content in a silicate melt saturated with anhydrite or sulfides is constrained thermodynamically to follow the solubility of these phases,

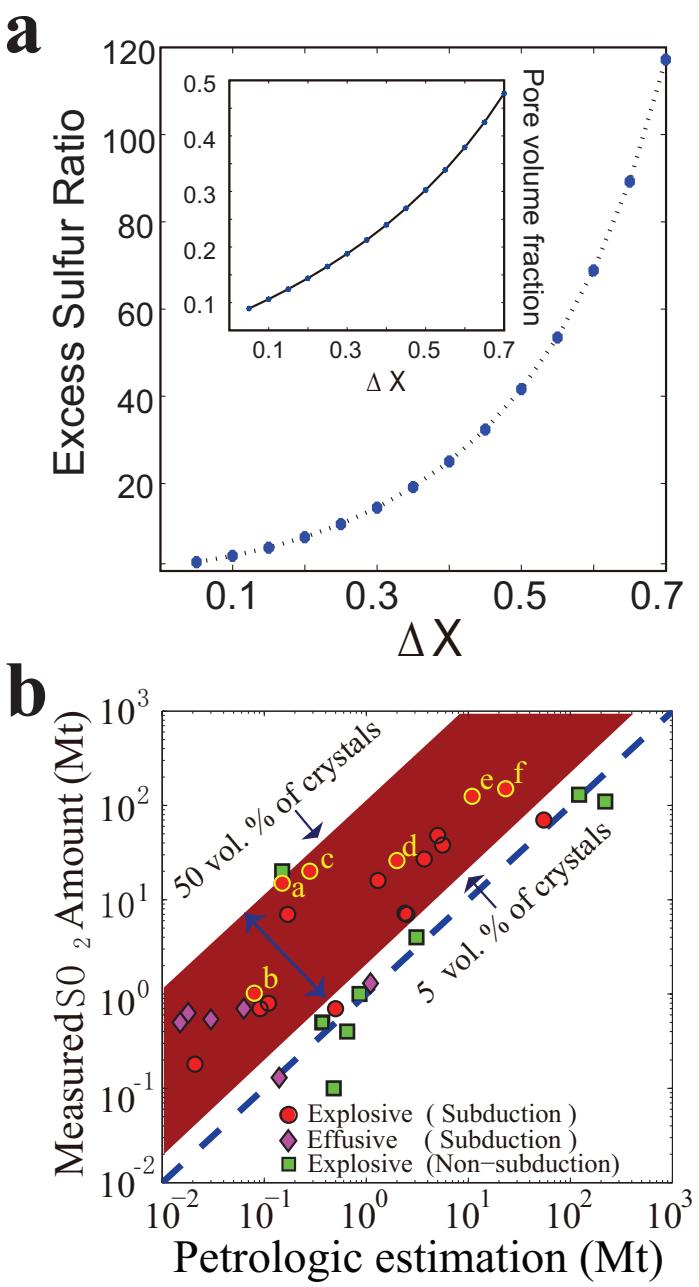

Figure 2.6: (a) The excess sulfur ratio E and bubble volume fraction increase with the volume fraction of crystals that are crystallized during second boiling. I obtain the excess sulfur ratio E here by assuming complete syn-eruptive degassing (setting the syneruptive sulfur degassing efficiency $f = 1$). (b) Reported excess sulfur ratio from eruptions from [177], compared with the range of excess ratio I find in my simulations. The measured SO_2 is derived either by satellite remote sensing or ice-core data. The dark blue dashed trend represents the 1:1 no excess line. The shaded red region encompasses my second boiling results; the lower and higher bounds are calculated using $\Delta\chi$ of 5 vol.% and 50 vol.%, respectively. The red circles represent the eruptions in Tabs. 2.1 and 2.2 from top to bottom as (a–f).

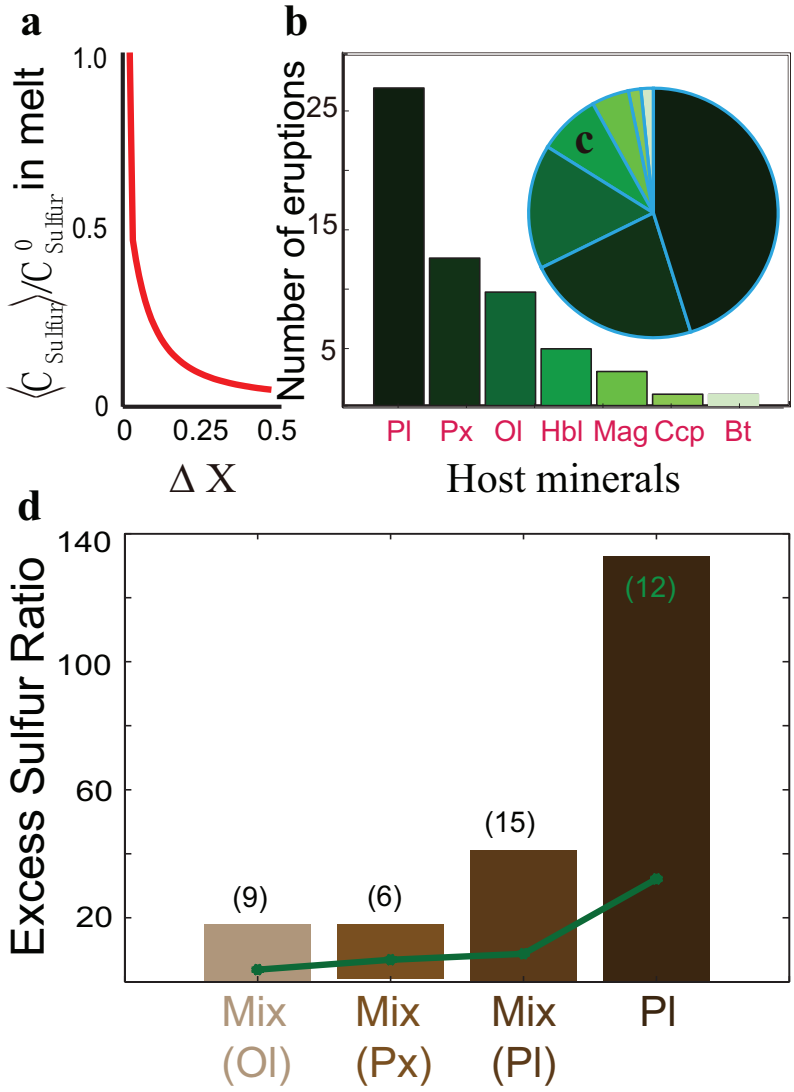

Figure 2.7: The evolution of the average sulfur concentration in the melt during second boiling and statistical studies of previous excess sulfur results. (a) Average sulfur normalized concentration in the melt $\langle C_{Sulfur} \rangle / C^0_{Sulfur}$ against crystallinity. (b–c) Common mineral hosts for MIs (data from Tab. 2.5). (d) Excess sulfur ratio E for 31 eruptions from volcanoes listed in Tab. 2.5. Mix olivine (Ol) indicates studies that used olivine and other host minerals; Mix pyroxene (Px) and Mix plagioclase (Pl) used a mixture of pyroxene or plagioclase, respectively with other phases. The green curve shows the average excess sulfur ratio recorded in each group.

which predicts greater sulfur concentrations in silicic melts at oxidizing conditions than observed in these late MIs. On the contrary, sulfur is a trace element in vapor bubbles and its partitioning is not limited by sulfur solubility. For instance, MIs trapped in quartz in the Toba Tuff [28] or Cerro Galan (this study) record sulfur levels that are below the solubility of sulfur (anhydrite) in these magmas, suggesting an influence of second boiling behind sulfur loss from the melt in these shallow magma reservoirs (Fig. 2.7b–d). As I see from M_s^{MI} in Eq. 2.1 and Fig. 2.7, the choice of host of melt inclusions is also important to determine and interpret the excess sulfur. Consequently, in order to yield a more accurate estimate of the mass balance of sulfur in shallow magma bodies, it is fundamental to determine the timing of the trapping of MIs. When considering melt inclusions that do not suffer from considerable post-entrapment leakage, the wide range in sulfur content that is sometimes observed for a given magmatic system can be used qualitatively as a proxy for the stage at which the melt inclusions have been trapped (Fig. 2.7b–d).

2.3.3 S-bearing minerals breakdown

Another source for sulfur in magmas comes from the decomposition of S-bearing minerals such as as pyrrhotite in reduced magmas [211] and anhydrite in oxidized magmas [110] illustrated in trends 3, III, b, and C in Fig. 2.5. These minerals are considered transiently stable if $\chi > \chi_s$, and resorb as the magma exsolves an aqueous fluid phase as shown by the following simplified reactions,

$$\mathrm{FeS(pyrrhotite) + H_2O(m)} = \mathrm{H_2S(g) + FeO(m)} \quad (2.21)$$

$$\mathrm{CaSO_4(anhydrite) + H_2(g)} = \mathrm{SO_2(g) + CaO(m) + H_2O(g)} \quad (2.22)$$

Note that the index (g) stands for the magmatic volatile phase, and the (m) phase stands for the melt phase. In these reactions, the gas phase (g) is to be understood as a dissolved component in the melt. S-bearing mineral breakdown has been proposed to explain the excess sulfur ratio of some eruptions (e.g., eruption of EI Chichón volcano, which is considered as S-saturated [107]).

As sulfide and anhydrite resorption is driven mainly by sulfur redistribution into the exsolving volatile phase, the most important variable required to model this process is the

concentration of sulfur in the volatile phase at anhydrite or pyrrhotite saturation. The experiments of Zajacz et al. [220, 221] have shown that the sulfur content in the volatile phase at $P = 200$ MPa and pyrrhotite saturation is in the 5 to 7 wt.% range from basaltic to dacitic melt compositions. Zajacz et al. [220] has found similar sulfur concentration in the volatile phase in equilibrium with andesite melts at anhydrite saturation (5.5 wt.%). Scaillet and MacDonald [169] reported sulfur concentrations in the range of 4.8 to 16.7 wt.% in the volatile phase in equilibrium with slightly to moderately peralkaline rhyolite melts at anhydrite saturation and $P = 150$ MPa. At pyrrhotite saturation, the same study determined sulfur concentrations in the range of 6.1 to 11 wt.%. Hence, one can state that the sulfur concentration in the volatile phase of an anhydrite- or pyrrhotite-saturated arc magma at upper crustal depth, will broadly fall within the range of 5 to 17 wt.%. To illustrate the efficiency of anhydrite breakdown by second boiling, the first 1 wt.% of volatile phase exsolving from a magma with a bulk sulfur concentration of 2400 ppm would incorporate one third of the total S-budget (assuming 8 wt.% sulfur concentration in the volatile phase). When present, it is therefore a potent process for sulfur partitioning in magmas.

The following conditions are necessary for anhydrite or sulfide breakdown to contribute to the measured excess sulfur ratio: (1) these phases must be present and sequester a portion of sulfur at the time of the trapping of melt inclusions and (2) their breakdown must operate efficiently enough before or during the eruption so that sulfur can diffuse from the melt to the vapor phase before fragmentation. The relevance of anhydrite or pyrrhotite to excess sulfur therefore impinges on the ability of the sulfur released by these phases to diffuse from the melt to bubbles provided that most bubbles do not nucleate on the surface of S-rich minerals, which is a fair assumption in crystal-rich magmas. In other words, the process of sulfur degassing is limited by the kinetics of mineral breakdown and sulfur transport in the melt to bubbles by diffusion.

Assuming that the breakdown occurs during syn-eruptive decompression, Eqs. 2.21 and 2.22 become additional kinetic steps to consider besides the low efficiency of the sulfur diffusion in the melt to bubbles. Based on my calculations for syn-eruptive degassing, I

expect syn-eruptive breakdown during explosive eruptions to be inefficient and to contribute only a small fraction of the total sulfur released to the atmosphere. Hence, it should not contribute much sulfur syn-eruptively, as suggested by the data for the Pinatubo 1991 eruption [84].

If the breakdown of sulfides or anhydrite takes place in the magma reservoir, then it would impact the measured excess sulfur only if sulfur is sequestered in these solid phases at the time the MIs are trapped and is subsequently released by their breakdown as second boiling proceeds. The growth of bubbles by second boiling is prone to scavenge significant amounts of sulfur from the melt, which lowers the sulfur melt concentration (Figs. 2.5 and 2.7a) and drives the reactions Eqs. 2.21 and 2.22 to the right. In that context, instead of the path "melt→ vapor" I modeled in my study, sulfur may follow a path "melt → S-rich crystal phase → melt → vapor" which involves an additional kinetic step (decomposition of S-bearing minerals). However, unless vapor nucleates on S-bearing minerals, the process remains controlled by the diffusion of sulfur in the melt towards the bubbles, which is the aspect my model focuses on. Crystallization-driven exsolution is a slow process and my numerical calculations showed that the efficiency of crystallization to partition sulfur to the vapor is mostly unchanged if I consider a process that lasts 1 year versus thousands of years (it is not kinetically limited). Therefore, considering the long timescale available for sulfur redistribution during crystallization, I expect that my model provides a reliable estimate for the partitioning of sulfur to the vapor, even for cases where sulfides or anhydrite may play an important role on the sulfur mass budget in the magma reservoir, because the transfer of sulfur from S-bearing phases to the melt and its diffusion to bubbles is unlikely to be kinetically-limited under most circumstances in the magma reservoir.

2.4 Concentration analyses of Cerro Galan (2.08 Ma)

The sulfur content in the magma of Cerro Galan (2.08 Ma) shown in Tab. 2.3 is measured by SIMS, while other oxides are obtained by microprobe analyses. Oxides are renormalized to anhydrous values. Major element compositions of melt inclusion glasses were analyzed on the JEOL 8900 electron microprobe at the USGS, Menlo Park, California using a 15 keV,

5 nA, and 10 um beam. Sulfur concentrations were determined using the Stanford-USGS SHRIMP-RG ion microprobe in one session using a 0.8–1.3 nA O_2^- primary beam with 10 kV acceleration and focused to a $\sim$ 25 micrometer diameter spot. During this session, the SHRIMP-RG instrument was tuned to a mass resolution of $\sim$ 7000 in order to resolve any potential isobaric interferences. Positive secondary ions were measured using a single electron multiplier over 3 mass scans with counting times of 2 ($^{30}Si^+$) to 10 sec ($^{32}S^+$). Sulfur concentration was calculated using a best-fit regression to count rate ratios normalized to ^{30}Si versus variable known concentration ratios normalized to wt.% SiO_2 of experimental and natural glass standards [216]. Standards include natural volcanic glasses RLS37, RLS140, RLS76-75 [112], Macusani [105] and synthetic NIST standards 611 and 613 [148]. Standard 2170 (experimental product of Mangan and Sisson, 2000) [117] was used as a secondary standard, using sulfur concentration determined by Wright et al. [216]. All uncertainties in S concentration are external uncertainties. External uncertainties (1 σ) were calculated by propagating errors of standard concentrations and error from repeat analyses through a modified York regression [219]. External uncertainties were greater than internal uncertainties for all samples. Internal uncertainties (1 σ) were calculated from counting statistics using SQUID 2 [106].

2.5 Discussion

My calculations of the kinetics of sulfur during exsolution clearly mark a distinction between silicic crystal-poor ($< 20\%$) and crystal-rich ($> 20\%$) wet magmas. Second boiling can play a important role on the mass balance of sulfur in the latter, as it can even explain excess sulfur ratio of up to two orders of magnitude for some eruptions (Mount St. Helens in 1480 and 1980 and Pinatubo in 1991 as shown in Fig. 2.6b and Tabs. 2.1 and 2.2. My results do not imply that open-system processes do not play an important role on the sulfur mass balance for these systems, rather it means that the yield of second boiling in terms of sulfur partitioning can generate the scale of excess sulfur ratio measured in these eruptions. Conversely, second boiling must play only a secondary role on the sulfur melt-bubble partitioning in crystal-poor magmas (very little crystallization to drive second

Table 2.1: Observed excess sulfur of 3 crystal-rich and 3 crystal-poor eruptions: Mount St. Helens [32, 54], Pinatubo [142], Minoan [178], Katmai [72], and Crater Lake [40, 114]. The superscripts (a–f) correspond to the same labels in Fig. 2.6.

Volcano	**Eruption Year**	**V (km3)**	**Whole-rock composition**	**Crystallinity (vol.%)**	**Excess S [177]**
[a]Mount St. Helens	1480	∼2	Dacite	Dominantly crystal-rich 25%	∼100
[b]Mount St. Helens	1980	<1	Dacite	Dominantly crystal-rich 20-40%	10∼15
[c]Pinatubo	1991	∼10	Dacite	Dominantly crystal-rich 40%	∼70
[d]Minoan	1645 BCE	∼40	Rhyodacite to andesite	Dominantly crystal-poor (10%) but up to <50% in late-erupted scoria	10∼15
[e]Katmai	1912	∼13	Rhyolite to andesite	Dominantly crystal-poor (1-5%) but up to 50% in late-erupted scoria	10∼15
[f]Crater Lake	7700 cal BP	∼50	Rhyodacite to andesite	Dominantly crystal-poor (10%) but up to 70% in later-erupted scoria	5∼10

Table 2.2: Calculated excess sulfur of the eruptions listed in Tab. 2.1 when the syneruptive sulfur degassing efficiency $f = 0.25$ by assuming a decompression rate $\dot{\hat{P}}$ of 2×10^5 Pa/s and the listed 6 magmas reach their H_2O saturation levels after 5 vol.% of crystals are produced. The results show that second boiling can generate large excess sulfur to match the measured excess sulfur for crystal-rich eruptions, while the importance of the open system volatile transport from new recharges provides a more important contribution to the excess sulfur recorded by crystal-poor eruptions.

Volcano	**Eruption Year**	χ **(vol.%)**	$\Delta\chi$ **(vol.%)**	**Calculated Excess S**
[a]Mount St. Helens	1480	25	20	∼32
[b]Mount St. Helens	1980	20-40	15-35	20∼80
[c]Pinatubo	1991	40	35	∼80
[d]Minoan	1645 BCE	10	5	∼8
[e]Katmai	1912	1-5	0	∼1
[f]Crater Lake	7700 cal BP	10	5	∼8

Table 2.3: Concentration analyses of Cerro Galan (2.08 Ma).

Name	n (probe)	wt.% SiO_2	wt.% TiO_2	wt.% Al_2O_3	wt.% FeO	wt.% MnO	wt.% MgO	wt.% CaO	wt.% NaO_2	wt.% K_2O	wt.% Cl	wt.% F	wt.% P_2O_O	wt.% Raw Total	ppm sulfur	1 σ uncrtainty	wt.% H_2O
406N-2	2	77.1	0.09	12.8	0.27	0.04	0.01	0.8	3.5	5.1	0.11	0	0.05	97.41	51	6	2.4
491-B2	2	73	0.11	15.2	0.2	0.05	0	0.6	4.1	6.4	0.14	0.16	0.05	97.94	27	3	1
491-E2	1	72.1	0.04	15.6	0.27	0.05	0	0.5	4.8	6.1	0.21	0.26	0.04	97.05	10	1	
491-E1	2	73.1	0.16	14.9	0.17	0.01	0	0.5	4.4	6.2	0.24	0.19	0.15	99.37	13	1	0.2
491-F1	2	72.2	0.17	15.5	0.19	0.08	0	0.6	4.6	6.3	0.18	0.13	0.08	98.47	26	3	0.3
491-F6	2	72.3	0.13	15.6	0.23	0.04	0	0.7	4.4	6.4	0.19	0.05	0.04	97.94	45	5	
491-F2	2	72.8	0.14	15.4	0.07	0.05	0	0.6	4.3	6.3	0.14	0.13	0.08	98.27	11	1	0.3
491-F5	3	71.8	0.12	15.6	0.44	0.06	0.05	1.1	4.2	6.4	0.18	0	0.1	98.1	49	6	
491-J1	5	75.5	0.06	13.7	0.62	0.06	0.05	1	3.6	5.1	0.18	0.15	0.05	93.37	57	6	0.7
491-B1		73													14	5	
491-F3		73													51	20	
406-I2		73					glass composition not determined for these melt inclusions								6	2	
406-H1		73													10	4	
406-H2		73													6	2	
406-L5		73													6	2	
406-groundmass glass [215]		77.9	0.09	13.1	0.48		0.06	0.8	2.2	5.1	0.18		0.01	95.82	59	23	
406-groundmass glass [215]		77.9	0.09	13.1	0.48		0.06	0.8	2.2	5.1	0.18		0.01	95.82	25	10	

boiling). For eruptions that involved dominantly crystal-poor magmas (Minoan eruption (1645 BC), Katmai (1912) and Crater Lake ($\sim$ 7700 cal BP) in Fig. 2.6b and Tabs. 2.1 and 2.2), large excess sulfur cannot be leveraged by closed system processes and requires transport and accumulation of S-rich bubbles from deeper sources to be the driving factor to close the sulfur mass balance [78, 145, 180].

The 2.08 Ma Cerro Galan ignimbrite ($\sim$ 630 km^3 erupted) is a crystal-rich rhyodacite. It is old enough to prevent the use of remote sensing and ice core analysis to infer the amount of sulfur released during the eruptions [226]. The petrological method is the only way to estimate the amount of sulfur released to the atmosphere and the potential impact of this eruption on climate. The volumetrically dominant white pumice (95 vol.%) in the Cerro Galan ignimbrite contains 44–57% phenocrysts on a vesicle-free basis [215]. Quartz crystals separated from two white pumice clasts were analyzed for FTIR spectroscopic analysis in a previous study [215]. These same doubly polished quartz wafers were mounted in epoxy mounts in order to analyze major element and sulfur compositions. The sulfur content of these melt inclusions measured by the SHRIMP-RG ranges from 6–57 ppm, which is at or barely above the detection limit and are equivalent to the sulfur concentration measured in the GG (25–59 ppm, Tab. 2.3). An uncorrected traditional petrologic estimate for sulfur would therefore suggest that only a very limited amount of SO_2 was released during the eruption.

In order to establish the contribution of second boiling to degassing, I model the isobaric crystallization of the magma at 245 MPa and = NNO+1.5 with an initial water content of 6 wt.% using Rhyolite-Melts [64] (sample input parameters and output crystallinity are shown in Tab. 2.4), from which 20–40 vol.% crystallization is estimated to be produced during second boiling. My second boiling simulations imply that approximately about 90–95 % of sulfur has been depleted from the melt by the time the melt inclusions are trapped by their host (quartz), and the estimated excess sulfur ratio E ranges from 32 to 100 when I assume a syn-eruptive decompression rate of 2×10^5 Pa/s ($f = 0.25$). In order to estimate the amount of sulfur released during the eruption of Cerro Galan (2.08 Ma), I also need to estimate the sulfur concentration in the primitive magma. Assuming an initial sulfur concentration of 500

ppm reasonable for sulfate saturated dacite to rhyodacite, I estimate that around 1 Gt vapor sulfur could have been stored by bubbles before the onset of the eruption. Thus, by ignoring the sulfur contribution associated with syneruptive decompression (contributes only a few percent of the total S) as well as additional unconstrained open-system contributions, second boiling alone would result in the release of about 1 Gt SO_2, an amount comparable to Bishop Tuff, 0.76 Ma [206] and Toba YTT, 75 ka [28]).

2.6 Conclusions

In this chapter, I present the results of numerical calculations of sulfur partitioning during bubble growth in magmas and combine them with excess sulfur datasets to constrain the relative importance of closed and open system degassing at active volcanoes. These calculations highlight that the dominant process that leads to the build-up of large excess sulfur ratio are different for eruptions driven by crystal-rich and crystal-poor silicic magmas. For instance, second boiling has the potential yield to explain the excess sulfur ratio observed for magmas that underwent $>$ 10–20 vol.% crystallization under volatile-saturated conditions. However, the addition of S-rich bubbles from mafic recharges or from an underlying crystal mush is necessary to close the sulfur mass balance when the primitive magma does not store sufficient sulfur or in silicic crystal-poor magmas where second boiling is not sufficient to pump enough sulfur into the bubbles [145].

Table 2.4: White Pumice from Cerro Galan Ignimbrite and sulfur concentration from Tab. 2.3. The whole-rock composition, crystallinity, and the vesicularity of the white pumice are shown by Wright et al. [215]. The sulfur concentration data are summarized from Tab. 2.3 in this study.

White Pumice - CG257 [215]				
Whole-rock Composition	SiO_2	69.7	MgO	1.26
	TiO_2	0.62	CaO	2.59
	Al_2O_3	15.45	Na_2O	3.31
	FeO	3.05	K_2O	4.58
	MnO	0.05	P_2O_5	0.2
Crystallinity	44–57 (vol.%)			
Vesicularity	24–69 (vol.%)			
S concentration				
Groundmass Glass	25–59 (ppm)			
Melt Inclusion	6–57 (ppm)			

Table 2.5: Melt inclusion list in Fig. 2.7(b–d) [177]. Excess sulfur less than 1 (marked by '*') could be caused by the underestimate of remote sensing and ice-core measurements (Pl: Plagioclase Px: Pyroxene Ol: Olivine Hbl: Hornblende Mag: Magnetite Ccp: Chalcopyrite Bt: Biotite).

Eruptions	Pl.	Px.	Ol.	Hbl.	Mag.	Bt.	Excess sulfur
Agung, 1963 [171]	✓		✓				~ 3
Arenal, 1985–1996 [187]	✓	✓					~ 1
Bezymianny, 1956 [140]	✓						~ 3
Chikurachki, 1986 [67]	✓	✓	✓				~ 1
EI Chichon, 1982 [109]	✓			✓			~ 41
Eldgja, 934 [195]	✓						$\sim 0.5^*$
Galungyung, 1982–1983 [34]	✓		✓				~ 7
Hekla, 1104 [38]	✓						~ 130
Hekla, 1980 [173]	✓		✓				~ 1
Hekla, 2000 [173]	✓		✓				$\sim 0.2^*$
Mt. St. Helen, 1480 [140]	✓						~ 100
Mt. St. Helen, 1980 [38]	✓						~ 13
Mt. St. Helen, 1980–1986 [38]	✓						~ 33
Huaynaputina, 1600 [30]	✓			✓			~ 10
Katmai, 1912 [209]	✓	✓					~ 13
Kilauca, 1992–1997 [38]	✓		✓			✓	~ 1
Krafla, 1984 [173]	✓		✓				$\sim 0.6^*$
Krakatau, 1885 [113]	✓	✓			✓		~ 7
Laki, 1783 [196]	✓						~ 1
Lascar, 1989 [122]		✓	✓	✓			~ 18
Mauna Loa, 1984 [173]	✓		✓				~ 1
Minoan, 1645 B.C. [38]	✓						~ 11
Pinatubo, 1991 [58]	✓						~ 71
Redoubt, 1989–1990 [57]	✓	✓		✓	✓		~ 9
Redoubt, 1990 [57]	✓	✓		✓	✓		~ 35
Ruiz, 1985 [178]	✓	✓					~ 8
Santa Maria, 1902 [140]		✓					~ 7
Soufriene, 1995–1998 [41]	✓						~ 11
Tambora, 1815 [170]	✓						~ 1
Taupo, 181 [140]		✓					~ 12
Unzen, 1991–1994 [166]		✓		✓		✓	$\sim 0.9^*$

CHAPTER III

MAGMA SYN-ERUPTIC ASCENT HISTORY AND VOLATILE DEGASSING

In this chapter, a similar numerical approach for syn-eruptive degassing as the model presented in Chap. 2 and study the volatile (H_2O and CO_2) diffusion profiles around bubbles. As magmas ascend to the surface, the rate of decompression is expected to increase as they approach the vent, because of the increasing buoyancy of the more vesicular magma. The question that this chapter focuses on is whether these volatile profiles after eruption can be used to constrain time-dependent magma decompression rates. The numerical simulations cover a wide range of of ascent time, magma decompression paths, and pre-eruptive volatile compositions. A significant difference with the model of bubble growth in the previous chapter is that I simulate the H_2O–CO_2 coupled system which influences the kinetics and solubility of each gas species. The content of this chapter is now under review in Journal of Geophysical Research: Solid Earth [188].

3.1 Introduction

Characterizing the rate of magma's ascent to the surface remains a central question to understand the behavior of volcanic eruptions. Several kinetic processes, including phenocryst breakdown and volatile diffusion, have been suggested as tracers for the magma ascent rate [4, 81, 102, 163, 197]. These kinetic processes are suitable to study a range of decompression rates depending on their inherent time scale.

For eruptions with low averaged decompression rates (e.g., lower than 2–9 kPa/s), Rutherford and Hill [163] and Anderson [4] suggest constraining the decompression rate with breakdown rims around amphibole crystals, or H_2O concentrations dissolved in hourglass melt inclusions in quartz. For eruptions involving intermediate decompression rates (e.g., between 1 kPa/s and 100 kPa/s), Liu et al. [102] proposed a technique that integrates the measurements of CO_2 diffusion profiles in quartz-hosted and microlites-free melt

pockets with a model assuming constant decompression rates and volatile equilibrium between bubbles and melts. Shortly after, Humphreys et al. [81] developed an approach with back-scattered electron microscope to correlate gray-scale intensity to H_2O concentration in plagioclase-hosted melt tubes. Assuming equilibrium condition outside the melt tube, the authors were able to provide an upper bound for the decompression rate given that (1) their values only constrain an average magma decompression rate and (2) that the decompression rate is low enough (< 0.25 MPa/s) to satisfy equilibrium condition. For high decompression rates (e.g., > 2 MPa/s), Toramaru [197] developed a methodology based on the bubble number density in erupted clasts, and was able to infer ascent rate of hundreds of meters per second for Plinian eruptions.

While phenocryst breakdown can provide constraints on low decompression rates (< 1 kPa/s), volatile kinetics have been used to constrain fast decompression (> 1 kPa/s) in explosive eruptions. Although volatile exsolution and diffusion are both pressure-sensitive processes, one faces two important challenges when relying on gas exsolution to constrain magma decompression rates. First, in eruptions where the decompression rate of the magma can exceed 0.25 MPa/s, most volatiles cannot maintain equilibrium partitioning between melt and bubbles, especially for volatiles species diffusing slower than H_2O, such as CO_2, S, Cl, etc [1, 9, 55, 208]. Second, because of feedbacks between decompression and buoyancy, magmas do not actually ascend under a constant decompression rate, as discussed in several studies such as Refs. [81, 102] and shown by conduit model simulations (e.g., Refs. [63, 121, 143], among others).

In this study, I focus my attention on whether diffusion profiles of H_2O and CO_2 around bubbles record faithfully time-dependent decompression rates in silicic magmas. In other words, can I use diffusion profiles around bubbles to go beyond the approximation of a constant decompression rate? Using numerical simulations and considering a wide range of eruption durations, magma decompression paths, and pre-eruptive volatile compositions, I find that the disequilibrium of CO_2 between bubbles and melt provides constraints on the total magma ascent time at decompression rates > 0.25 MPa/s. I also find that the assumption of a constant decompression rate generally yields an overestimated average

decompression rate.

3.2 Methods

3.2.1 Decompression parameterization

The goal of this study is to test whether kinetics effects recorded in diffusion profiles of H_2O and CO_2 around bubbles, post-decompression, carry any information that can be used to point to and perhaps quantify deviation from constant decompression rates. During magma ascent, decompression paths are complex because they reflect coupled non-linear processes and feedbacks associated with exsolution, changes in rheology and increasing buoyancy as magmas migrate closer to the surface. Numerical models of conduit magma flow dynamics have shown, to a first order (and within the assumptions made in these models), that magmas first ascend under near constant decompression rates (decompression and ascent rates rapidly become non-linearly related, as the density of the magma changes during ascent). As the magma vesicularity increases, a positive feedback between degassing and ascent rate causes a non-linear increase in decompression rate, which further accelerates either until fragmentation, or for effusive eruptions, until the magma is extruded at or above the surface. To a first order, these typical non-linear decompression paths, reported in many studies [62, 63, 121, 143, 153], can be parameterized with a relatively slow and near constant decompression rate early on, with an acceleration up to the point of disruption. I develop a simple parameterization that captures these essential features by introducing only 2 free parameters, the duration of the decompression event τ and the degree of non-linearity of the decompression path λ

$$\frac{P_a\left(t\right)}{P_i} = 1 - \frac{e^{\lambda\left(\frac{t}{\tau}\right)} - 1}{e^{\lambda} - 1}, \tag{3.1}$$

which, written as a decompression rate, reads

$$\frac{dP_a}{dt} = \frac{\lambda P_i e^{\frac{\lambda t}{\tau}}}{e^{\lambda} - 1} \tag{3.2}$$

where P_a is the ambient pressure and t denotes time. P_i and τ are the magma chamber pressure and total magma ascent time, respectively. As $\lambda \to 0$, Eq. 3.1 leads to a linear decompression $P_a/P_i = 1 - t/\tau$. Throughout the remainder of this chapter, "$\lambda = 0$" refers to

linear decompression paths. As λ increases, decompression is initially slow and accelerates as the magma approaches atmospheric pressure (Fig. 3.1a). To better illustrate how the magma decompression rate varies along these paths, I calculated the average decompression rate $\left\langle \dot{P}_a \right\rangle$ when magma moves from an arbitrary pressure P_s to the atmospheric pressure P_0, where $P_0 \leq P_s \leq P_i$. From Fig. 3.1b I see that $\lambda = 7$ can yield $\left\langle \dot{P}_a \right\rangle$ up to 6 times greater than $\left(\dot{P}_a\right)_L$, the time-averaged decompression rate for $\lambda = 0$ and the same τ.

3.2.2 Bubble dynamics model

Both H_2O and CO_2 kinetics are considered in a homogeneous bubble growth model, in which bubble growth is driven by syn-eruptive decompression and volatile diffusion (Fig. 3.2). In the model, I simulate the volatile diffusion in the melt (Eq. 3.3) and the bubble growth (Eq. 3.4).

$$\frac{\partial C_x}{\partial t} + v_m \frac{\partial C_x}{\partial r} = \frac{1}{r^2}\frac{\partial}{\partial r}\left(r^2 D_x \frac{\partial C_x}{\partial r}\right), \tag{3.3}$$

$$P(t) - P_a(t) = \frac{2\sigma}{R(t)} + 4\frac{\dot{R(t)}}{R(t)}\eta_{eff} \tag{3.4}$$

where t is time, r is the radial distance from the bubble/melt interface, C is the volatile concentration in the melt, D is the volatile diffusion coefficient, the subscript "x" denotes either H_2O or CO_2, v_m is the melt radial velocity, R is the bubble radius, σ is the bubble interfacial tension, P is the bubble pressure, P_a is the ambient pressure, $\dot{R(t)}$ is the growth rate of the bubble, and η_{eff} is the effective viscosity of the melt. Eq. 3.3 describes the local mass balance of volatiles while Eq. 3.4 describe the hydro-dynamical force balance for a bubble/melt interface. The periodic cell approach to bubble growth is inspired by the seminal work of Proussevitch et al. [152], however, for numerical stability, I follow the scheme developed by Forestier-Coste et al. [44] and later applied to sulfur degassing in silicic magmas by Su et al. [189]. A detailed explanation of the numerical algorithm and closure relationships is provided in Chap. 2 and Ref. [189]. Eqs. 3.3 and 3.4 are closed by a mass balance statement for the entire bubble/melt system,

$$\frac{d}{dt}M(t) = 4\pi\rho_m F|_{r=R(t)}, \tag{3.5}$$

which describes the change of the mass (M) of a bubble which balances the volatile mass flux (F) at the bubble/melt interface ($r = R(t)$) where ρ_m is the density of melt.

The system is initialized with spatially periodic cells, each cell consisting of a bubble and a surrounding melt region as illustrated in Fig. 3.2. The equation of state of the gas within the bubbles is described by the ideal gas law. A no flux boundary condition is set between neighboring cells. At the bubble/melt interface, I use the empirical mixed solubility model (Eqs. 3.6 and 3.7) for H_2O–CO_2 in rhyolitic magmas [104] as the boundary condition,

$$\begin{aligned} H_2O(\text{wt.}\%) &= \frac{(354.94P_w^{0.5} + 9.623P_w - 1.5223P_w^{1.5})}{T} + 0.0012439P_w^{1.5} \\ &\quad + P_{CO_2}(-1.084 \times 10^{-4}P_w^{0.5} - 1.362 \times 10^{-5}P_w), \qquad (3.6) \\ CO_2(\text{ppm}) &= P_{CO_2}\frac{(5668 - 55.99P_w)}{T} + P_{CO_2}(0.4133P_w^{0.5} + 12.041 \times 10^{-3}P_w^{1.5}), \qquad (3.7) \end{aligned}$$

where P_w and P_{CO_2} (in MPa) are partial pressures of H_2O and CO_2 in the bubble ($0 < P < 500$ MPa), respectively, and $973 < T < 1473$ is the temperature in Kelvin.

In the model, the total H_2O diffusivity is set to [131]:

$$D_{H_2O}(\text{m}^2/\text{s}) = \exp\left(-14.26 + 1.888P - 37.26X - \frac{12939 + 3626P - 75884X}{T}\right), \qquad (3.8)$$

where P is in GPa, T is in Kelvin, and X is the mole fraction of total H_2O dissolved in the melt on a single oxygen basis. This H_2O diffusivity law works for normal metaluminous and peraluminous rhyolite melts when $676 \leq T \leq 1900$ K and $P \leq 1.9$ GPa. I use the total CO_2 diffusivity ($673 \leq T \leq 1773$ K and $P \leq 1.5$ GPa) [225],

$$D_{CO_2}(\text{m}^2/\text{s}) = \exp\left(-13.99 - \frac{17367 + 1944.8P}{T} + C_w\frac{855.2 + 271.2P}{T}\right), \qquad (3.9)$$

where C_w is the water content dissolved in the melt in wt.%.

The model is designed to track volatile kinetics in a H_2O–CO_2 coupled system. It allows non-equilibrium degassing and time-dependent decompression rate. However, the model does not include new bubble nucleation events, the effect of syn-eruptive crystallization, and bubble/melt separation. These issues will be addressed in future studies.

I ran over one thousand decompression simulations over a wide range of initial gas CO_2 content, magma decompression duration τ and decompression path λ. The parameters

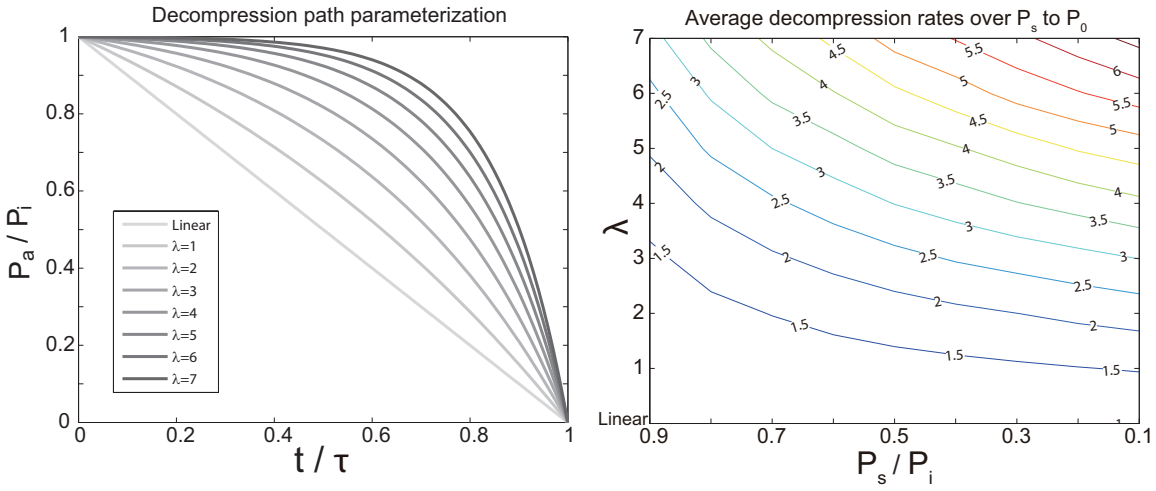

Figure 3.1: (a) With a greater λ, the decompression path deviates more from the linear path. Such non-linear paths are motivated by the fact that magmas tend to accelerate as they rise to the surface due to an increased buoyancy (bubble growth and nucleation). (b) For each magma ascent time and ascent path, the average magma decompression rates over different pressure intervals to the surface are calculated. The present contours are in unit of the decompression rate obtained for the corresponding linear ascent path.

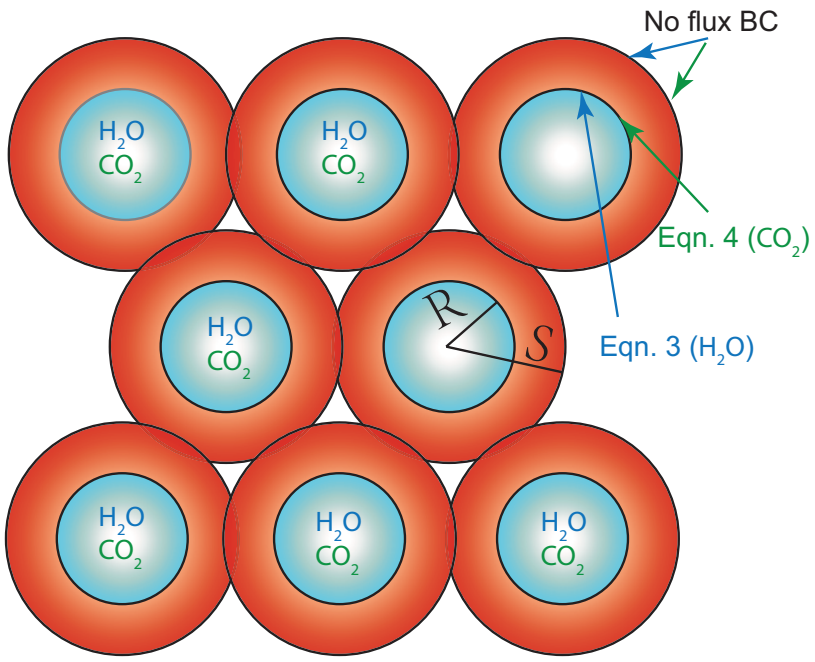

Figure 3.2: An illustration of the homogeneous bubble growth model based on Ref. [44]. Each cell includes a bubble (the lighter area inside the shell) and melt (the red shell) surrounding the bubble . The gas within bubbles is comprised of H_2O and CO_2. Between each two adjacent cells, no flux boundary conditions are set, while at the bubble/melt interface, the solubilities laws defined in Eqs. 3.6 and 3.7 are applied.

tested in my simulations are listed in Tab. 3.1. The magma chamber pressure P_i is fixed throughout the entire simulations, while the value of $X_{\mathrm{CO_2}}$ are varied. For different $X_{\mathrm{CO_2}}$, $C^0_{\mathrm{H_2O}}$, and $C^0_{\mathrm{CO_2}}$ are calculated from Eqs. 3.6 and 3.7, and are set as the initial concentration of H_2O and CO_2 in the melt in order to maintain chemical equilibrium between bubbles and melt before decompression. Following Ref. [207], the H_2O content in rhyolitic melt at 2 kbar ranges from 4 to 6 wt.%, and the concentration of CO_2 is generally < 500 ppm for most silicic magmas, which results in initial $X_{\mathrm{CO_2}} < 60$ wt.% using Eqs. 3.6 and 3.7.

3.3 Results

In this section, I show the impact of the 3 parameters (λ, τ, and X_{CO_2}) on the final vesicularity, the bubble overpressure, the average volatile content in the melt and the degree of chemical equilibrium between bubble and melt after eruption.

3.3.1 Final vesicularity

In explosive eruptions, magma vesicularity can be affected by various factors, including magma composition and tectonic settings. Here, using a fixed initial bubble volume fraction of 4 vol.%, I test how the final magma vesicularity Φ_f varies with the total magma ascent time τ, the initial volatile composition of the magma $X_{\mathrm{CO_2}}$ and the magma's ascent path λ. Fig. 3.3a shows the variation of the bubble volume fraction (vol.%) after eruption as function of the total magma syn-eruptive time τ for conditions: (a) $\lambda = 0$ and $X_{\mathrm{CO_2}} = 10$ wt.%, (b) $\lambda = 4$ and $X_{\mathrm{CO_2}} = 10$ wt.%, (c) $\lambda = 0$ and $X_{\mathrm{CO_2}} = 40$ wt.%. All three curves exhibit increasing Φ_f (from ~ 10 vol.% to ~ 80 vol.%) with longer magma ascent durations τ (from 10 seconds to $\sim$ 2.7 hours). Eruptions with magmas sharing the same initial volatile composition but different decompression paths (cases (a) & (b)) yield different magma vesicularity Φ_f, i.e., Φ_f for case (b)($\lambda = 4$) is about 10 vol.% lower than case (a)($\lambda = 0$). Magmas containing more CO_2 (case (c)) yield a lower final vesicularity Φ_f than their CO_2-depleted counterpart (see case (c) versus (a) where the difference is about 5%). To summarize, for a fixed decompression time τ, the final vesicularity Φ_f is greater for low CO_2 magmas and linear decompression paths ($\lambda = 0$).

Table 3.1: List of major model parameters

P_i	Magma chamber pressure	2 kbar
Φ_i	Pre-erutive bubble volume fraction in the magma	4 vol.%
τ	eruption duration	20 s–5.5 h
λ	non-linearity of magma ascent paths	0–7
X_{CO_2}	pre-eruptive CO_2 in bubbles	0–60 wt.%
$C^0_{H_2O}$	pre-eruptive H_2O concentration in the melt	4.4–6.1 wt.%
$C^0_{CO_2}$	pre-eruptive CO_2 concentration in the melt	0–470 ppm

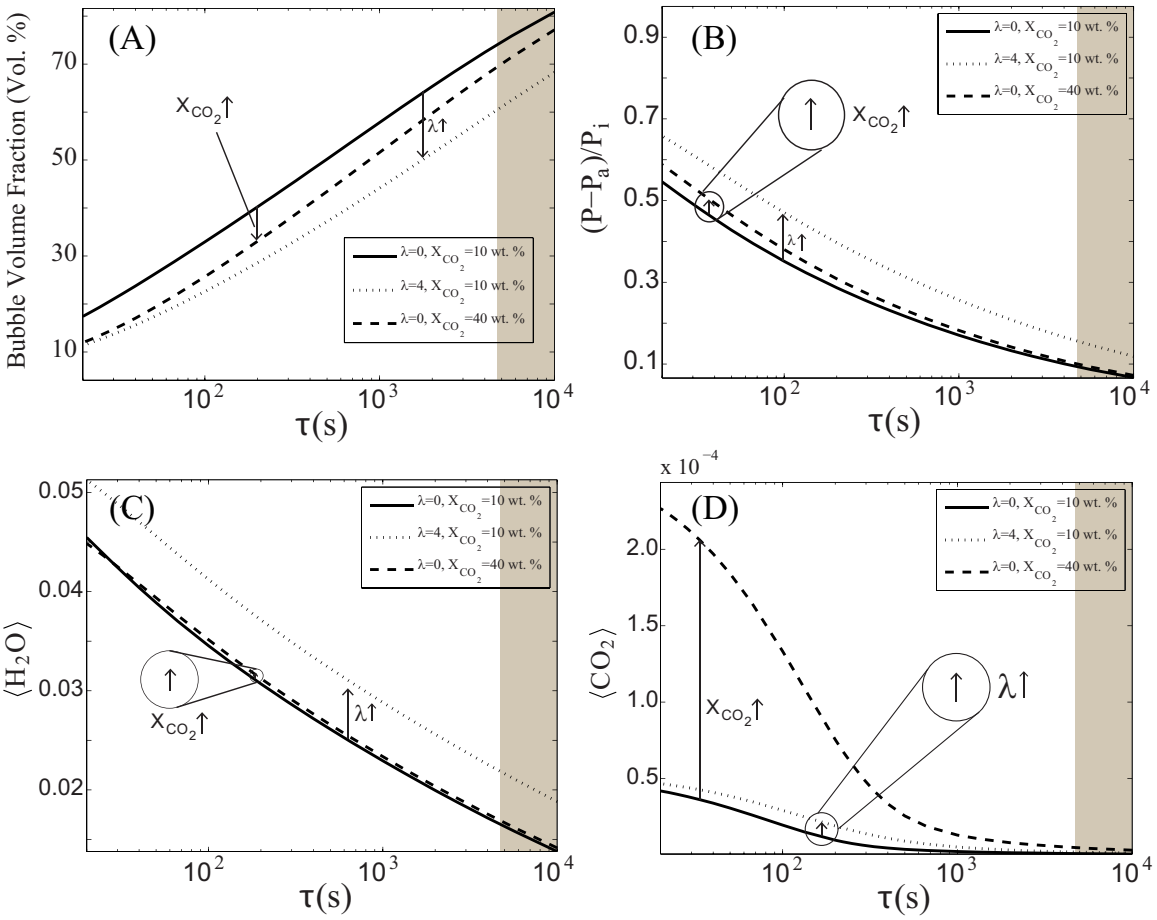

Figure 3.3: The variation of the bubble volume fraction vol.% (A), the bubble overpressure $(P - P_a)/P_i$ (B), the average water concentration $\langle H_2O \rangle$ within melt (C), and the average water concentration $\langle CO_2 \rangle$ within melt (D) after eruptions with respect to the total magma syn-eruptive time τ for $\lambda = 0{,}4$ and $X_{CO_2} = 10$ wt.%, 40 wt.%. The shaded regions highlight decompression simulations that led to final vesicularity beyond 74%, where fragmentation processes are likely to have truncated the decompression paths. I focus on cases where fragmentation is less likely to interrupt the decompression path.

3.3.2 Bubble Overpressure

Bubble overpressure is defined as the difference in pressure between bubbles (P) and the melt (P_a), and can play a major role to drive bubble nucleation [97] and magma fragmentation [223]. Overpressure builds up when magmas ascend fast enough that the bubble pressure can not diffuse out rapidly by creep in the surrounding melt shells. As demonstrated in Fig. 3.3b, overpressure is more prominent in eruptions with faster ascent. Although I do not explicitly evaluate bubble nucleation and fragmentation in this work, I test how the overpressure builds up at the final stage of eruption for a range of τ, X_{CO_2}, and λ conditions. The curves in Fig. 3.3b represent variations of the normalized overpressure $(P-P_a)/P_i$ after eruptions for the same 3 cases as in Fig. 3.3a. P_i is the pressure in the magma chamber. Increasing λ or $X_{\mathrm{Co_2}}$ both cause increases in overpressure.

3.3.3 Average H_2O and CO_2 content in the melt

The H_2O and CO_2 content in the melt are quantities commonly measured from volcanic samples. Rutherford et al. [161, 162] have suggested that analytical data on the abundance of the different volatile species lost from the melt to the gas phase during an eruption may record the rate of magma ascent to the surface. Longer ascent time τ, when volatiles have more time to diffuse into bubbles, yield a depletion of H_2O and CO_2 in the surrounding melt, while increasing values of λ or X_{CO_2} result in more H_2O and CO_2 left in the melt after decompressions (Figs. 3.3c and 3.3d).

3.3.4 Degree of chemical equilibrium between bubble and melt

I analyzed all post-eruption H_2O and CO_2 diffusion profiles within the parameter space of this study. Examples of these post-eruption profiles for H_2O and CO_2 are shown in Fig. 3.4, a magma rising at a constant speed ($\lambda = 0$) and a range of total ascent time τ. The concentrations of H_2O and CO_2 have been normalized with their solubility after eruption ($P_a = P_{\mathrm{atm}}$). In Figs. 3.4a and 3.4b, H_2O concentration profiles in the melt display a greater disequilibrium as magmas ascend faster, while the steepness of CO_2 profiles reaches a maximum value around a magma ascent speed of about 20 m/s. For a fixed

total ascent time τ, the extent to which the diffusion of H_2O and CO_2 erases the degree of disequilibrium depends on the non-linearity of the magma ascent path. For greater λ values, the disequilibrium in H_2O between the bubbles and the melt increases (Fig. 3.4c). Fig. 3.4d shows that the behaviour of CO_2 is more complex. For example, considering the total magma ascent time $\tau = 4.2$ min, the degree of disequilibrium for CO_2 is lower for $\lambda = 7$ than $\lambda = 0$. For longer magma ascent durations, the trend is reversed and a highly non-linear decompression path would lead to higher degree of diffusive equilibration for CO_2.

I introduce a parameter δ to quantify the disequilibrium between bubbles and the melt,

$$\delta = \frac{C_{\max} - C_{\min}}{C_{\max}} \tag{3.10}$$

where $C_{\max}$ is the volatile concentration at the boundary between any two adjacent bubble-melt cells in my simulations or the concentration far away from bubbles. $C_{\min}$ is the volatile concentration at bubble/melt interfaces. The dimensionless parameter δ ($0 \leq \delta \leq 1$) decreases to 0 as melt and bubbles approach equilibrium. As shown in Fig. 3.5a, δ_{H_2O} is characterized by a monotonous decrease with increasing τ, and H_2O is close to equilibrium when $\tau > 10^3$ s, which agrees with experiments [8, 53, 82, 117]. Increasing λ or X_{CO_2} drives H_2O further away from equilibrium. In Fig. 3.5b CO_2 displays higher degrees of non-equilibrium than H_2O (δ_{CO_2} is one order greater than δ_{H_2O}), and behaves differently. A local maximum is found when $\tau \sim 100$ s. I will thereafter define τ_c as the critical τ that corresponding to the local maxima of δ_{CO_2} for a given set of X_{CO_2} and λ. The critical decompression time τ_c increases with the initial X_{CO_2} or a greater degree of non-linearity in the decompression path (λ). Fig. 3.5c is test plot that shows that the local maximum of δ_{CO_2} no longer exists if the diffusivity of H_2O and CO_2 were the same ($D_{H_2O} = D_{CO_2}$).

3.4 Discussion

I propose a parametric study of the effect of non-linear decompression paths on coupled CO_2–H_2O degassing during magma eruptions. My goals are two-fold. First, I aim to test whether the CO_2–H_2O content in the glass and other measurements such as the vesicularity of erupted samples can provide some constraints on the decompression history. Second, I

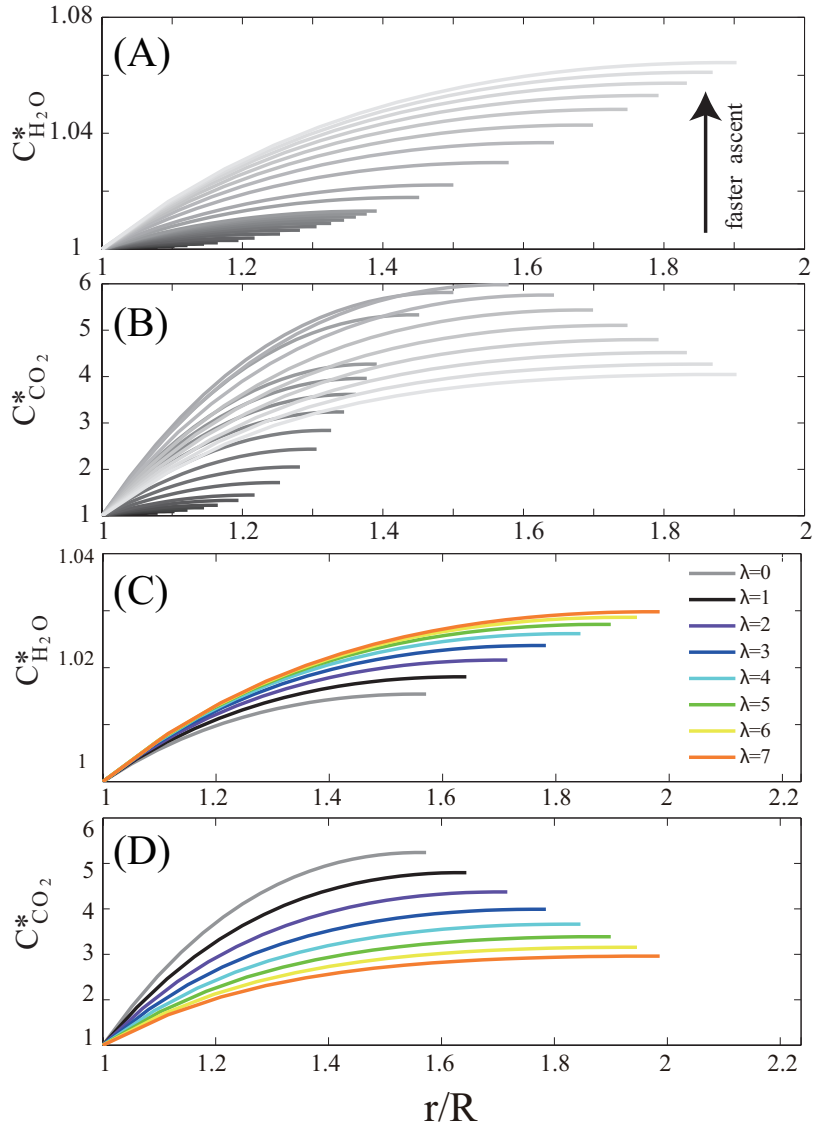

Figure 3.4: (a–b) H_2O and CO_2 diffusion profiles for linear eruption paths (different ascent time) and an initial bubble composition with 30 wt.% CO_2. The slower the ascent, the darker the color of the diffusion profile. The ascent rates in this plot range from ~ 0.1 m/s to ~ 100 m/s if assuming the density is constant. (c–d) H_2O and CO_2 diffusion profiles for a range of decompression paths (here the ascent time remains constant, ~ 4.2 mins in this plots, and λ is varied) with a bubble containing initially 40 wt.% CO_2. Warmer colors refer to more non-linear decompression paths (higher λ). All the profiles shown here are taken at vesicularity below 74%.

aim to quantify the error built in the assumption of constant magma decompression rate when estimating the average magma decompression rate from non-linear decompression paths.

1. When considering higher initial X_{CO_2} values, the solubility of H_2O in the melt decreases (see Eq. 3.6), and thus, the initial H_2O content in the melt decreases since my simulations start from equilibrium conditions between bubble and melt. Because of the lower dissolved H_2O content in the melt, (1) bubble experience less growth (i.e., smaller final vesicularity Φ_f), (2) the overpressure in bubbles is greater because the melt is more viscous (Fig. 3.3b), and (3) the diffusivity of H_2O and CO_2 is reduced as predicted by Eqs. 3.8 and 3.9. One of the consequences of lower diffusion coefficients is that higher concentrations of H_2O and CO_2 remain in the melt after the eruption (Figs. 3.3c and 3.3d. The other consequence is that the degree of disequilibrium of H_2O increases as the characteristic diffusion time scale increases.

2. When the non-linearity (λ) of a magma decompression path increases, the final bubble overpressure, $\langle H_2O \rangle$, $\langle CO_2 \rangle$, and δ_{H_2O}, increase as shown in Figs. 3.3–3.5. For a fixed total magma ascent time τ, λ affects the eruptions by modulating the duration and strength of the fast ascent period. From Fig. 3.1, I know that a path with higher non-linearity (larger λ) is characterized by an early stage at a lower decompression rate followed by a late stage of fast decompression. Slower decompression helps maintain near-equilibrium conditions, while faster decompression promotes the build-up of bubble overpressure, and increase the disequilibrium of H_2O between bubbles and the melt. Thus, for a fixed total magma ascent time τ, a path with higher λ leads to a lower final vesicularity, higher bubble overpressure, less volatile degassing, and higher δ_{H_2O}.

3. For shorter magma ascent time, δ_{CO_2} decreases as X_{H_2O} or λ increase, which contrasts with δ_{CO_2} associated with longer ascent time (see Fig. 3.5b). In order to constrain what factors control the existence of a maximum in δ_{CO_2} (λ, τ), I set some additional simulations where the transport kinetics (diffusion) of H_2O and CO_2 are assumed

identical (Fig. 3.5c). I find that the difference in transport kinetics (slow diffusion for CO_2) plays a fundamental role on the existence of a maximum for δ_{CO_2}. I argue that the combination of the delayed transport kinetics for CO_2 and the implicit coupling between H_2O and CO_2 that arises from the melt/bubble boundary conditions (solubilities, Eqs. 3.6 and 3.7) and H_2O–dependent D_{CO_2} are responsible for this feature.

3.4.1 Summary

My goal is to examine whether I can estimate the magma ascent time τ and the non-linearity of the decompression path λ from variables that I can measure in erupted samples. It turns out that Φ_f, over-pressure, $\langle H_2O \rangle$, $\langle CO_2 \rangle$, δ_{H_2O} share similar patterns as λ and τ vary. The similarity suggests these variables are not independent of each other. The contours of $\langle H_2O \rangle$ and δ_{H_2O} in λ-τ space are shown in Fig. 3.6 as examples. Isocontours for $\langle H_2O \rangle$ and δ_{H_2O} have a positive slope, which implies a trade-off between τ and λ. Therefore, measurements of water content in the melt do not provide a unique decompression history, but a family of possible decompression paths where an increase in assumed ascent time τ requires a more non-linear decompression history (higher λ). By following one $\langle H_2O \rangle$ contour line (e.g., the curved double arrows), I estimate $d\lambda/d\,(\log_{10}\tau)$ to be around $2 \sim 3$, so that $\Delta\tau \approx c(\ln 10)\tau\Delta\lambda$ where c is a constant ranging in $0.3 \sim 0.5$. The uncertainty on the non-linearity of magma decompression λ could lead to large errors in the estimated magma ascent time τ. For example, if one estimates the magma ascent time to be τ_0 by assuming a constant magma decompression rate ($\lambda = 0$), τ could be $5.8 \sim 9\tau_0$ if, in reality, $\lambda = 7$. Under specific circumstances, however, δ_{CO_2} can provide additional (independent) constraints on the decompression history.

I consider 3 scenarios based on measurements made on $\langle H_2O \rangle$, δ_{H_2O}, and δ_{CO_2} to discuss the possibility of using the concentration of volatiles dissolved in the melt to invert for λ and τ. Since the errors when measuring volatile content vary with different analytical methods, I set the relative errors for $\langle H_2O \rangle$, δ_{H_2O}, and δ_{CO_2} to be around 10% [86]. However, when the concentrations are very low and possibly near the detection limit, the relative error can

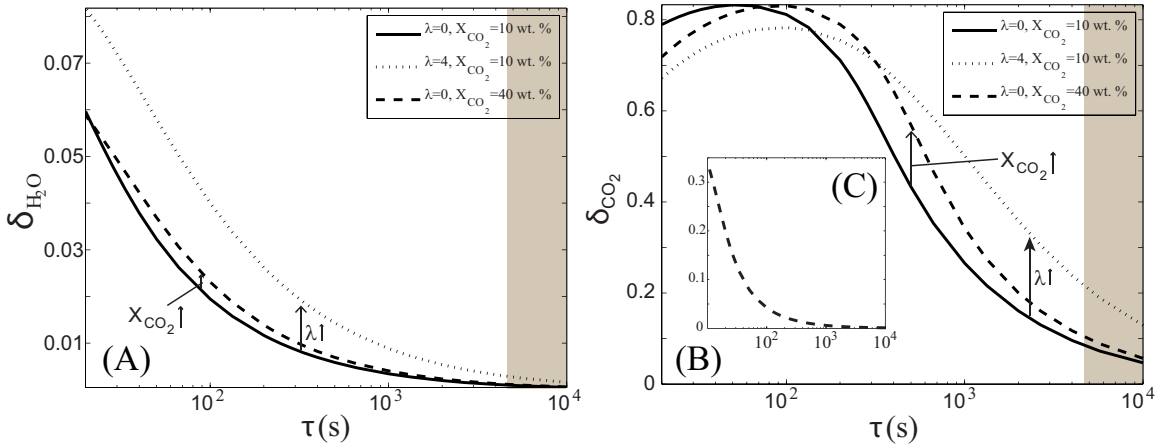

Figure 3.5: Variation of the disequilibrium of H_2O, δ_{H_2O} (A), and the disequilibrium of CO_2, δ_{CO_2} (B) between the bubble and melt after eruptions with respect to the total magma ascent time for $\lambda = 0, 4$ and $X_{CO_2} = 10$ wt.%, 40 wt.%. (C) δ_{CO_2} (y-axis) as a function of τ (x-axis) when $\lambda = 0$ and $X_{CO_2} = 40$ wt.% if the diffusivity of CO_2 is set equal to H_2O. Note the absence of a maximum in δ_{CO_2} for the latter case. The shaded regions are the same as in Fig. 3.3.

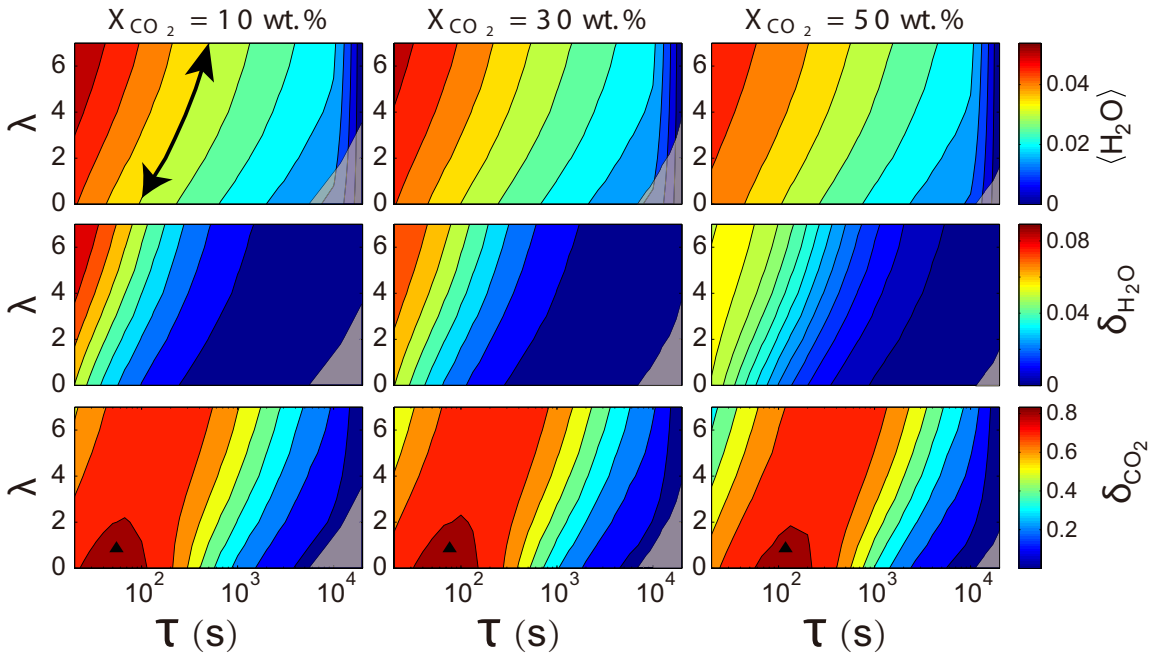

Figure 3.6: Average water concentration $\langle H_2O \rangle$, δ_{H_2O} and δ_{CO_2} after eruptions for various initial CO_2 content in bubbles, magma ascent time and degrees of non-linearity during decompression (λ). δ is defined as $\frac{C_{\max} - C_{\min}}{C_{\max}}$ for each diffusion profile. The regions where the final vesicularity is above 74 vol.% are shaded in grey (see bottom right corner of each panel).

creep up to 50%.

1. Scenario i

   Considering 2.2 wt.% $< \langle H_2O \rangle <$ 2.5 wt.%, 0.005 $< \delta_{H_2O} <$ 0.015, and 0.45 $< \delta_{CO_2} <$ 0.55, the solution space for λ-τ is bounded by the limits of the red dashed curves ($\langle H_2O \rangle$), the blue dashed curves (δ_{H_2O}), and the green dotted curves (δ_{CO_2}). When $X_{CO_2} = 10$ wt.% in Fig. 3.7a, the solution space covers $0.8 \leq \lambda \leq 7$ and 320 s $\leq \tau \leq$ 2000 s with $\Delta\lambda = 6.2$ and $\Delta\tau = 1680$ s. As X_{CO_2} increases to 30 wt.% (Fig. 3.7b) and 50 wt.% (Fig. 3.7c), the solutions differ in both τ and λ, and shift to a region centered around a higher value for τ. From the region i shown in all three subplots of Fig. 3.7, I can see clearly the trade-off between τ and λ and more specifically that a linear decompression assumption would bias τ towards rapid magma ascent.

2. Scenario ii

   Considering now 3 wt.% $< \langle H_2O \rangle <$ 3.5 wt.%, 0.025 $< \delta_{H_2O} <$ 0.035, and 0.65 $< \delta_{CO_2} <$ 0.75, the solution space is characterized by $\Delta\lambda = 5.5$ and $\Delta\tau = 205$ s ($1.5 < \lambda < 7$, 75 s $< \tau <$ 280 s) when $X_{CO_2} = 10$ wt.% and shift to a higher range of τ when X_{CO_2} increases. For $X_{CO_2} = 10$ wt.% and 30 wt.%, a solution with lower non-linearity (λ) of the decompression path, e.g., $\lambda < 2$, is unlikely as shown in Figs. 3.7a and 3.7b. However, when $X_{CO_2} = 50$ wt.%, a low-λ solution can exists (Fig. 3.7c).

3. Scenario iii

   When 3.5 wt.% $< \langle H_2O \rangle <$ 4.1 wt.%, 0.035 $< \delta_{H_2O} <$ 0.045, and 0.75 $< \delta_{CO_2} <$ 0.8, the solution space iii is confined to $0 < \lambda < 2$, 28 s $< \tau <$ 60 s with $\Delta\lambda = 2$ and $\Delta\tau = 32$ s for $X_{CO_2} = 10$ wt.% (Fig. 3.7a). For $X_{CO_2} = 30$ wt.% (Fig. 3.7b), the space of possible solutions shifts to longer total ascent times. I find no admissible solutions for $X_{CO_2} = 50$ wt.% (Fig. 3.7c). For these specific conditions, the solutions space is tightly-confined and inversions would yield relatively small errors $\Delta\lambda$, $\Delta\tau$.

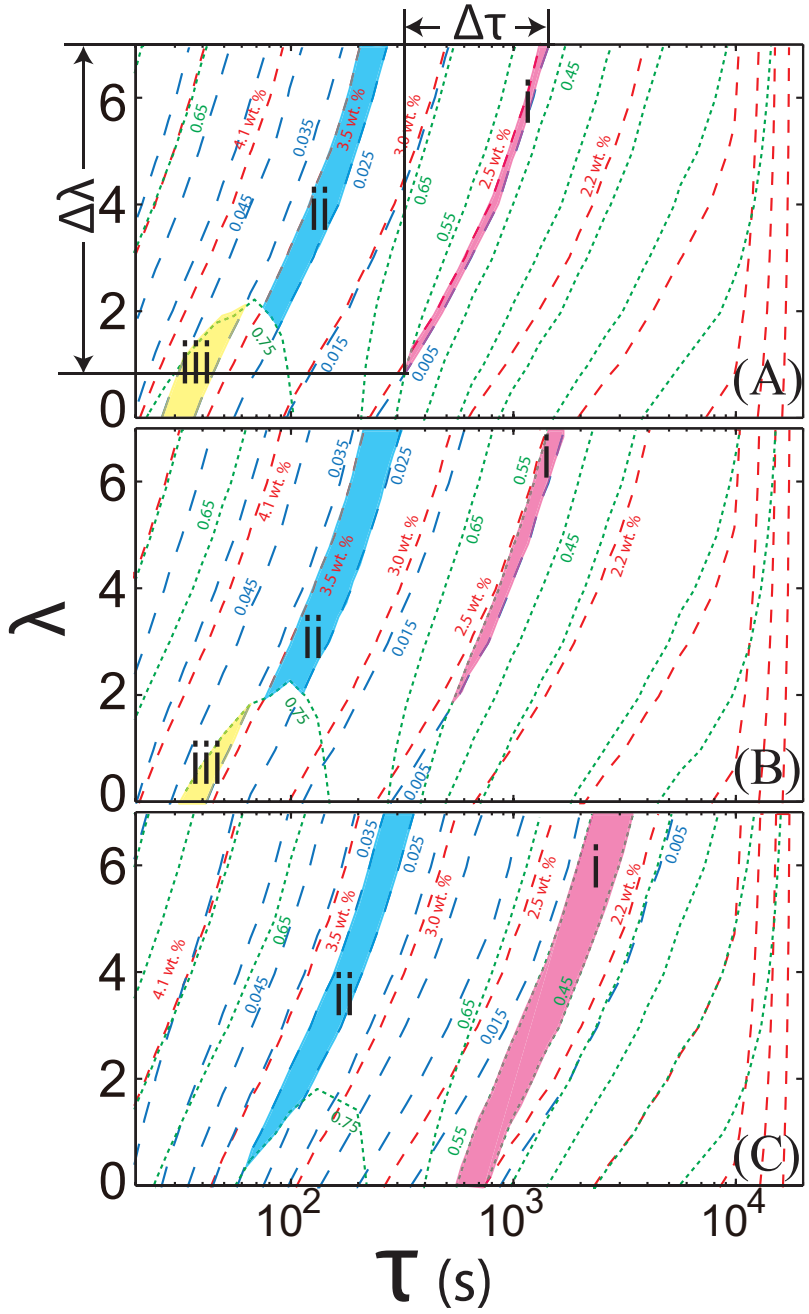

Figure 3.7: Solution space for λ and τ from the average water concentration $\langle H_2O \rangle$ (red and dashed curves), δ_{H_2O} (blue and medium dashed curves), and δ_{CO_2} (green and dotted curves). When the initial CO_2 content $X_{CO_2} = 10$ wt.% (a), 30 wt.% (b), 50 wt.% (c), 3 scenarios are discussed in the main text as examples to invert for (λ, τ). **Scenario (i)** (2.2 wt.% $< \langle H_2O \rangle <$ 2.5 wt.%, $0.005 < \delta_{H_2O} < 0.015$, and $0.45 < \delta_{CO_2} < 0.55$), **Scenario (ii)** (3 wt.% $< \langle H_2O \rangle <$ 3.5 wt.%, $0.025 < \delta_{H_2O} < 0.035$, and $0.65 < \delta_{CO_2} < 0.75$), and finally **Scenario (iii)** (3.5 wt.% $< \langle H_2O \rangle <$ 4.1 wt.%, $0.035 < \delta_{H_2O} < 0.045$, and $0.75 < \delta_{CO_2} < 0.8$).

3.4.2 Applications

As illustrated by the 3 scenarios in Sec. 3.4.1, I can confine the solutions in a relatively small region compared to the full space of λ-τ with (1) the measurement of the average $\langle H_2O \rangle$, δ_{H_2O}, and δ_{CO_2} in the glass of the samples and (2) the estimate of a plausible range for the initial X_{CO_2} of the magma. My approach retrieves a family of solutions with a trade-off between λ and τ.

Furthermore, assuming a constant decompression rate from volatile kinetics comes at the cost of severely underestimating the true average decompression rate and the total ascent time. To narrow down the choice of possible λ and τ, one should look for other constraints independent of $\langle H_2O \rangle$, δ_{H_2O}, and δ_{CO_2}. One candidate would be to consider other volatile species, such as SO_2. SO_2 is the third most abundant volatile species in magmas, and has an even lower diffusion coefficient than CO_2. In that regard, and considering that SO_2 and H_2O are coupled through the partitioning of S between the bubbles and the melt, a local maximum in δ_{SO_2} could exist and would most likely be shifted to greater τ compared to δ_{CO_2}.

An interesting byproduct of my study is to use the combination of $\langle H_2O \rangle$, δ_{H_2O}, and δ_{CO_2} to constrain the initial X_{CO_2} present in the magma. My method for inverting for λ and τ can potentially be applied to estimate the initial magma volatile content, e.g., X_{CO_2}. For a set of measured $\langle H_2O \rangle$, δ_{H_2O}, and δ_{CO_2} , I could search for different λ-τ solutions considering various X_{CO_2}. For example, panels (a–c) in Fig. 3.7 show the admissible solutions for λ–τ constrained by $\langle H_2O \rangle$, δ_{H_2O}, and δ_{CO_2} for 3 different initial X_{CO_2}. I find that scenario (iii) does not admit a solution for high X_{CO_2} (50 wt.%). Although I am not yet in measure to constrain the initial X_{CO_2} of the magma by measuring $\langle H_2O \rangle$, δ_{H_2O}, and δ_{CO_2}, I can restrict, in some cases, the range of possible X_{CO_2} of the predegassed magma. This perspective is encouraging because it suggest that I may be able to constrain the starting X_{CO_2} composition of the magma as well as λ and τ if I find an additional constrain on decompression that is independent from $\langle H_2O \rangle$, δ_{H_2O}, and δ_{CO_2}.

3.5 Conclusions

In this work, I use a bubble growth model with H_2O–CO_2 coupled kinetics to investigate how the initial volatile composition, the magma ascent time, and the non-linearity of the decompression path influence volatile kinetics during rhyolitic eruptions. The main findings are: (1) the disequilibrium states of H_2O and CO_2 between bubbles and the melt are different when magmas ascend following different non-linear decompression paths; (2) the disequilibrium of CO_2 between bubbles and the melt does not behave monotonically with magma ascent time and the non-linearity of the decompression rate; (3) the solution space of λ-τ exhibits a trade-off between the magma ascent time τ and the linearity of the magma decompression path; (4) the methods relying on volatile diffusion and assuming a constant decompression rate over-estimate the effective average magma decompression rate.

CHAPTER IV

A NEW BUBBLE DYNAMICS MODEL TO STUDY BUBBLE GROWTH, DEFORMATION AND COALESCENCE

In Chaps. 2 and 3, the models for simulating volatile degassing in silicic volcanic eruptions include volatile kinetics and assume an idealized bubble geometry as well as no interactions between bubbles. Although these models can yield predictions for volatile degassing during volcanic eruptions, they have many limitations: (1) bubbles are monodispersed and distributed as a periodic array, (2) there are no confining boundaries that prevents/limits growth, (3) bubbles remain spherical at all times and (4) bubbles do not interact hydrodynamically (no diffusion coarsening, no coalescence). These limitations can be significant when considering magmas with high vesicularity, or when attempting to use bubble deformation as a strain tracer in the ascending magma. Since bubble-bubble interactions and bubble deformation by shear often become significant as the magma approaches a possible fragmentation level, it is important to go beyond these common assumptions and develop a new bubble dynamics model.

In this chapter, a new bubble dynamics model is proposed and accounts for hydrodynamical interactions among bubbles, e.g., bubble deformation and coalescence. The model is then calibrated with laboratory experiment of a bubble rising to a free surface and validated for bubble growth, Ostwald ripening and bubble deformation in simple shear conditions. This chapter represents the work that I co-authored in Ref. [76]. My contribution to this work was to participate in the development of the model and conduct the simulations and analyses of the bubble shearing calculations. A notation list for this chapter is shown in Appendix D.

4.1 Introduction

Exsolved volatiles provide the driving force for explosive volcanic eruptions. While the magma is ascending to the surface, the melt becomes super-saturated with volatiles driving

bubble nucleation and growth. The increasing vesicularity of the magma during decompression affects its buoyancy (provides an acceleration) and deeply affects the physical properties of the magma [63]. The processes that control the nucleation and growth of gas bubbles (water and CO_2, mostly) are complex and highly non-linear.

Bubbles gain mass by diffusion during decompression as the solubility of gas in the silicate melt is suppressed and, simultaneously, they grow by mechanical expansion due to the compressibility of the gas phase. On the other hand, the viscosity of the surrounding melt poses a resistance to bubble growth. The interplay between diffusion of volatiles, expansion and viscous resistance during the growth of a single bubble or a periodic suspension of monodisperse bubbles in an infinite silicate melt as been studied theoretically and numerically with various levels of sophistication [50, 97, 99, 111, 152, 154, 182, 199, 217]. These studies were able to identify different growth regimes: viscosity- and diffusion-controlled, and also highlight the important effect of spatially variable viscosity and water diffusivity in these processes. Even though some of the bubble dynamics models cited above differ in terms of approaches, they share some common assumptions. The first assumption made is that bubble have little to no hydrodynamic interactions between each other and also with rigid/partially rigid confining boundaries. In other words, bubbles remain spherical at all times, deformation between bubbles that are coupled hydrodynamically or of a bubble that interacts with a boundary (conduit wall for example) are not taken into account. Even if the studies of Refs. [51, 217] consider the effect of coalescence into their bubble population dynamics model, it is introduced as a simple parameterization and does not account for the actual mechanics of the process.

The inability of previous bubble growth models to account for bubble deformation, coalescence and (3) bubble deformation under different flow environments (uniaxial decompression, shear) hampers their applicability to magmas with low vesicularities. However, the effect of bubbles on the evolution of the ascending magma increases with its vesicularity. Ultimately, prior to the onset of fragmentation, it is the rheological state and pressure distribution in a high vesicularity suspension (commonly greater than 50%) that controls the eruption dynamics [61, 154, 182, 223]. In this chapter, I describe a new model that is

designed to investigate the physical evolution of bubble suspensions in magmas across a wide range of vesicularities (from a few to $\gg 50\%$) subjected to different decompression and shear flow conditions.

In this contribution, I present the physical and numerical bubble model, provide validations of the model and explore the ability of the model to solve problems where bubble-bubble or bubble-structure interactions become important. My model differs significantly from other published bubble growth models in that it is based on different numerical approach that allows one to deal with deformed bubbles and resolve the hydrodynamical interactions between bubbles in the suspension. In Sec. 4.2, I review in greater details the existing bubble dynamics models in physical volcanology. I also discuss the advantages and limitations of my model in the light of the existing models. The physical and numerical model is presented in Sec. 4.3. Model validations for the growth of bubbles by expansion and diffusion are presented in Sec. 4.4. It is followed by tests of the model's ability to go beyond the limitations of existing bubble growth models. The first set of calculations consists of the ascent of a single bubble (no mass change) to a free surface and the subsequent film drainage that results in the bubble bursting at the surface. These calculations serve to calibrate a free parameter in my model, the disjoining pressure, that controls the efficiency of the drainage process, and by extension of coalescence. I use a set of experiments with an identical design to calibrate the disjoining pressure as function of the bubble Bond's number (ratio of buoyancy to surface tension stresses). The objective of the next series of calculations is to test the model accuracy with scenarios of bubble-bubble or bubble-structure interactions. I focus first on Ostwald ripening, where the thermodynamical coupling between two neighbor bubbles of different sizes leads the growth of the larger bubble at the expense of the smaller one in response to chemical potential gradients between bubbles of different sizes. Lastly, I test the models ability to resolve accurately the viscous and capillary coupling between bubbles and the ambient melt in simple shear flow conditions. When inertia can be neglected, it is known that single bubbles are expected to reach a known steady shape (deformed when viscous stresses are important) and a known final orientation that depends on the balance between shear and capillary stresses. Finally, I use my model

to study the evolution of the distribution of deformation and orientation of a suspension of bubbles and contrast it to single bubble calculations. This allows one to quantify the effect of bubble-bubble hydrodynamic interactions on a sheared suspension.

In subsequent studies, I plan on focussing on (1) the resultant drag and lift forces between a suspension and the melt in shear flow conditions, (2) the dependence of the coalescence rate in a suspension as function of shear at constant and time-dependent (growth) vesicularity and (3) introduce water-dependent viscosity and diffusivity. The ultimate objective behind the development of these numerical investigation of bubble dynamics is to provide conduit flow models with a parameterization of bubble-melt interactions that covers a wide range of dynamical conditions and vesicularity.

4.2 Bubble dynamics models

The understanding of bubble growth in viscous silicate melts has made significant progress over the last three decades, thanks to a combined experimental [52,93,95,111,117,126,132–134], theoretical and numerical efforts [17,97,99,152,154,182].

In this section, I present a brief overview of the field of bubble dynamics models in physical volcanology. Since the seminal work of Ref. [203], it has been recognized that exsolved volatiles (bubbles) can play a significant role on the behavior of magmas during volcanic eruptions. A few decades later, Sparks [182] developed a model of a single bubble growing in an infinite melt, where the growth of the bubble is caused by expansion and mass transfer (diffusion) during decompression and is hampered by the viscosity of the melt. The transport of dissolved volatiles to the bubble's interface was not explicitly solved for, but the growth rate due to diffusion was parameterized according to a parabolic growth law.

In the late 1980's and early 1990's two different categories of multiple bubble growth models were simulaneously developed. In the first family of models, diffusion of volatiles to the bubbles is parameterized (mean-field approach), but polydispersed bubble size distribution are allowed [50,99,198,199,217]. These models assume that the bubbles remain spherical (no deformation) and, in the exception of Ref. [51], coalescence is not taken into account. An advantage of these models, over the second family of models discussed just

below, is that they allow to include several nucleation event, although the competition for dissolved water during growth is not explicitly taken into account.

The second family of models is based on the work of Ref. [152], where the multiphase magma is represented as a monodisperse periodic array of spherical bubbles surrounded by a viscous melt shell [17,97,111,154]. This idealization was made to solve for the evolution of a single bubble-melt shell system with a radial symmetry. The model solves for the diffusive transport of dissolved volatiles to bubbles explicitly, as well as for the existence of radial gradients in water concentration and its effects on the melt viscosity and water diffusivity [17, 97, 154]. These models draw an accurate representation of the coupled momentum balance and diffusive transport of volatiles at the cost of an ideal geometry and a suspension that remains monodisperse at all time.

The two types of approaches have lead to important results about the different regimes of bubble growth [97,152], the effect of viscosity and diffusivity radial heterogeneities on bubble growth [17,97,154], the effect of supersaturation on the nucleation of new bubbles and how it translates into changes in bubble number density and size distributions [198, 199, 217]. Nevertheless, all these models are limited to low versicularity by several assumptions. The first assumption concerns the limited hydrodynamic coupling between the bubbles and between the melt and bubbles. Bubbles are not allowed to deform and remain spherical. The behavior of a bubble of radius r during shear deformation can be constrained by the capillary number

$$Ca = \frac{\rho \nu \dot{\epsilon} r}{\sigma}, \tag{4.1}$$

where σ is the surface tension, ρ is the melt density, $\dot{\epsilon}$ is the shear-rate and ν the dynamic viscosity of the melt. At high capillary numbers ($Ca > 0.1$) bubbles are expected to accomodate a large portion of the shear and the spherical assumption becomes invalid [115, 116]. Although shear deformation of bubbles should be expected to play a significant role mostly in melts with high viscosity or for large bubbles, the hydrodynamic coupling between bubble and melt and between multiple bubbles is also expected to play a significant role in magmas with high vesicularity. The second argument that restricts the standard bubble growth models to low vesicularity is that they do not account explicitly for the

competition for dissolved volatiles during the growth of bubbles of different sizes, or with different separation distances. Bubbles with different spacing, different size and different internal pressures will be responsible for variable gradients in dissolved water content in the melt, this effect may lead to some implicit non-linear interactions among neighbor bubbles. The dynamics of coalescence has been avoided, at least explicitly (besides the Smoluchowsky approach of Ref. [51]), but it has been shown that, at vesicularity of about 40 percent, expansion and growth can lead to significant coalescence and that this effect becomes even more important at lower vesicularity in a suspension subjected to shear [21, 133, 134]. Another implicit assumption common to all previous models is that there is no respective motion between the center of mass of a bubble and the ambient melt, this is a good approximation for small bubbles and melts with high viscosity, but it is expected to break down in the other cases or when connected pathways start to form between coalesced bubbles and gas-melt segregation occurs.

In this study, I develop a new bubble dynamics model to attempt to remediate to some of the common limitations listed above. The aim of this model is to keep an explicit description of the mass transport of dissolved water by diffusion in the melt, free ourselves from the radial symmetry and allow bubbles to interact hydrodynamically with the melt and other bubbles. In other words, the new model should provide the ability to solve for bubble deformation and coalescence. I also want to be able to consider enough bubbles at the same time (orders of hundreds at this stage) and distribute them randomly in space so as to follow the evolution of the bubble size distribution (variable bubble growth rate in a given suspension) and coalescence rate during decompression. Finally, I want the new model to allow one to investigate the effect of an imposed shear-rate on the rheological behavior of the suspension and on the bubbles coalescence rate, this requires a model that can solve for a finite and spatially variable motion between each bubble center of mass on the melt surrounding bubbles. The model I present below allows one to study these processes, but the aim of this chapter is limited to a few case studies (see Introduction). I plan on considering more sophisticated problems in future studies. My goal with this model is to address some of the fundamental processes associated with bubble interactions, such

as those expected at vesicularities $>$ 10–20%, and better understand the behavior of the multiphase mixture prior to fragmentation (if any) or closer to vent conditions.

Before describing the new model in details, I step back and list some of the present (should be overcome in future studies) and absolute limitations of my model.

1. The model is discretized in space on a homogeneous grid, it is therefore not accurate in terms of water concentration profile at the early stage of degassing. The model of Proussevitch et al. [152] is expected to yield more accurate results at low vesicularity. However, at later stages, when the vesicularity is greater (more advanced diffusion profiles) the model is expected to perform well. Although the spatial resolution is an issue for the accuracy of the diffusion model at early times (steep gradients), I want to emphasize that film drainage between bubbles and coalescence, which are solved by a Volume-of-Fluid method (see below), use a mass balance description that has a subgrid spatial resolution (see below).

2. The model is, as of now, limited to 2-D calculations. An extension to 3-D is not trivial (calculation time) but nothing should prevent it in the near future. Although the existing models discussed above are intrinsically 3-D, they assume a perfect radial symmetry (which is unlikely to be exact) and therefore reduce the physics to 1 dimension.

3. In this study, water-dependent melt viscosity and diffusivity were not taken into account. As discussed in the next section, this does not betray an intrinsic limitation of my model and these dependence will be added in a subsequent study.

4.3 Numerical method

The bubble model I propose is based on the lattice Boltzmann method for free surface flows [92]. The lattice Boltzmann method (LBM) has emerged as an efficient alternative to traditional computational fluid dynamics (CFD) solvers and was developed as an extension to cellular automata [48, 71]. The LBM solves for the evolution of particle distribution functions according to simple rules and follows a discretized form of Boltzmann's kinetic

equation. The model I use for bubble dynamics is an extension of the model proposed by Körner [92] where the fluid inside bubbles is assumed inviscid and interfaces between the two fluids are treated as a free surface boundary condition. In this section, I describe the model and introduce some of the extensions that were required to adapt it to decompression and shear flow conditions.

4.3.1 The lattice Boltzmann model for free surfaces

The lattice Boltzmann free surface method on which my bubble model is based has been used successfully by different authors to measure dynamic contact angles, study metal foaming processes and free surface flows [6, 92]. Within the LBM, Boltzman's equation is commonly discretized in physical and velocity spaces so that particle distribution functions, at a given lattice site, can stream along a finite number of directions (lattice velocity vectors) and reach a neighbor site at the next time step. In general, in 2-D (my model is limited to 2-D so far, but the model would remain similar in 3-D), a topology with one rest velocity $\mathbf{e}_0 = (v_{x,0} = 0, v_{y,0} = 0)$ and 8 finite velocity vectors connecting the site to its nearest neighbors is used. This 9-velocity lattice topology is usually referred to as the D_2Q_9 lattice (see Fig. 4.1a) with velocities $\mathbf{e}_i$

$$\mathbf{e}_i = \begin{cases} (0,0) & \text{if } i = 0 \\ \left(\cos\left(\frac{(i-1)\pi}{2}\right), \sin\left(\frac{(i-1)\pi}{2}\right)\right) & i = 1, \ldots 4 \\ \left(\cos\left(\frac{(2i-1)\pi}{4}\right), \sin\left(\frac{(2i-1)\pi}{4}\right)\right) & i = 5, \ldots 8. \end{cases} \tag{4.2}$$

The evolution equation for the particle distribution functions f_i (where i stands for the discrete velocity vector along which the particles are moving) uses a simplified (linearized) collision operator, often referred to as the BGK or single relaxation time operator [156]. The update of the distribution between two consecutive timesteps (t and $t+1$) is given by

$$f_i(\mathbf{x} + \mathbf{e}_i, t+1) = f_i(\mathbf{x}, t) + \frac{1}{\tau_F}[f_i^{\text{eq}}(\mathbf{x}, t) - f_i(\mathbf{x}, t)] + F_i, \tag{4.3}$$

where $\mathbf{x}$ are the spatial coordinates on the lattice, t is time, f_i^{eq} is the equilibrium distribution (defined below) and F_i represents a body force acting on the distribution f_i. The

relaxation time τ_F is explicitly related to the kinematic viscosity of the fluid

$$\nu = c_s^2 \left(\tau_F - \frac{1}{2} \right), \tag{4.4}$$

where c_s^2 is a constant of the lattice (1/3 on the D_2Q_9). The local fluid density and momentum (and hence velocity) can be retrieved as moments of the particle distribution functions

$$\rho(\mathbf{x}, t) = \sum_{i=0}^{8} f_i \quad \text{and} \quad \rho(\mathbf{x}, t)\mathbf{u}(\mathbf{x}, t) = \sum_{i=0}^{8} \mathbf{e}_i f_i. \tag{4.5}$$

The equilibrium distribution is a quadratic function of the local fluid velocity and depends linearly on the density

$$f_i^{\text{eq}}(\mathbf{x}, t) = w_i \rho(\mathbf{x}, t) \left[1 + \frac{\mathbf{u} \cdot \mathbf{e}_i}{c_s^2} + \frac{1}{2} \frac{(\mathbf{u} \cdot \mathbf{e}_i)^2}{c_s^4} - \frac{1}{2} \frac{\mathbf{u} \cdot \mathbf{u}}{c_s^2} \right], \tag{4.6}$$

where w_i are the lattice weights, $w_0 = 4/9$, $w_{1-4} = 1/9$ and $w_{5-8} = 1/36$. This generic lattice Boltzmann model was shown to recover Navier-Stokes and the continuity equations with second order accuracy in space and first order in time [71, 156]. For simplicity, I subdivide Eq. 4.3 into two steps: the collision step

$$f_i^{\text{out}}(\mathbf{x}, t) = f_i(\mathbf{x}, t) + \frac{1}{\tau_F} [f_i^{\text{eq}}(\mathbf{x}, t) - f_i(\mathbf{x}, t)] + F_i, \tag{4.7}$$

and the streaming step

$$f_i^{\text{in}}(\mathbf{x} + \mathbf{e}_i, t + 1) = f_i^{\text{out}}(\mathbf{x}, t). \tag{4.8}$$

The free surface model developed by Körner and co-workers [92] uses an approach similar to the Volume-of-Fluid method, where a continuous scalar occupancy field m allows to track the position and evolution of the interface between the two fluids (here bubble and silicate melt). The lattice is divided among three cell-types, gas, melt and finally interface cells (see Fig. 4.1b). With this approach, there is no direct contact between gas and melt cells. The type of each cell is updated dynamically according to the local evolution of the scalar quantity m. The field variable m represents the fluid mass content of the cell and is given by

$$m(\mathbf{x}, t) = \begin{cases} 0 & \text{if } \mathbf{x} \in \text{Gas cell} \\ \rho(\mathbf{x}, t) & \text{if } \mathbf{x} \in \text{Melt cell} \\ \rho(\mathbf{x}, t)\epsilon(\mathbf{x}, t) & \text{if } \mathbf{x} \in \text{Interface cell.} \end{cases} \tag{4.9}$$

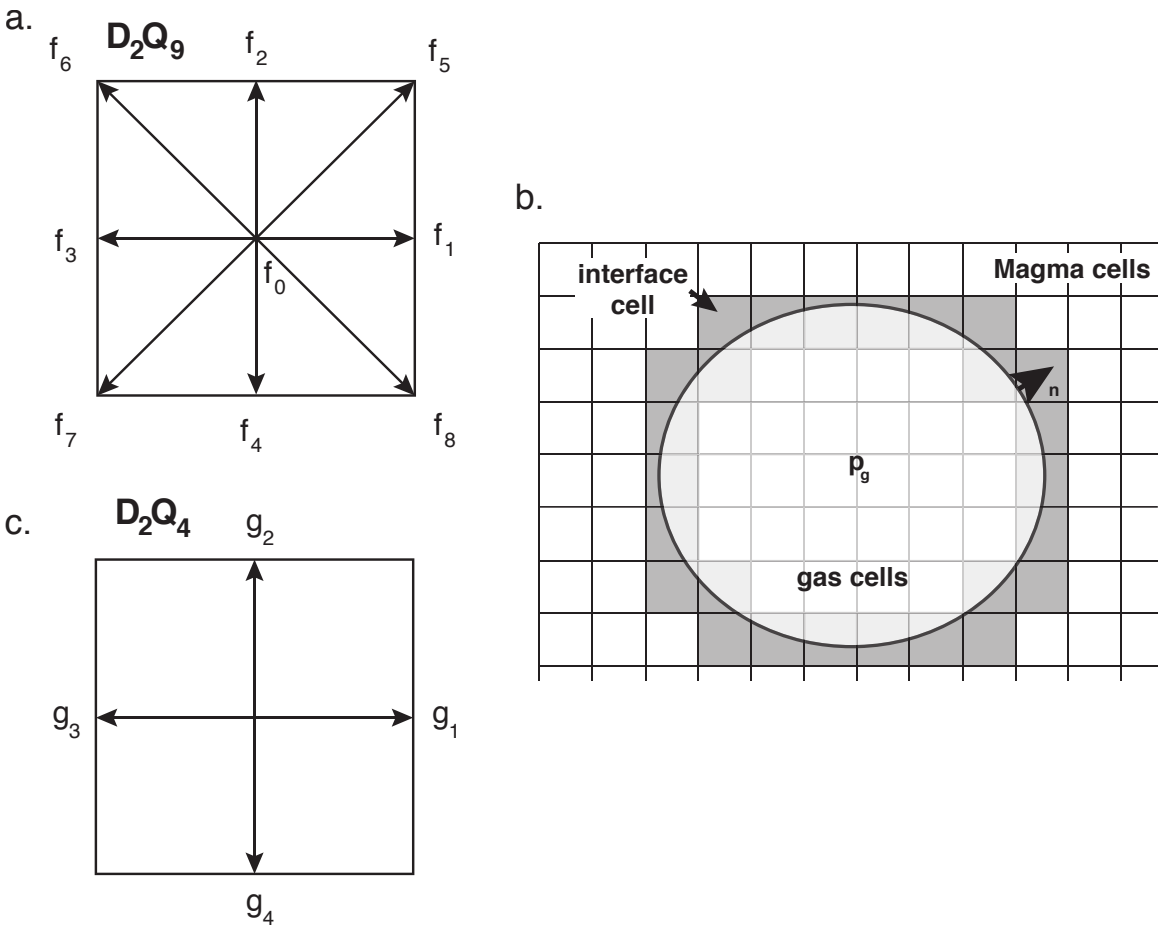

Figure 4.1: Discretization of the particle distribution functions in velocity space. The two choices of lattice used (a) for the advection-diffusion equation for the dissolved volatile concentration (D_2Q_4) and (c) for the viscous fluid flow around bubbles (D_2Q_9). (b) Illustration of the Volume of Fluid approach used for the lattice Boltzmann free surface model. The domain is divided among three cell types, bubble cells where no dynamics is computed, melt/fluid cells where Navier-Stokes and the advection-diffusion equations are solved, and interface cells that separate the other two types and act as boundary conditions between bubbles and ambient melt.

where ϵ is the volume fraction of melt at site $\mathbf{x}$ and time t (between 0 and 1). An evolution equation for the distribution of each cell-type is required because gas bubbles (hereafter referred to as bubbles) and the melt can move with respect to the lattice, while, simultaneously, bubbles can expand (mechanical work) and grow during decompression. The evolution equation for m follows the procedure described in Ref. [92] and consists of tracking the mass exchange between neighbor site of each cell-type

$$\Delta m_i(\mathbf{x},t) = \begin{cases} 0 & \text{if } \mathbf{x} \in \text{Gas cell} \\ \Delta f_i^{\text{out}} \equiv f_{\bar{i}}^{\text{out}}(\mathbf{x}+\mathbf{e}_i,t) - f_i^{\text{out}}(\mathbf{x},t) & \text{if } \mathbf{x} \in \text{Melt cell} \\ \frac{1}{2}(\epsilon(\mathbf{x},t)+\epsilon(\mathbf{x}+\mathbf{e}_i,t))\Delta f_i^{\text{out}} & \text{if } \mathbf{x} \in \text{Interface cell.} \end{cases} \tag{4.10}$$

where $\mathbf{e}_{\bar{i}} = -\mathbf{e}_i$. Ref. [92] showed that this scheme conserves mass locally and that m can now be updated at each site using

$$m(\mathbf{x},t+1) = m(\mathbf{x},t) + \sum_{i=0}^{8} \Delta m_i(\mathbf{x},t). \tag{4.11}$$

Obviously, the mass content of each cell must stay bounded $0 < m(\mathbf{x},t) < \rho(\mathbf{x},t)$. To enforce this bounds, I impose the following set of rules: if $m \geq \rho$, the cell is converted to a melt cell, if $m < 0$, then it is converted to a gas (bubble) cell. Similarly, new interface cells are created when a former melt cell evolves so that $m < \rho$ or a gas cell mass content becomes greater than 0 ($m > 0$). A more complete description of the mass redistribution algorithm can be found in Ref. [92].

Because the viscosity ratio between the melt and the gas in the bubbles is generally greater than 10^7, I assume that the fluid inside bubbles is inviscid. That allows one to treat bubbles as boundary conditions similar to free surfaces, i.e., no tangential stress, but existing normal (pressure) drop at the interface between the two fluids. If the gas pressure is known, I can apply a pressure boundary condition on the melt. I assume that the gas in the bubble is ideal

$$p_g = \frac{nRT}{V}, \tag{4.12}$$

where n is the number of moles of gas molecules in a given bubble, V its volume, T the ambient temperature (here assumed constant) and R the ideal gas constant. At any given interface cells, some elements f_i of the particle distribution functions are missing because

they carry information from a gas-cell (outside of the domain where the f_i's are defined) to the interface-cell. These missing distributions are reconstructed to impose the correct boundary condition on the melt, using informations from the gas pressure in the bubble and the curvature of the interface at the interface site. For more details about this procedure, the reader is referred to Ref. [92]. The effect of the surface tension σ between the two fluids can be added easily to the gas-interface boundary conditions

$$p_g(\mathbf{x},t) = \frac{n(t)RT}{V(t)} - 2\kappa(\mathbf{x},t)\sigma, \tag{4.13}$$

where $n(t)$ and $V(t)$ are the number of moles of gas molecules (here I focus on water) and the volume of the bubble respectively, and $\kappa(\mathbf{x},t)$ is the local curvature of the interface. When considering multiple bubbles interacting with each other, or the interaction of a bubble with a free surface, an additional term is included in the pressure boundary condition: the disjoining pressure Π

$$p_g(\mathbf{x},t) = \frac{n(t)RT}{V(t)} - 2\kappa(\mathbf{x},t)\sigma - \Pi. \tag{4.14}$$

The disjoining pressure is defined as the variation of Gibbs free energy with distance associated with the interaction of two melt-gas interfaces associated with different objects (e.g., two different bubbles or a bubble and a free surface)

$$\Pi = -\frac{1}{A}\left(\frac{\partial G}{\partial x}\right), \tag{4.15}$$

here A is the surface area of the interacting surfaces and G is the Gibbs free energy. The disjoining pressure term has a fundamental impact on controlling the coalescence rate between bubbles and therefore the stability of foams. For simplicity, the disjoining pressure can be taken as a linearly decreasing function of the distance between the two interacting objects with a finite range d_{range}

$$\Pi(d_{\text{int}}) = \begin{cases} 0 & \text{if } d_{\text{int}} \geq d_{\text{range}} \\ c_\Pi |d_{\text{int}} - d_{\text{range}}| & \text{if } d_{\text{int}} < d_{\text{range}}. \end{cases} \tag{4.16}$$

The disjoining pressure is therefore set by two constants: its amplitude c_Π and range d_{range}, as well as the distance between the two interacting interfaces neighbor objects d_{int}. I discuss how the disjoining pressure model is calibrated from experiments in section Sec. 4.4.

A more detailed explanation of the method can be found in Ref. [92]. I note however, that keeping track of the mass content in each interface nodes allows one to accurately model the coalescence of bubbles (if the disjoining pressure term is correctly calibrated) which occurs when the fluid content of the interface node separating to adjacent bubbles has fully drained out of the interface. Finally, for all calculations involving solid surfaces, the contact angle between the interface separating the two fluid phases and the solid boundaries is such that the gas phase is non-wetting.

4.3.2 Decompression scheme

During volcanic eruptions, decompression exerts a major control on the physical state of the magma. The change in pressure influences the density of the gas phase (through my assumed ideal gas law) and also the solubility of the volatile species dissolved in the melt (here again I limit the study to water). A large number of experiments were designed to study the growth regime of suspension under different decompression conditions, from a static decompression (instantaneous pressure drop) to constant decompression rates [21,52,55,94]. While many of these studies focused on the transition from equilibrium to non-equilibrium bubble growth as function of imposed decompression rates and melt viscosity [52, 55, 126], other studies investigated the effect of bubble-bubble interactions on the growth rate of a suspension [94], the vesicularity at the onset of coalescence [21, 93] and the effect of shear on coalescence and the formation of outgassing permeable pathways [132].

During decompression, two processes lead to bubble growth: (1) mechanical expansion (no mass exchange between the melt and the suspension) and (2) degassing by diffusion from a supersaturated melt to adjacent bubbles. In this section, I focus first on mechanical expansion. In order to account for decompression, I modified the scheme presented above to allow for the pressure in the gas phase to evolve in response to the change of ambient pressure. For simplicity, in the light of my model, I assume a pressure reference frame where the pressure in the ambient melt p_{amb} (which is supposed to follow closely the decompression pressure path) is constant over a given run. In that reference frame, the pressure in bubbles is expected to increase if the bubble overpressure develops, i.e., if the decompression rate is

fast enough for the growth of the bubble to be impeded by the viscous melt. Assuming a decompression rate in the melt $(dp/dt)_{\text{dec}}$ (< 0 for decompression), the pressure evolution in bubbles does not follow Eq. 4.12, but rather

$$\frac{dp_g}{dt} = RT\left[\frac{1}{V}\frac{dn}{dt} - \frac{n}{V^2}\frac{dV}{dt}\right] - \left(\frac{dp}{dt}\right)_{\text{dec}}, \tag{4.17}$$

where the number of moles of gas n is allowed to evolve with time (in the case of exsolution), the volume V can change in response to mechanical expansion and because the number of moles increases by diffusion if the solubility of dissolved water decreases during decompression (see next subsection). The effect of surface tension and the disjoining pressure can be added into the boundary condition similarly to Eq. 4.14. In the limit where diffusion of dissolved water is neglected, the pressure evolution reduces to

$$\frac{dp_g}{dt} = -RT\frac{n}{V^2}\frac{dV}{dt} - \left(\frac{dp}{dt}\right)_{\text{dec}}, \tag{4.18}$$

where the pressure equilibrium between the melt and the bubbles (no residual overpressure) is reached when the volume change of bubbles accomodates all the decompression of the modeled magma parcel, which occurs only when the growth of bubbles is not viscously limited.

The decompression model presented here does not restrict one from studying the effect of non-uniform decompression rates (although not the focus of this chapter). Nevertheless, Eq. 4.17 can limit the choice of timesteps (small time steps) for large decompression rates, as the pressure in the bubble must remain > 0. The scheme was found to be stable over the whole range of calculations presented in this study.

4.3.3 Volatile diffusion and bubble growth

In order to allow for the degassing of dissolved volatiles, the model needs to account for diffusion of dissolved volatiles in the melt. I use a similar approach to Ref. [92], where a second set of distribution functions g_j is used to model an advection-diffusion equation with imposed concentration boundary conditions at the bubble-melt interfaces. Because the advection-diffusion equation requires less symmetry than the momentum conservation in the lattice Boltzmann method, I use a different lattice topology with four velocities

(D_2Q_4, see Fig. 4.1c). The lattice nodes for g_j coincide with the D_2Q_9 lattice used for the flow calculations. A similar discretized Boltzmann equation can be solved for the dissolved volatile concentration

$$g_j(\mathbf{x}+\mathbf{e}_j, t+1) = g_j(\mathbf{x}, t) + \frac{1}{\tau_G}[g_j^{\mathrm{eq}}(\mathbf{x}, t) - g_j(\mathbf{x}, t)], \tag{4.19}$$

where the velocity index $j = 1, \ldots, 4$ (see Eq. 4.2). The relaxation time τ_G is related to the diffusion coefficient of the dissolved volatiles in the melt

$$D_{\mathrm{H_2O}} = c_{sG}^2 \left(\tau_G - \frac{1}{2}\right), \tag{4.20}$$

and the constant $c_{sG}^2 = 1/2$ for the D_2Q_4 lattice. The local dissolved water content is retrieved from the distribution with

$$C(\mathbf{x}, t) = \sum_{j=1}^{4} g_j(\mathbf{x}, t), \tag{4.21}$$

and the equilibrium distribution is given by

$$g_j^{\mathrm{eq}}(\mathbf{x}, t) = w_{j,G} C(\mathbf{x}, t) \left(1 + \frac{\mathbf{e}_j \cdot \mathbf{u}}{c_{sG}^2}\right), \tag{4.22}$$

where the velocity $\mathbf{u}$ is obtained from the Navier-Stokes solver (from the distributions f_i), $w_{j,G} = 1/4$ for $i = 1, \ldots, 4$ are the lattice weights for the distributions g_j corresponding to the four discrete velocity vectors $\mathbf{e}_j$ which point (East-North-West-South, see Fig. 4.1). The equilibrium distribution are therefore a function of the local flow velocity and the local concentration only. The water-dependence of the diffusivity can be easily included in the model by setting the relaxation time τ_G to be function of the dissolved water content C. This effect will not be explored here, but will part of a subsequent study. This lattice Boltzmann model for advection diffusion was shown to recover the advection-diffusion equation [190]

$$\frac{\partial C}{\partial t} + \mathbf{u} \cdot \nabla C = \nabla \cdot (D_{\mathrm{H_2O}} \nabla C). \tag{4.23}$$

I impose the dissolved water content in the melt at a bubble-melt boundary to follow Henry's law

$$C_b(\mathbf{x}, t) = S\sqrt{p_g}, \quad \mathbf{x} \in \text{Interface cell} \tag{4.24}$$

with S the Henry's constant and p_g the bubble's pressure [182]. This boundary condition at the interface site is imposed by setting the missing distributions (coming from the adjacent gas-cell) g_x to

$$g_x = g_x^{\mathrm{eq}}(C_b, \mathbf{u}) + g_{\bar{x}}^{\mathrm{eq}}(C_b, \mathbf{u}) - g_{\bar{x}}(C_b, \mathbf{u}), \tag{4.25}$$

while the other g_j's are set to $g_j(C_b, \mathbf{u})$. In Eq. 4.25, the overbar defines the opposite velocity direction, e.g., $\bar{1} = 3$. The bubble model, including the diffusion of the dissolved volatiles, at the exception of the decompression scheme, has been validated in previous studies [92].

As one of my long term interests is to allow for degassing and bubble growth during decompression, the decompression rate $(dp/dt)_{\mathrm{dec}}$ should be included into the advection-diffusion scheme for dissolved water in the melt. As the pressure exerts only a second order effect on the diffusivity of dissolved water in the melt, I will not consider this effect here. Following the decompression scheme described above, where the pressure reference-frame follows the pressure of the ambient melt, the decompression rate is expected to play a role in the solubility of water at the bubble-melt interface. I therefore introduce the decompression of the suspension into the boundary condition with

$$C_b(\mathbf{x}, t) = S\sqrt{p_g + \int_0^t \left(\frac{dp}{dt}\right)_{\mathrm{dec}} \mathrm{dt}}. \tag{4.26}$$

A first note concerns the sign of $(dp/dt)_{\mathrm{dec}}$, because it is negative the decompression term leads to a decrease in solubility with time. It is important to note, however, that if the bubble growth is limited by the viscosity of the ambient melt, the overpressure buildup in the bubble in response to the decompression can ideally compensate for the decompression of the magma and, in that particular case, the solubility of water at the bubble interface should remain constant as is expected from the expression above.

4.4 Validations

A detailed description of benchmark problems solved with the generic free surface lattice Boltzmann model can be found in Ref. [92]. Here, I focus on validations regarding the additions I made to the model: the decompression scheme.

4.4.1 Single and multiple bubble growth by expansion during decompression

The following calculations are meant to test if the pressure evolution equation (Eq. 4.17) allows one to solve for the expansion of a bubble or a bubble suspension (up to 120 different bubbles) during a constant decompression rate experiment, in the absence of degassing (no diffusion growth). All the runs presented here use similar initial conditions, I normalize pressure with regards to the initial ambient pressure $p_{\text{amb}}(t = 0) = 1$, and start with $N = 1, 5, 40, 120$ bubbles with a given initial radius r_0 (initially monodisperse size distribution). The physical domain can be decomposed in two main regions, the suspension (melt+bubbles) that occupies the lower half and a free surface with a fictitious atmosphere in the upper half. The presence of the free surface and atmosphere is required to allow for the suspension to expand (increase in volume). The whole domain is bounded by solid walls and is isochoric (constant total volume during decompression). In all the following calculations, I use a constant decompression rate with a duration Δt (5000 time steps in my simulation) so that

$$\left(\frac{dp}{dt}\right)_{\text{dec}} \Delta t = -\frac{3}{4}\, p_{\text{amb}}(t = 0). \tag{4.27}$$

For a single bubble, I should therefore expect the final volume of the bubble to be four times greater than its initial volume, given that enough time is allowed for the bubble-melt system to relax to a new steady-state. In Fig. 4.2, I show the evolution of a single bubble during a decompression experiment (the decompression lasts for only half of the calculation time, i.e., 5000 time steps). In general, starting with N bubbles each with an initial volume V_0 and a volume of melt (incompressible, constant) V_m, I get by mass conservation between the initial and final stages

$$\frac{NV_0}{NV_0 + V_m} = \mathcal{C}\frac{4 \times NV_0}{4 \times NV_0 + V_m}, \tag{4.28}$$

where $\mathcal{C}$ is the expansion factor and V_m can be calculated from the vesicularity ϕ of the suspension at $t = 0$. I can compare the value of $\mathcal{C}$ obtained theoretically with Eq. 4.28 with the ratio of final to initial suspension vesicularity in my calculations. In Tab. 4.1, I use the initial vesicularity in my calculations to compute the theoretical expansion factor and final vesicularity, these results are then compared graphically with the timeseries of increasing

vesicularity obtained numerically with my decompression model (see Fig. 4.3). I observe that in all cases, even when coalescence is prominent (the run containing intially 120 bubbles reaches a steady-state with 29 bubbles), the agreement is excellent between the numerical model and the theory. Because coalescence does not have a significant importance on the final steady-state vesicularity of a decompressed suspension, I used an arbitrary value for the constant c_Π that controls the amplitude of the disjoining pressure term. In the following calculations, the coalescence rate becomes important and I will calibrate the disjoining pressure constant value with laboratory experiments.

4.4.2 Growth of a single bubble

An empirical test for my model is to reproduce the qualitative features observed in other numerical models and laboratory experiments during the growth of a single bubble by diffusion and expansion during a linear decompression event. First, when the bubble is small and the diffusive flux of water to the bubble interface can be neglected, the growth of the bubble is delayed [97,103,152,154,182]. Ref. [97] showed that under this growth regime (often referred to as viscous-limited growth regime), the bubble radius grows exponentially and the argument of the exponential growth depends on the timescale for viscous relaxation t_{visc} and the timescale for decompression t_{dec} [63,97]

$$\frac{R(t)}{R_i} = \exp\left(\frac{t*^2}{2}\frac{t_{dec}}{t_{vis}}\right), \tag{4.29}$$

where $t* = |dp/dt|t$,

$$t_{vis} = \frac{4\mu}{p_i} \tag{4.30}$$

$$t_{dec} = \frac{p_i}{|dp/dt|}, \tag{4.31}$$

with the subscript i referring to an initial condition (prior to decompression), p_i the initial ambient melt pressure and μ is the dynamical viscosity of the melt, here assumed constant. In Fig. 4.4, I show the volume and radial growth of the bubble obtained with my model. The different insets correspond to snapshots taken at different times during the growth. I clearly observe an early exponential growth stage that is consistent with the time-delay process observed in other numerical models [97,103,152,154]. As the bubble grows, the balance for

Table 4.1: Summary of results from the decompression of a bubble suspension

$N(t=0)$	$\phi(t=0)$	$N(\Delta t)$	$\mathcal{C}$ theory	$\mathcal{C}$ calculated	$\phi(t=\Delta t)$
1	0.019	1	4	4	0.076
5	0.0099	5	3.08	3.11	0.0308
40	0.077	27	3.27	3.273	0.252
120	0.22	29	2.42	2.418	0.532

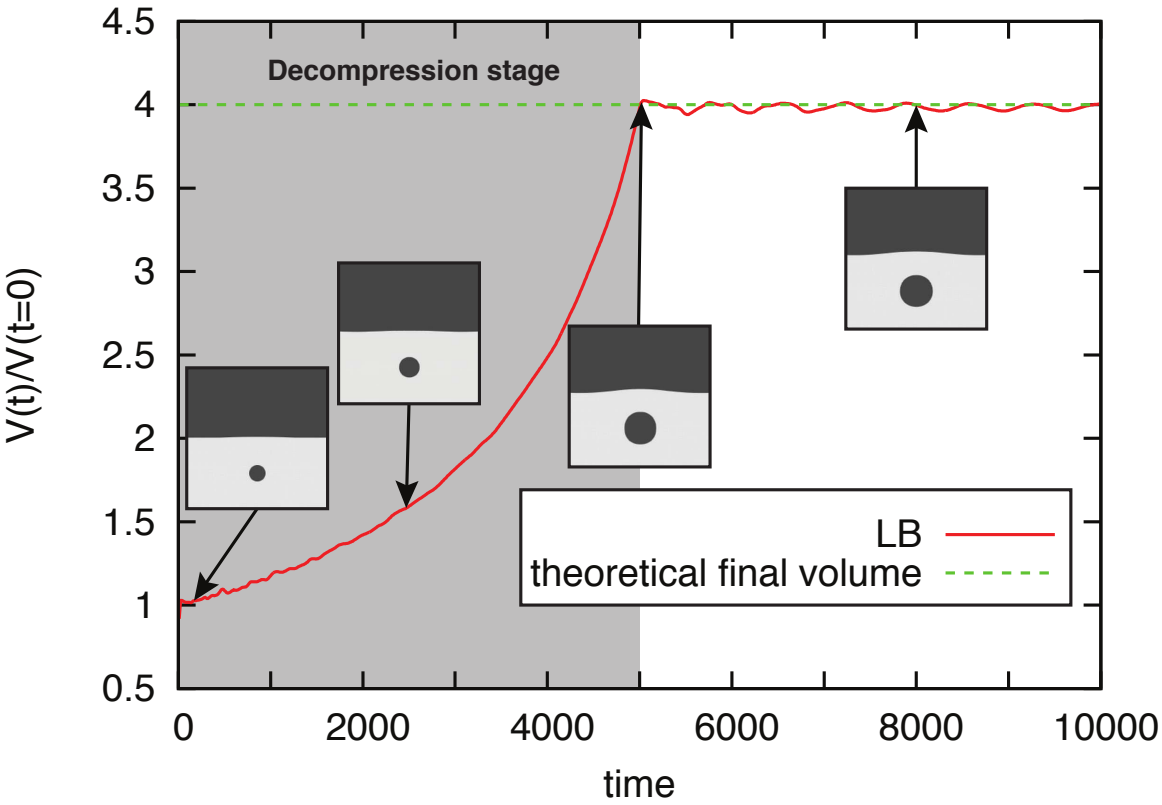

Figure 4.2: Linear decompression of a bubble. The decompression phase lasts for 5,000 iterations. Here only mechanical expansion is allowed (no diffusion) and the bubble reaches its final expected size (see dashed line) after decompression. The oscillations observed around the steady state are caused by capillary waves generated at the free surface by the growth of the bubble during the decompression phase.

growth becomes different and displays the usual sigmoidal radius growth observed in other models [152, 154].

4.5 Bubble-bubble interactions

The interaction between bubbles in a suspension is highly non-linear and has been neglected in existing bubble dynamics models in physical volcanology. This results in serious limitations of these models when applied to magma ascent during eruptions. The focus of my model is to account for these non-linear interactions between bubbles under a range of realistic magmatic conditions. In this section, I demonstrate the ability of the model to treat bubble thermo and hydrodynamic interactions during diffusion (Ostwald ripening), deformation and coalescence.

4.5.1 Diffusion and Ostwald ripening

In a polydisperse bubble suspension, diffusion coarsening, often referred to as Ostwald ripening, can lead to the growth of large bubbles at the expense of smaller ones [96]. A similar process is known to operate during the growth of crystals in magmatic and high temperature metamorphic environment [127, 144]. This process occurs because the growth of large bubbles (or crystals) and the disappearance of smaller ones is more favorable in terms of surface energy.

This coarsening process was first recognized by Ref. [138], but it took about 60 years to establish a theory that yields quantitative predictions. The physics underlying the coarsening is simple: because of surface tension, small bubbles have a higher gas pressure than larger ones. In fact, assuming static conditions the difference in pressure between two spherical bubbles with radius r_1 and r_2 is

$$\Delta p = p_1 - p_2 = 2\sigma \left(\frac{1}{r_1} - \frac{1}{r_2} \right). \tag{4.32}$$

The pressure difference increases with bubble volume differences and surface tension. The

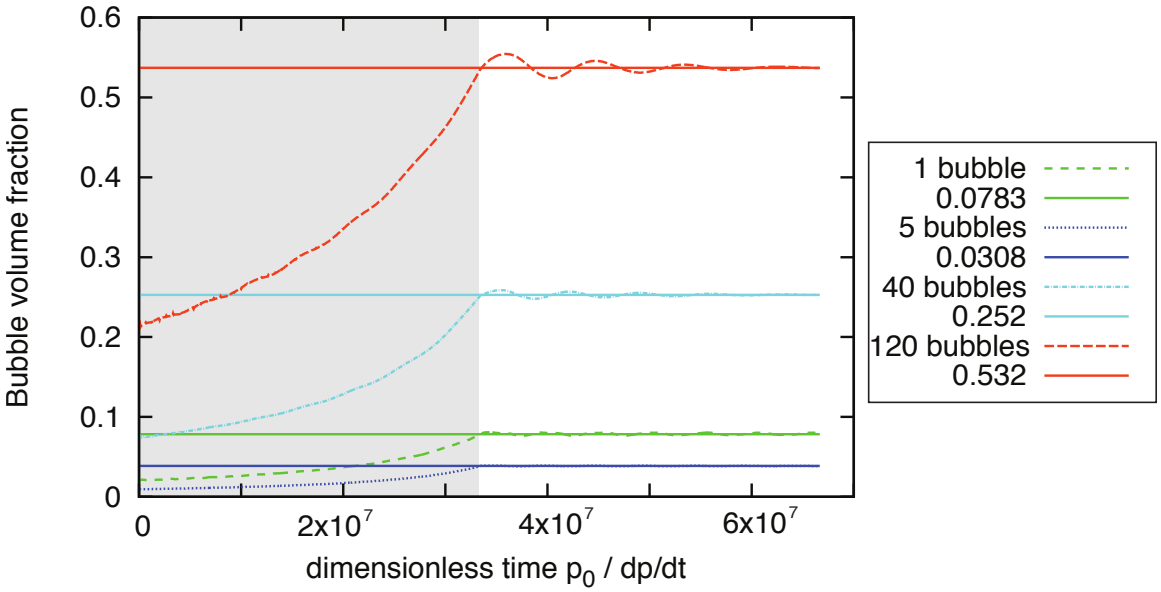

Figure 4.3: Same exercise as for Fig. 4.2 but with a different amount of bubbles. It is interesting to note that the runs at higher vesicularity hosted a large amount of coalescence, but it did not affect the accuracy of the decompression scheme.

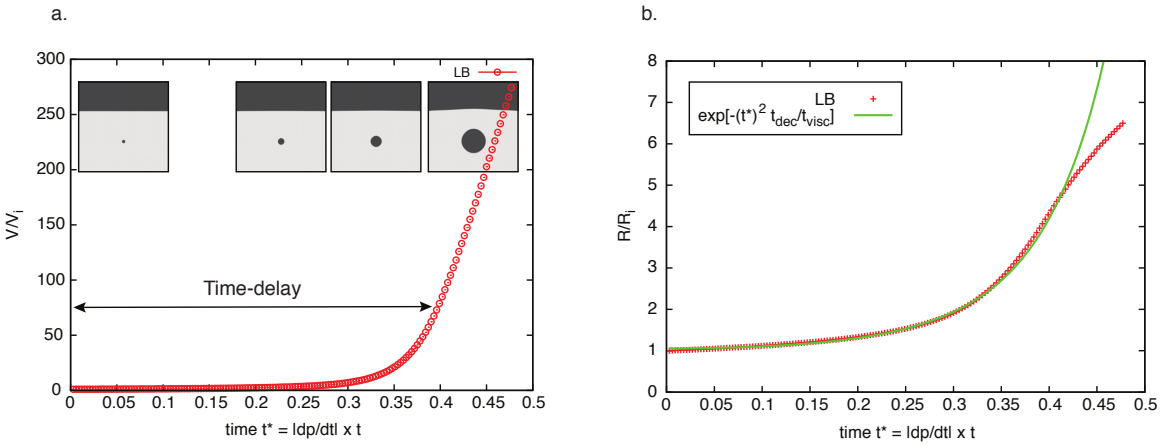

Figure 4.4: Illustration of the growth of a bubble by a combination of mechanical expansion and diffusion during decompression. In panel (a), the inset illustrate the size of the growing bubble and shows clearly the time-delay caused by the viscosity of the ambient melt at the onset of the growth. Panel (b) shows a fit of my results with the exponential growth derived for early growth by Ref. [97].

diffusion of dissolved water from a small to a large bubble is caused by the the pressure-dependence of the solubility condition at the bubble-melt interface (Henry's law)

$$C_1 = S\sqrt{p_{\text{amb}} + \frac{2\sigma}{r_1}} \tag{4.33}$$

$$C_2 = S\sqrt{p_{\text{amb}} + \frac{2\sigma}{r_2}}, \tag{4.34}$$

if $r_1 < r_2$, then $C_1 > C_2$ and water will diffuse from the small to the large bubble, further increasing the capillary pressure difference and the coarsening process. The development of analytical models with predictive capabilities is however not simple.

A major difficulty for modeling this process arises from the boundary conditions, the concentration of dissolved water changes over time and so does the position of the two boundaries as one bubble shrinks and the other grows. The first predictive models were based on highly idealized bubble population statistics, such as the LSW model developed by Lifshitz and Slyozov [100] and Wagner [205]. These models assumed that the bubble remains spherical at all time, and more importantly, that the suspension is dilute, the interaction between bubbles was replaced by a mean-field interaction. These models predict that, during steady coarsening, the average bubble radius increases with time$^{1/3}$ for diffusion-controlled growth. Recently, more sophisticated models of population dynamics emerged, like the model of Ref. [37] where the mean-field approximation was replaced by a nearest-neighbor interaction. Theoretical models of transient coarsening are still built on a large number of simplifying assumptions and a theoretical model that allows to account qualitatively for Ostwald ripening processes remains challenging.

For magmatic suspensions, Refs. [118, 119] discussed vesicle size distribution in basaltic magmas (VSD, equivalent to BSD) erupted either effusively or explosively. Although the importance of diffusive coarsening was not directly measured in the skewed VSD distribution, the faster diffusion and also broader range of radii among coexisting bubbles make basaltic magmas more prone to display efficient diffusion coarsening. Estimates of the duration for the diffusive exchange of water between bubbles separated by a melt film was discussed by Proussevitch and co-workers, using again some important assumptions such

as steady-state diffusion and simple geometry [152]. Under these assumptions, they anticipated that the radius of the shrinking bubble had to decrease with the square-root of time. This model does not take into account the change in film thickness that is expected to happen during the process. Ref. [96] presented laboratory experiments to study Ostwald ripening in magmas with different compositions (mafic andesite to rhyolite). They showed that, in agreement with a multitude of other laboratory experiments, the temporal evolution of the bubble's radius expected from the LSW theory is not obtained. They concluded that transient coarsening with widely variable growth rates was more susceptible to be relevant during fast degassing event such as during the ascent of bubbles in a volcanic conduit.

Available bubble growth models in physical volcanology can not account for diffusive coarsening. This is because these models are either assuming that the suspension is monodispersed (no gradients of solubility) or because they do not solve explicitly for volatile diffusion around individual bubbles [50,199,217]. Recently, Ref. [217] expanded on the polydispersed model of Ref. [199] and introduced a critical radius below which bubbles where made to disappear to the benefit of larger bubbles. To a first order, they argued that the forced disappearance of bubbles smaller than this critical radius could account for Ostwald ripening, but the process is not explicitly solved for. In realistic scenarios, at high vesicularity, it is likely than the coarsening of a volcanic foam can involve more than two partner bubbles of different sizes.

My model allows one to model diffusive coarsening, because I can solve explicitly for the dynamics of multiple bubbles with various sizes and water diffusion from and to neighboring bubbles. In Fig. 4.5, I show an attempt of modeling Ostwald ripening, where two bubbles of different initial sizes ($r_1 = 7$ and $r_2 = 30$ grid spacing) are initially separated by 4 lattice nodes. The large bubble is initially in chemical equilibrium with the host melt. While the smaller bubble loses water over time by diffusion, the pressure and temperature remain fixed during this run. Although a comparison of the model with an analytical or asymptotical solution remains mostly qualitative, this calculation highlights the potential of the method to resolve complex thermodynamical interactions between neighbor bubbles. As I expect, the total volume/mass of exsolved volatiles remains constant throughout the run (dotted

line in the two upper panels), but the volume of the small bubble decreases with time while the larger bubble grows.

Assuming steady-state diffusion, bubble growth in melt has been shown to follow a parabolic growth rate $r^2 \propto t$. Similarly, the diffusive exchange of water across a melt film separating two close bubbles of different sizes is expected to yield a parabolic shrinking rate [152]

$$r_0^2 - r^2 \propto (t - t_0), \tag{4.35}$$

where r_0 is the bubble radius at time $t_0 < t$. This scaling between the shrinking rate and time is valid mostly for the early stage of the mass exchange, when the size of the small bubble has not changed significantly. In Fig. 4.6, I compare the numerical results for the evolution of the small bubble size with the scaling above and find a great agreement for the first phase of the calculation. The latter stage of the calculation is marked by an faster shrinking rate. The acceleration in shrinking rate is caused by two effects. The first effect is that while the bubble's volume decreases, the boundary of the small bubble recedes faster than the large bubble boundary advances because of the different surface to volume ratios of the two bubbles. This leads to a change in film thickness that affects the idealized parabolic shrinking law. The second effect is merely numerical; when the shrinking bubble becomes small, the spatial resolution becomes more limited and the results less accurate.

4.5.2 Calibration of the model for coalescence with laboratory experiments

During bubble coalescence, a melt film separating the bubbles drains and shrinks until a critical thickness (δ_{crit}) is reached and the film suddenly ruptures. Capturing the exact physics of this phenomenon is impossible from the numerical point of view, because the complex dynamics in the film occurs ultimately at scales significantly smaller than the effective radius of the bubbles ($\delta_{crit} \sim 10^{-7}$m), and the dynamics of the film rupture is much faster than the drainage and poorly constrained. The model I propose offers two advantages over standard multiphase LB models where bubble coalescence occurs automatically when the two free surfaces approach each other to within a computational grid cell. First, the mass conservation during the drainage of film fluid is resolved locally to a subgrid-scale

(Eq. 4.10). Second, and most importantly, an additional pressure term is introduced in the stress boundary condition at each free surface to account for the interaction between neighbor free surfaces, the disjoining pressure (Eq. 4.14). The disjoining pressure term is expected to become significant for surfactant rich interfaces, where foams can become stable over much longer timescales. I use c_Π as a free parameter to account for the subgrid effects of lubrication forces on the stabilization of the film prior to rupture.

In order to calibrate the disjoining pressure term, I designed the simplest experiment that accounts for two approaching and distinct free surfaces: a bubble approaching and bursting at a free surface. In the laboratory, air bubbles where injected into silicon oil (using a range of oil viscosity) [130]. I decided to use these experiments to calibrate the disjoining pressure dependence on the Bond number Bo= $\Delta\rho g R^2/\sigma$. Fig. 4.7 shows a visual comparison between two selected experiments and a numerical calculation with my free surface model. The duration of the film drainage between the bubble and the free surface was measured over a range of bubble radii. In the experiments, the flow regime is viscous, i.e., inertial forces are negligible. The reader is referred to Ref. [130] for a thorough description of the experimental setup. The experiments revealed the existence of two regimes of film drainage at low Re, depending on the balance between buoyancy and surface tension stresses (Bond number). At Bo < 0.25, in the capillary-dominated regime, the film drainage is caused by surface tension, and the characteristic timescale for drainage was found theoretically and experimentally to be

$$t_c = C_c \ln\left(\frac{\delta_0}{\delta_{crit}}\right)\frac{\mu R}{\sigma}, \tag{4.36}$$

where *sigma* is the surface tension between the two immiscible fluids, R the effective bubble radius, μ the dynamic viscosity of the ambient fluid, δ_0 the initial film thickness (before drainage) and C_c a constant which value was found experimentally to be about 20 [36, 130]. The ratio δ_0/δ_{crit} was estimated from natural samples to be of the order of 10^2 to 10^3.

As buoyancy stresses become more important (Bo > 0.25), the drainage regime is governed by the balance between buoyancy and viscous stresses. The drainage time is then

$$t_g = C_g \ln\left(\frac{\delta_0}{\delta_{crit}}\right)\frac{\mu}{\Delta\rho g R} = \frac{C_g}{C_c}\,\mathrm{Bo}\,t_c, \tag{4.37}$$

where $\Delta\rho$ is the density difference between the bubble and the ambient fluid. The two empirical constant C_c and C_g were found experimentally to be 20 and 5 respectively.

The same general setup was used for the numerical calculations, a buoyant bubble is initially emplaced about 10 bubble radii below the unperturbed free surface. I compute the bubble's ascent, deceleration as it approaches the free surface and record the drainage time leading to the bubble rupture at the surface. The drainage time is defined similarly between the experiment and the calculations, it consists of the time interval between the sharp slowdown of the bubble as it approaches the free surface (the center of mass decelerates from a velocity close to the free ascent velocity for the bubble to rest) and the rupture of the film when it reaches its critical thickness δ_{crit}.

The disjoining pressure defined in Eq. 4.16 includes two constants c_Π and the range of the interaction between free surfaces d_{range}. The latter was fixed to the same distance, 3 gridpoints, as in the study of Ref. [92]. I decided to keep d_{range} fixed and calibrate the disjoining pressure by varying the constant c_Π so as to reproduce the dimensionless drainage time observed experimentally over a range $0.1 \leq \text{Bo} \leq 4$ that overlaps both drainage regimes (capillary and gravity-driven). As expected, an increasing magnitude for c_Π yields a longer drainage time, as shown in Fig. 4.8 taken at $\text{Bo} = 1$. One can clearly see the bubble slowing down as it interacts with the free surface and the subsequent film drainage leading to the bubble's rupture.

I repeated similar calculations over a range of Bo varying the value of c_Π (Fig. 4.9). I ran each calculations for about 200,000 iterations (in all case much longer than the expected experimental drainage time) to map the regime where coalescence occured. I found that there is a critical disjoining pressure constant value where the two bubbles remained stable, and, that this value depends on Bo.

The experimental normalized drainage time was found to satisfy

$$\frac{t_d}{t_x} = \begin{cases} 1 & \text{if Bo} < 0.25 \text{ and } x = c \\ 1 & \text{if Bo} > 0.25 \text{ and } x = g. \end{cases} \tag{4.38}$$

Fig. 4.10b shows the best fit for c_Π to match the experimental results. Because of the

two drainage regimes (below and above Bo = 0.25), the calibrated value for c_Π becomes

$$c_\Pi(\mathrm{Bo}) = \begin{cases} 1.57 \times 10^{-3}\mathrm{Bo} + 1.59 \times 10^{-5} & \text{if Bo} < 0.25 \\ 1.27 \times 10^{-4}\mathrm{Bo}^{2.1} + 6.6 \times 10^{-4} & \text{if Bo} > 0.25. \end{cases} \tag{4.39}$$

In the near future, I plan to conduct similar type of combined experimental-numerical effort to constrain the dependence of the disjoining pressure Π on the Capillary number (shear to surface tension stresses). In the latter case, bubble deformation and its feedback into capillary stresses can significantly impact the film drainage rate during coalescence.

4.5.3 Sheared suspensions

The effect of dispersed bubbles on the rheology of magmas has been studied theoretically and experimentally [115,116,183,186,193]. It was found that the presence of bubbles induces a shear thining behavior, i.e., the effective viscosity decreases with increasing strain-rates. Bubbles influence on the effective viscosity are strongly controlled by the capillary number. At low Ca, when bubbles remain spherical because surface tension dominates the force balance at the scale of the bubbles, the effective viscosity is greater than for a melt with no bubbles. At large Ca (> 0.1), when bubbles can accomodate a substantial part of the deformation in the suspension, bubbles decrease the effective viscosity of the mixture. The importance of the suspension vesicularity has also been studied extensively and it was shown that the viscosity of the suspension increases weakly with vesicularity, at least in the limit of low vesicularity studied ($< 10\%$ in most cases). Here, I discuss the effect of a constant imposed shear-rate on a suspension and, more specifically, I focus on the deformation and orientation of these bubbles in response to an imposed simple shear.

The evolution of a sheared suspension is important because the rheology of the mixture is sensitive to the bubble size distribution, i.e., small bubbles can increase the effective viscosity of the mixture because of their resistance to deformation (low Ca), whereas large bubble will tend to accomodate most of the strain and therefore reduce the effective viscosity of the suspension. In this study, I explore the behavior of suspension over a range of imposed shear-rates (I fix the initial bubble size, and hence the initial bubble Ca), but I do not account for degassing. The aim of these calculations is (1) to validate my bubble dynamics

calculations under shear conditions with published theory and experiments for a single bubble, and, (2) to investigate the role of bubble interactions on the distribution of bubble shapes and orientations.

I present three sets of calculations. First, I compare and validate my numerical results for the steady shape and final orientation of a single bubble under simple shear conditions with theoretical and experimental results obtained by Refs. [73, 157, 160]. The second set of calculations aims at characterizing how the presence of other bubbles with the same size (dealing now with a monodisperse suspension) affects the distribution (average and standard deviation) of deformation and orientation in a suspension. Finally, introducing a bimodal initial bubble size distribution, I test the effect that smaller bubbles (more difficult to deform) have on the deformation and orientation of larger ones.

The LBM offers a very convenient approach to impose velocity boundary conditions on solid sites. I use the boundary condition of Ref. [227] to impose a velocity $(U_w, 0)$ at the lower wall and a standard bounceback of the distribution for the no-slip boundary condition on the top wall (see Fig. 4.11). The missing distribution in melt-sites adjacent to the lower boundary (moving wall) are f_2, f_5 and f_6, i.e., the distributions i with $\mathbf{e}_i \cdot \mathbf{n}_y > 0$, where $\mathbf{n}_y$ is the upward (+y) normal to the wall

$$\rho = f_0 + f_1 + f_3 + 2\,(f_4 + f_7 + f_8) \tag{4.40}$$

$$f_2 = f_4 \tag{4.41}$$

$$f_5 = f_7 + \frac{1}{2}\,(f_3 - f_1) + \frac{\rho U_w}{6} \tag{4.42}$$

$$f_6 = f_8 + \frac{1}{2}\,(f_1 - f_3) - \frac{\rho U_w}{6}. \tag{4.43}$$

The capillary number Ca that represents the ratio of viscous to surface tension stresses is defined as

$$Ca = \frac{\rho \nu U_w r}{H\sigma}, \tag{4.44}$$

where r is the initial bubble size, ρ and ν refer respectively to the melt density and kinematic viscosity [186]. If the capillary number is identical for each bubble initially, coalescence will lead to a polydisperse bubble size distribution and therefore lead to a range of Ca in the suspension. In all these calculations, the domain is bounded on the sides by periodic

boundaries and the whole system is oriented perpendicular to the direction of gravity (no buoyancy effect).

If the viscous stresses are negligble with respect to surface tension stresses (Ca $\ll 1$), the bubble remains undeformed (spherical) and remains invariant under the rotation. With increasing Ca, the bubble starts to deform and loses its spherical symmetry. The bubble therefore rotates until the drag force applied by the melt to the bubble balances surface tension (here I only consider flows where inertia can be neglected). The elongation of the bubble, once it reaches a steady shape, is often characterized by the dimensionless quantity

$$D = \frac{l - b}{l + b}, \tag{4.45}$$

where l and b are respectively the long and short semi-axis of the elliptic or pseudo-elliptic final shape [73,160]. It is easy to see that $0 \leq D < 1$, where the two bounds hold respectively for an undeformed spherical bubble ($D = 0$) and an infinitely elongated bubble. Finally, the angle between the long axis of the bubble and the direction of the shear is defined as θ (see Fig. 4.11 for an illustration of these definitions on results from calculations conducted at Ca = 0.2 and 0.5).

4.5.3.1 Validation of the model for the deformation of a single bubble under simple shear

Since the seminal work of G.I. Taylor, the deformation of inviscid or nearly inviscid bubbles under shear flow conditions as been studied extensively [73, 157, 160]. These studies have yield many important results, in a context of a single deforming bubble, I will focus on the following set of theoretical and experimental results to test my model. First, for moderate Ca, i.e., Ca $< 10^3$, such as those expected under most magmatic conditions, bubbles are expected to reach a steady configuration and not break into smaller bubbles [11,73]. Second, for low Ca, i.e., Ca ≤ 0.5, the deformation of the bubble follows

$$D \simeq \mathrm{Ca} \tag{4.46}$$

as shown by Ref. [193]. Under the same conditions (low Ca), the orientation of the bubble reaches

$$\theta = \frac{\pi}{4} - 0.6\mathrm{Ca}. \tag{4.47}$$

At greater Ca (≥ 1), Ref. [73] derived theoretically that the ratio of the steady of the elongated semi-axis of the bubble to its initial radius R follows

$$\frac{l}{R} \simeq 3.45\mathrm{Ca}^{1/2}, \tag{4.48}$$

which, assuming a 2-D ellptical bubble, yields

$$D \simeq \frac{11.9\mathrm{Ca} - 4}{11.9\mathrm{Ca} + 4}. \tag{4.49}$$

Similarly, they showed that, for large Ca, the orientation of the bubble at steady-state is given by

$$\theta = \arctan\left(0.359\mathrm{Ca}^{-3/4}\right). \tag{4.50}$$

Rust and Manga demonstrated the validity of these relationship experimentally and pinned the transition from low to high Ca regimes to occur around $\mathrm{Ca} = 0.5$.

I run simple shear calculations in a 200×100 gridpoints domain over a range of shear-rate conditions ($0.1 \leq \mathrm{Ca} \leq 4$). For each run, the bubble shape and orientation was measured at steady-state. My first test consist in a comparison between my numerical results, theory and the laboratory experiments of Ref. [160] for the shape and orientation of the bubble across a range of Ca. Fig. 4.12 shows a very good agreement between both datasets and with Eqs. 4.46 and 4.49. It is important to remember, however, that my calculations are limited to 2-D (temporarily, as I work on a 3-D extension). As such, some of the small-scale discrepancies could be associated with the planar velocity field imposed by the 2-D symmetry in my calculations. The final orientation of the bubble agrees very well with the experiments of Ref. [160] and the scaling relationships presented in Eqs. 4.47 and 4.50. I also find the transition between surface tension to viscous stress dominated regime to be around $\mathrm{Ca} = 0.5$, similarly to Ref. [160]. Finally, the relationship between the deformation D of the bubble and its orientation θ also follows the experimental results of Rust and Manga. This gives good confidence that my model captures accurately the stress balance at the interface between a bubble and the ambient melt.

4.5.3.2 Deformation and orientation of a mono-disperse suspension of bubbles

I conducted similar simple shear flow calculations with a suspension of 20 bubbles with an initial radius of R. The initial position of each bubble was set randomly and I repeated each calculation (for each choice of Ca) 3 times to get a sense for the variability of my results with respect to these random initial conditions. The goal of these calculations is to study the effect of other bubbles (suspension) on the distribution of θ and D values over a range of capillary numbers and contrast those results with those for a single bubble.

In a suspension, the existence of a steady state is not guarantied, especially when Ca becomes large. This is because shear promotes coalescence [132,133] and coalescence affects the effective Ca of the suspension (as the average bubble radius increases at the detriment of the bubble number density). Therefore, instead of focusing on the steady deformation and orientation of the bubbles, I consider their temporal evolution parameterized in terms of accumulated strain ($\epsilon = U_w t/H$) and measure the distribution of D and θ at a few discrete values of ϵ. This also allows one to compare the behavior of the suspension under different shear conditions. I tried, as much as possible, to consider calculations where the amount of coalescence was minimal and where the effect of bubbles on neighbor bubbles is mostly limited to the deformation of streamlines.

In Fig. 4.13, I show the evolution of the average deformation $\langle D \rangle_m$ and average orientation $\langle \theta \rangle_m$ of the suspension over strain accumulation ϵ for Ca=0.1, 0.25, 0.5, 1, where

$$\langle D \rangle_m = \frac{1}{N_b} \sum_{k=1}^{k=N_b} D_k \tag{4.51}$$

$$\langle \theta \rangle_m = \frac{1}{N_b} \sum_{k=1}^{k=N_b} \theta_k, \tag{4.52}$$

N_b is the total bubble number. Figs. 4.13c and 4.13d illustrate the state of the suspension with color coding for the melt velocity for Ca = 0.1 and Ca = 1 respectively at $\epsilon \approx 6.923$. Suspension reaches a quasi-steady state after $\epsilon \approx 2 - 3$ as seen from panels a-b. The steady state is defined as fluctuation around a constant value of $\langle D \rangle$ and $\langle \theta \rangle$. At lower Ca (< 0.5), when interfacial tension stresses σ dominate, the steady state is characterized by $\langle D \rangle_m > D_s$, where $'m'$ denotes multi-bubbles cases, while $'s'$ is for single bubble case.

At higher Ca, when viscous shear stresses dominate, I can get the reverse result that is $\langle D \rangle_m < D_s$. For the average orientation, $\langle \theta \rangle_m$ is higher than θ_s at higher Ca. However, at lower Ca, it is not very obvious that which is larger from the figure.

The bubble number N_b being modest and their initial distributions being random, I ran 3 realizations for each set of calculation with different random initial positions for the bubbles. Fig. 4.14 presents results at Ca = 0.1 and Ca = 1. In case Ca = 0.1, the three runs match each other perfectly, all of which are almost overlap each other; for the Ca = 1, the curves still match each other very well except for some slight differences. The results are therefore reproducible regardless of initial bubble positions.

Generally, bubbles deform less compared to a single bubble at a given Ca above 0.5, whereas the deformation in the suspension exceeds prediction from a single bubble at Ca < 0.5. Bubble volume fraction Φ, which is fixed in my multi-bubble suspension tests ($\Phi \approx 0.14$), and bubble shape and orientation can affect the effective Ca* of suspensions by influencing the effective viscosity ν^*. From Eqn(44), the effective Ca* of bubbly suspension can be defined as follows,

$$Ca^* = \frac{\rho \nu^* U_w r}{H \sigma}. \tag{4.53}$$

Previous studies showed that low Re suspensions, with Ca in the range of (0, O(1)) are shear thinning [45, 68, 116, 160], which is to say the effective viscosity ν^* is decreasing when increasing Ca through increasing shear strain rate $\dot{\epsilon} = U_w/H$. Although ν^* is decreasing with increasing Ca, ν^* of multi-bubbles suspension system behaves differently in different range of Ca with respect to ν of the suspension melt. The ratio of ν^* and ν is above one ($0 < \text{Ca} < \text{Ca}_c$), and lower than one ($\text{Ca}_c < \text{Ca} < O(1)$), where the critical capillary number $\text{Ca}_c \approx 0.5 - -0.7$. Fig. 6 in Ref. [116] explained it in the following way: At lower Ca, bubbles stay spherical, the effective viscosity increases with Φ because the deformed streamline provide a net increase of viscous dissipation that is not compensated by the volume of quasi inviscid bubbles. At higher Ca, the elongated bubbles tilt almost horizontally providing the resistance to the flow of ambient melt. In addition, deformed bubbles can slide over each other in higher Ca, which, due to bubble wall's free surface properties, can help to reduce the viscous dissipation. Fig. 5 in Ref. [160] showed their experiment results of relation

between $\frac{\nu^*}{\nu}$ and Ca. Bubbles with Ca $<$ Ca$_c$ experience a greater ν^* of ambient melt with increasing Φ, while bubbles at higher Ca experience a reduced ν^*. My results are in good agreement with their studies.

My model offers a accurate description of bubble-bubble and bubble-melt hydrodynamic interactions. In the near future, I plan to explain how bubble deformation under shear flow conditions affects growth by exsolution. Bubble deformation leads to a greater interfacial area btween bubbles and melt which can promote faster degassing than expected from the models of Refs. [50, 97, 99, 111, 152, 154, 199].

4.6 Conclusions

The goal of this study was to develop a bubble growth model in magmas that accounts for bubble-bubble interactions hosted in a melt at rest or subjected to shear flow conditions, and obtain a more accurate description of the dynamics of bubbles during the ascent of magma to the surface. The model I propose is based on an adaptation of the free surface lattice Boltzmann model. I added a decompression algorithm to study the growth of bubbles by mechanical expansion and diffusion. The model was validated against analytical solutions and results from other bubble growth models. The advantages of this model over existing bubble dynamics models is that it allows to account for the complex non-linear dynamics of bubbles growing in a silicate melt as the vesicularity increases and bubble-bubble and bubble-structure (shear flow near conduit walls for instance) interactions become more important. The model also includes a free parameter (the disjoining pressure constant) that allows one to fine tune the model against laboratory experiments to reproduce accurately coalescence.

After the description and validation of the model, I conducted bubble dynamics calculations that involve non-linear dynamical aspects that are not accounted for in other models such as Ostwald ripening and bubble(s) deformation under simple shear flow conditions over a range of capillary numbers. The model is able to reproduce the scaling expected for Ostwald ripening, which confirms its ability to handle mass transfer of dissolved water between bubbles of different sizes. On the other hand, the simple shear flow calculations for

a single bubble follow accurately the scalings and experimental results obtained in previous studies, confirming that my model solves accurately the viscous coupling between a bubble and the melt.

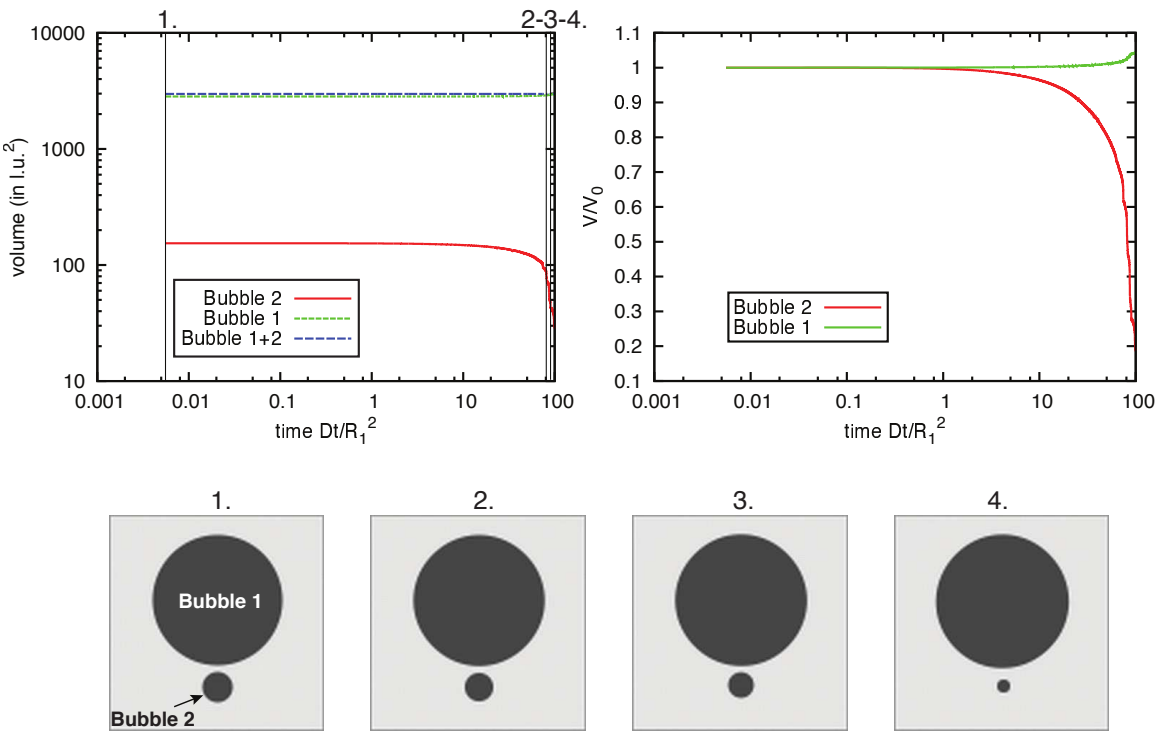

Figure 4.5: (a) Volume of each bubble during the mass exchange caused by Ostwald ripening between two bubbles (see evolution below). Panel (b) Normalized volume change for each of the bubbles as function of time.

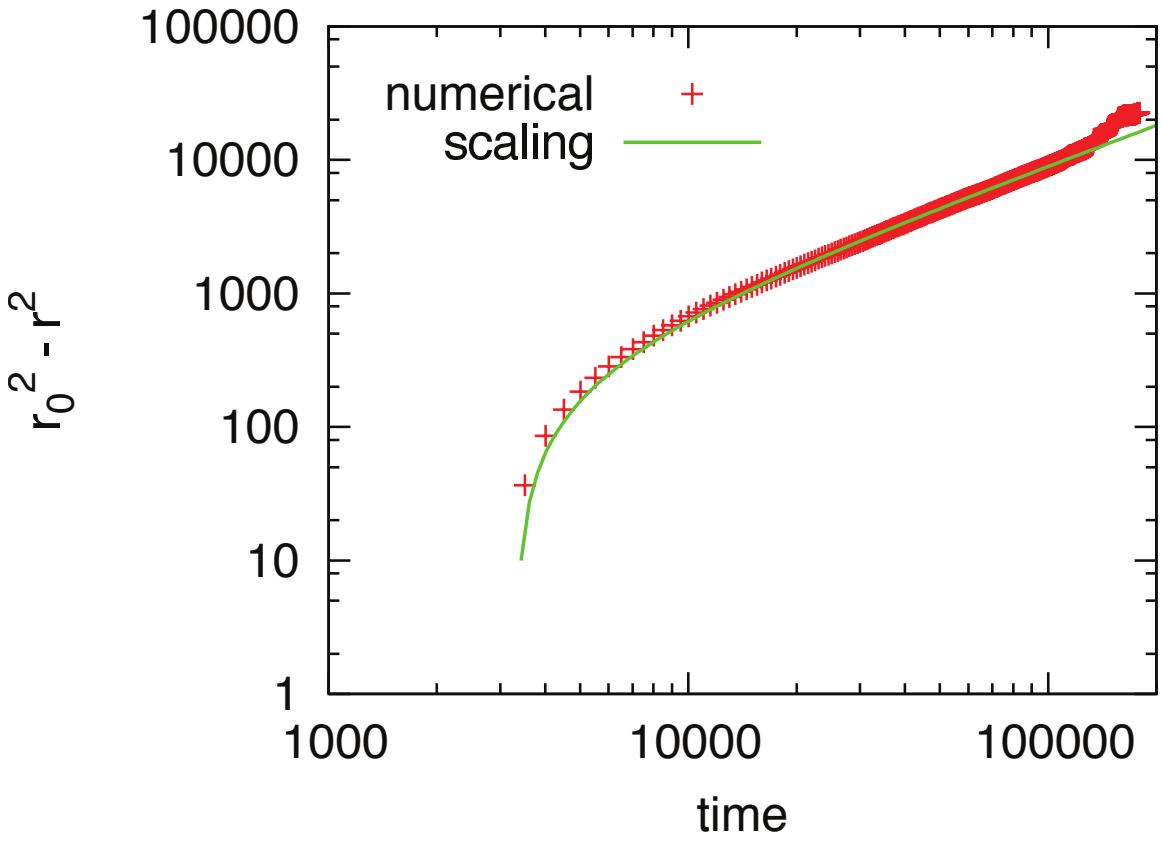

Figure 4.6: Comparison between the numerical results for the small bubble radius change with time. The early trend is in good agreement with a parabolic law, as expected. See the text for more details.

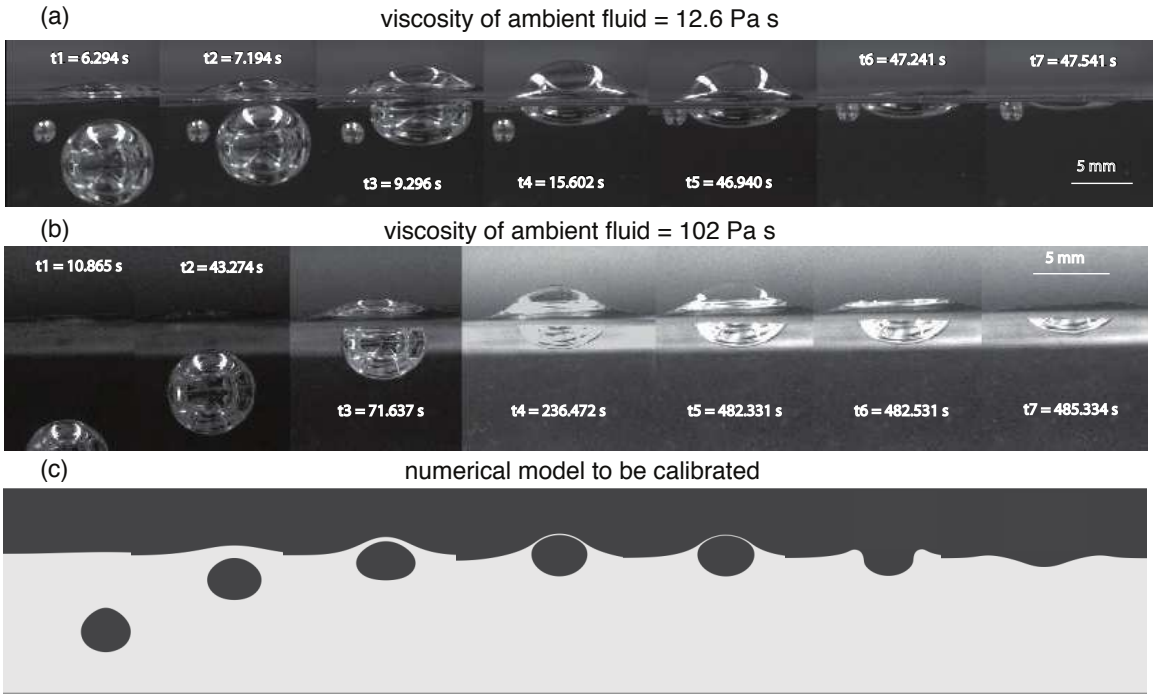

Figure 4.7: Examples of sequences of photographs taken during the bubble rise and film drainage in two experiments and comparison with my numerical results.

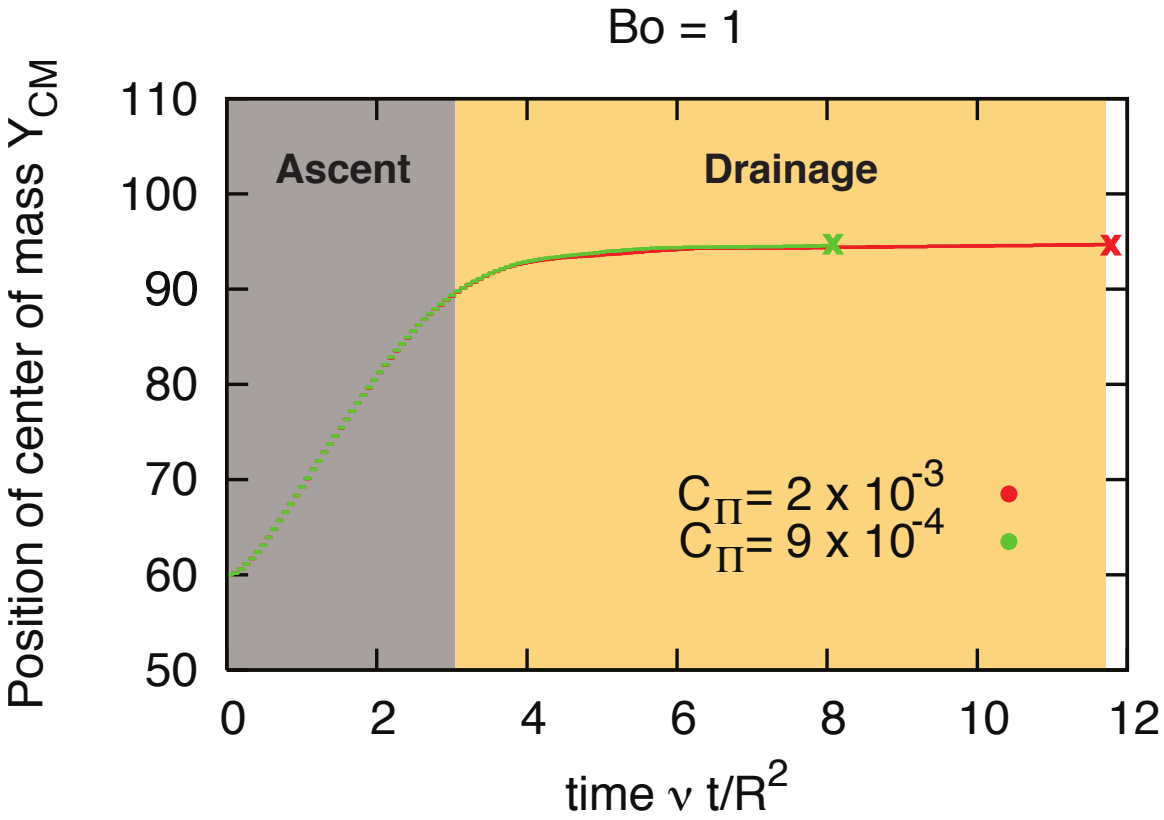

Figure 4.8: Vertical position of the bubble center of mass as function of time for Bo=1 and two different choices of disjoining pressure constant c_Π. The longetivity of the bubble increases with c_Π.

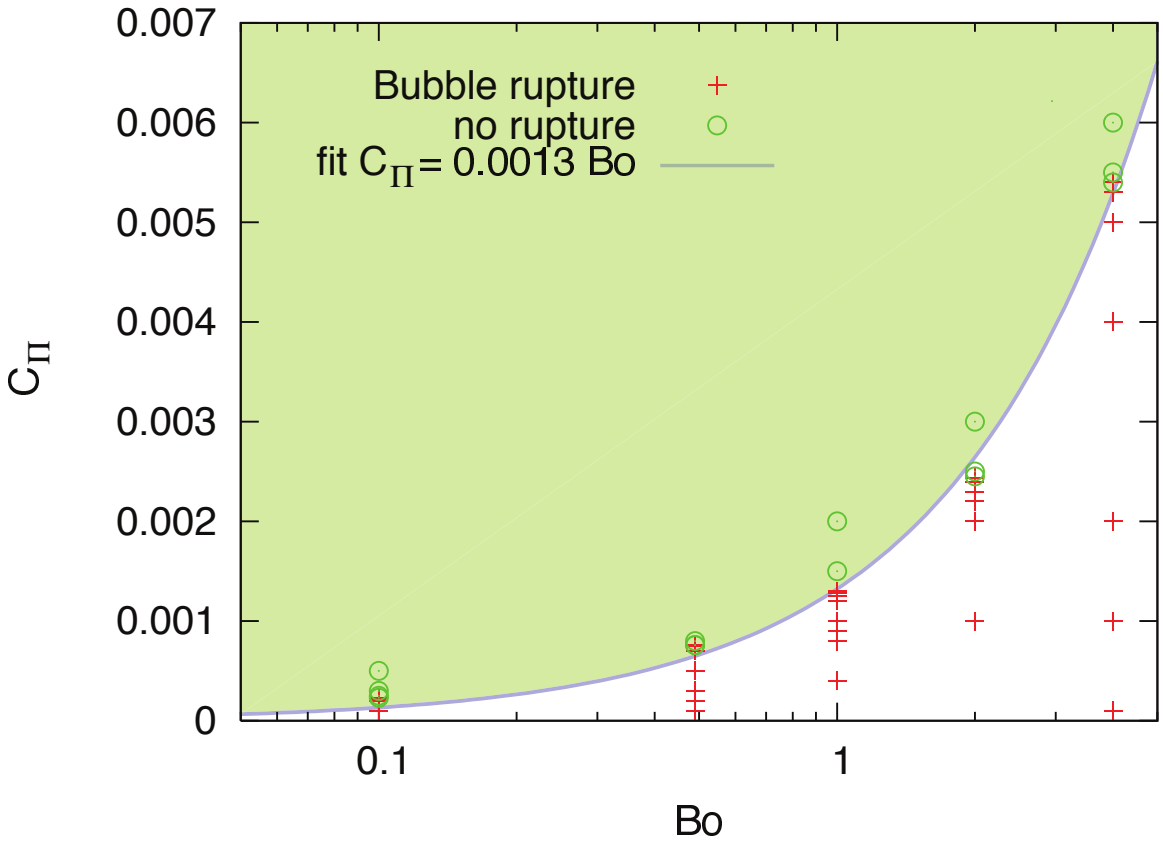

Figure 4.9: Regime diagram that shows how increasing disjoining pressures retard or sometimes prevent bubble rupture. All calculations presented here were run for a maximum of 200,000 iterations.

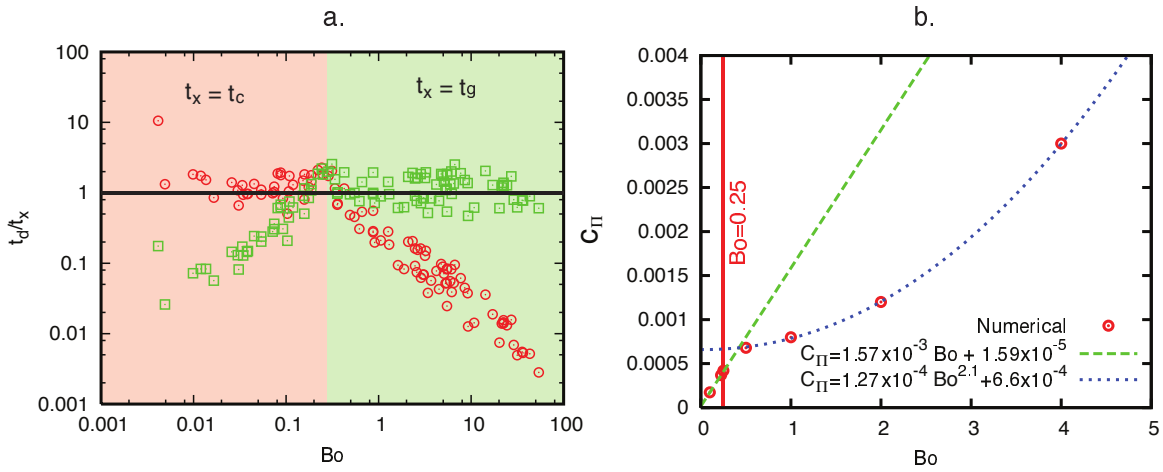

Figure 4.10: Functional form of the experimentally calibrated disjoining pressure - Bond number function. At Bo < 0.25 the trend is linear, it becomes non-linear above 0.25. See the text for a more detailed discussion.

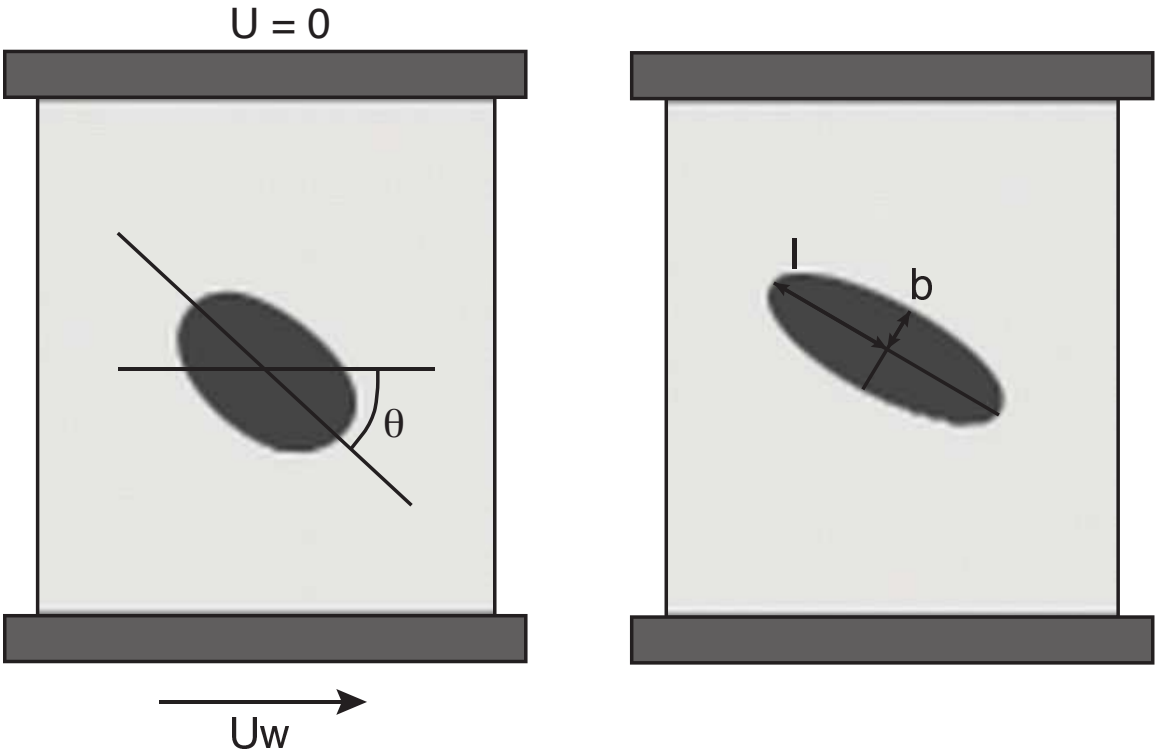

Figure 4.11: Illustration of the measurments used to characterize the bubble final orientation and shape. The actual bubbles shown here come from two calculations with Ca = 0.2 (left) and 0.5 (right).

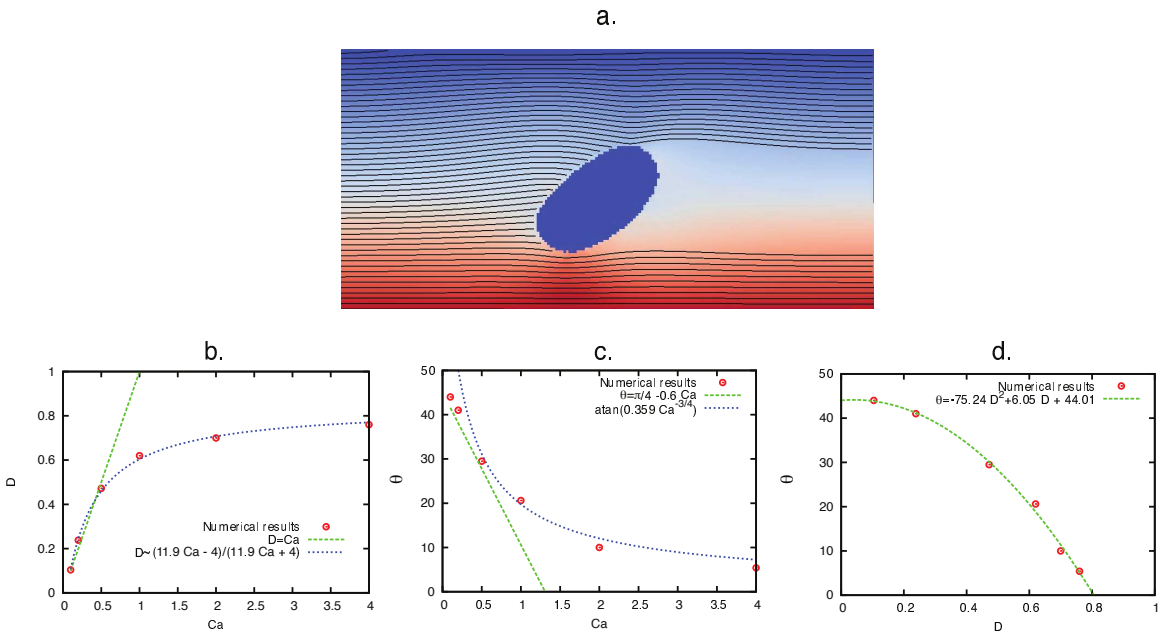

Figure 4.12: (a) Deformation of streamlines by the bubble (Ca = 0.5). (b) Results for the steady bubble shape D as function of Ca in my simple shear calculations. The dashed lines represent the theoretical trends and match closely the experimental results of Rust and Manga. (c) Same for θ and (d) for the correlation between the bubble's orientation and elongation.

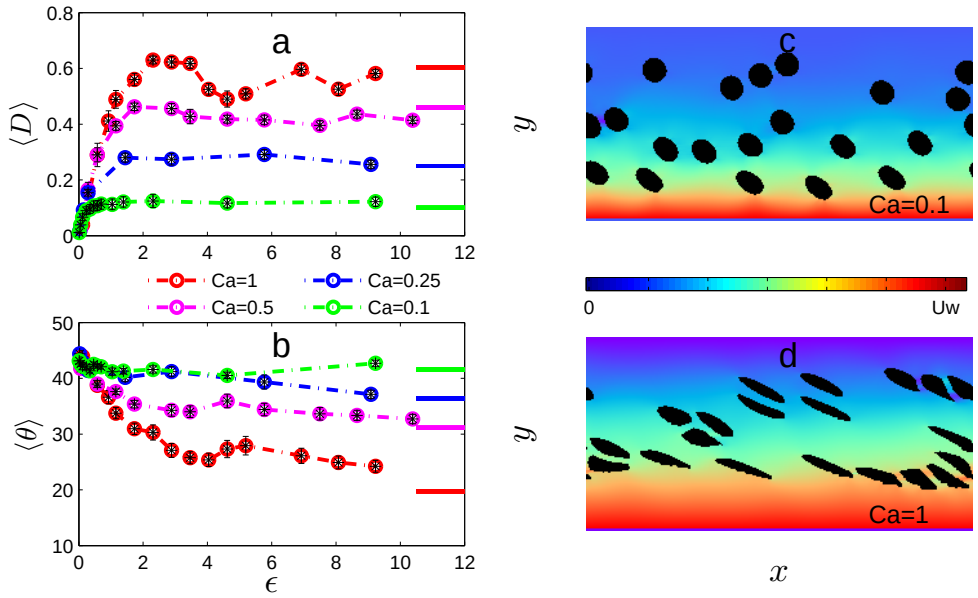

Figure 4.13: (a) Evolution of average deformation $\langle D \rangle_m$ of bubbles with strain accumulations under four different Ca (0.1, 0.25, 0.5, 1).(b) Evolution of average orientation $\langle \theta \rangle_m$ of bubbles under the same Ca numbers as (a). Standard errors for each data points are also given in (a–b). The solid lines at the right side mark the steady-state $\langle D \rangle_m$ and $\langle \theta \rangle_m$ theoretical values for single bubble at specific Ca number. (c) Snapshot of muti-bubbles distribution and the ambient melt velocity field around bubbles for Ca = 0.1 at $\dot{\epsilon} \approx 6.923$. (d) Same as (c) except for Ca = 1 at $\dot{\epsilon} \approx 6.923$. The wall velocity $\frac{U_w H}{\nu} = 0.0011731$ for Ca = 0.1, and $\frac{U_w H}{\nu} = 0.011731$ for Ca = 0.1.

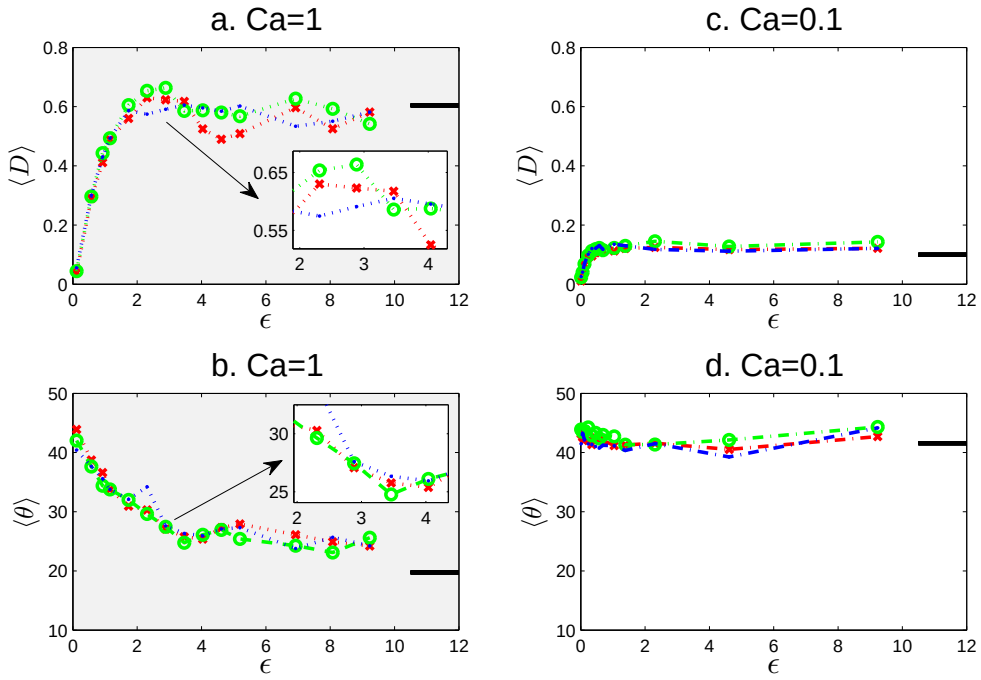

Figure 4.14: Evolution of average bubble shapes $\langle D \rangle_m$ and average bubble inclination angles $\langle \theta \rangle_m$ vs. accumulated strain $\dot{\epsilon}$ with Ca = 1 (a,b) and Ca = 0.1 (c,d). The black solid lines at the right side mark their corresponding theoretical values for single bubble. In each panel, data points of different runs are marked by 'x' in red, 'o' in green and '.' in blue.

CHAPTER V

OTHER TOPICS

Over the previous chapters, the focus was on the chemical and dynamical coupling between bubbles and melts. I have also worked on other topics over the course of my Ph.D. study. This chapter discusses an example of this additional work. I present a study of the dynamical response of saturated porous media to transient stresses using a pore-scale modeling approach. Four different porous media topologies are used to study how they respond dynamically to transient pore-pressure forcing. This chapter represents the work that I co-authored published in Ref. [75]. My contribution to this work was running the lattice Boltzmann model for the various geometries and analyzing the dynamical permeability simulation outputs.

5.1 Dynamic response of saturated porous media to transient stresses

5.1.1 Introduction

The Earth's crust is porous and heterogeneous over a wide range of length-scales [83]. In the upper few kilometers, the pore space is generally saturated with aqueous fluids that play a significant role in water-rock chemical reactions. Pore fluids also affect the physical properties of the heterogeneous medium. One of the most important properties for mass and heat transport is the permeability of the matrix to the flow of fluids. Besides long-term changes in permeability associated with chemical reactions and pore clogging, the response to rapid stress transients (dynamic stresses) can also significantly affect the effective permeability of saturated porous media because of poroelastic effects [14–16, 194].

Biot [14, 15] developed the first theoretical model of the propagation of acoustic waves in saturated porous media in the mid 1950s. Biot found two independent solutions to the propagation of acoustic waves in porous media that he referred to as waves of the first and second kind. For both types of waves, the net drag force exerted by the solid matrix on the fluid controls the dissipation of mechanical energy and by extension the attenuation of

the propagating waves. At low frequency, the wave of the second kind, sometimes referred to as Biot Slow wave, consists of pressure transport by diffusion (darcy transport) and can lead to larger attenuation over the seismic frequency band [151]. An important concept that emerged from the work of Biot is that the drag force that couples the fluid to the solid matrix is frequency dependent and can be represented as a dynamic correction on the effective fluid viscosity.

Following the seminal work of Biot, several groups studied the discharge of pore fluids subjected to harmonic pressure forcing and found, in agreement with Biot's analysis, the effective permeability of the medium to be frequency-dependent and complex valued at high frequency ($\pi/2$ phase lag between the forcing and the discharge) [12, 16, 85, 181]. The frequency-dependent permeability is often referred to as the dynamic permeability of a medium. The JKD dynamic permeability model offered the first scaling relationship to model the frequency-dependence of permeability [85]. It relies on a single free parameter, the rollover frequency ω_c, which depends on fluid and matrix properties. This critical frequency represents the transition from viscous to inertia-dominated momentum balance in a homogeneous porous medium (order of kHz or higher for water saturated sandstones) [151]. Later, the model was verified experimentally and numerically using simple geometries. Additionally, Smeulders et al. [181] provided a more rigorous mathematical validation of the model using standard homogenization methods.

For the most part, pore-scale calculations have been limited to simple and highly symmetric geometries because of computational limitations. Numerical results showed a good agreement with the existence of a single scaling function (related to the critical frequency) that was assumed in Ref. [85]. Recently, a pore-scale study using a lattice Boltzmann flow solver was able to extend the range of validation to more realistic geometries [147]. Their study actually solved for the dynamic permeability with a different problem setup. The porous medium is periodic and therefore infinite (no boundary conditions), the flow is buoyancy-driven and the forcing is homogeneous and applied through a transient harmonic perturbation of the bulk force responsible for the flow. In this study, I use a lattice Boltzmann pore-scale flow model to investigate different porous media topologies and their

effect on the dynamic permeability and verify the scaling of the JKD model. Each domain has finite dimensions and the flow is pressure-driven. The dynamic forcing is introduced by an imposed pore pressure oscillation at one of the boundary. Although the difference in these two models is subtle, the choice of setup can lead to significantly different outcomes, and the effect of finite domains and pressure boundary conditions need to be studied. I observe that the dynamic permeability response is generally in good agreement with the scaling proposed by Johnson et al. [85] and Smeulders et al. [181]. I discuss these results in analogy to well-known properties of electric circuit involving a resistor and a capacitor in parallel (Debye relaxation).

In specific cases, however, I observe a significant departure from the JKD (or Debye relaxation) model. In particular, I observe features that suggest a resonance behavior which is not consistent with the theory of Johnson et al. [85] and Smeulders et al. [181]. I propose two alternative explanations for the existence of resonance. First, using a continuum scale argument, I discuss the importance of a correction term to Darcy's law for transient flows that allows one to derive an hyperbolic version of the mass conservation equation. I show that this new mass conservation equation converges to the standard parabolic diffusion of pore pressure at low frequency, but allows the propagation of damped waves and resonance at high frequency. Although this continuum-scale model offers a satisfying framework to explain the occurrence of resonance in one medium, it fails to explain the lack of resonance in the three other media. Alternatively, I suggest that pore-scale effects, such as different pore-size distributions (PSD) can facilitate pore pressure excitation between heterogeneous flow pathways in response to forced pore-pressure excitations.

5.1.2 Background

Biot [16] introduced a model for the propagation of acoustic waves in saturated porous media by computing the net drag force between the fluid and an oscillating matrix under simplified geometry such as poiseuille and duct flows. He showed that the drag associated with harmonic forcing leads to an effective fluid viscosity that can become complex and that displays a frequency-dependence. It is important to note that Biot's approach was

conducted at the pore-scale and used an unsteady version of Stokes equation for the flow in the limit of a compressible fluid. The momentum equation represented therefore a balance between three terms, inertia, pressure and viscous stresses.

Johnson et al. [85] and Smeulders et al. [181] showed that by matching inertial forces associated with the transient forcing with viscous forces a critical frequency emerges

$$\omega_c = \frac{\eta}{\rho_f k_0 \alpha_\infty} \tag{5.1}$$

where η is the dynamic viscosity of the pore fluid, ρ_f its density, k_0 the static permeability, ϕ the porosity of the medium and lastly α_∞ is the dynamic tortuosity at infinite frequency of the medium which is related to the formation factor $F = \phi/\alpha_\infty$ [85].

The ratio of the forcing frequency ω to ω_c controls the dynamic response of saturated (homogeneous) porous media to transient pore pressure forcing. It is important to note that, in isotropic homogeneous media, the effect of the microstructure of the porous medium only emerges through three independent scalar parameters, the static ($\omega \to 0$) permeability, the porosity and the formation factor of the medium. As discussed by Pride et al. [151], once corrected for the dynamic permeability response, using mass conservation, the partial differential equation that describes the evolution of the pore pressure is a diffusion equation and therefore is parabolic and dissipative. I therefore expect that the forced pressure oscillations decay with time as expected from a diffusion equation.

5.1.3 Methods

5.1.4 Computation of the formation factor

I constructed four porous media synthetically, either by using a stochastic algorithm of crystal nucleation and growth following the method described by [70] (textures referred to as Rectangles and Spheres) or creating void space with simple geometrical shapes (e.g., spheres, tubes and wave-looking tubes). Fig. 5.1 shows the pore structure of the four media.

The formation factor of a heterogeneous medium is defined as the effective electric conductivity of the medium normalized to that of the pore-filling fluid assuming the solid matrix is a perfect insulator. I use the analogy between the steady-state solution of the

(heat) diffusion equation and the solution to poisson's equation for the electric potential in heterogeneous media.

I apply a 3-D lattice Boltzmann model for heat conduction in porous media. In the lattice Boltzmann method, the diffusion equation is modeled following a statistical approach it is replaced by a discrete version of Boltzmann's equation. Boltzmann's equation describes the evolution of particle probability functions $g(\mathbf{x}, \mathbf{v}, t)$ that represent the probability of finding a particle at position $\mathbf{x}$, traveling with velocity $\mathbf{v}$ at time t. Particles stream through the domain and collide with each other, which leads to the following equation for the evolution of the g_is

$$g_i(\mathbf{x} + \mathbf{e}_i dt, t + dt) = g_i(\mathbf{x}, t) - \frac{1}{\tau_h}\left[g_i(\mathbf{x}, t) - g_i^0(\mathbf{x}, t)\right] \tag{5.2}$$

where it is assumed that the collision operator reduces to a single relaxation time [13]. The index i refers the discrete set of possible trajectories $\mathbf{e}_i$ on the lattice (nearest neighbors), τ_h is the relaxation time (related to the thermal diffusivity) and g_i^0 are the local equilibrium particle probability distribution functions. The macroscopic field of interest, here temperature $T(\mathbf{x}, t)$, is obtained by summing the local distribution functions

$$T(\mathbf{x}, t) = \sum_i g_i(\mathbf{x}, t). \tag{5.3}$$

The equilibrium distributions are linearly dependent on the local temperature

$$g_i^0(\mathbf{x}, t) = t_i T(\mathbf{x}, t) \tag{5.4}$$

where t_i are lattice weights, which in my model with 7 discrete velocity e_i are $t_0 = 1/4$, $t_{1-6} = 1/8$ (see Fig. 5.2).

This method has been shown to recover the diffusion equation, in 3-D, and allows for a simple treatment of the internal solid-fluid boundaries (no heat flux). This is done with the bounceback rule that specifies that distributions are reflected on solid obstacles

$$g_i(\mathbf{x}, t) = g_{\bar{i}}(\mathbf{x}, t) \qquad \mathbf{x} \in \text{Solid} \tag{5.5}$$

where the overbar denotes the velocity direction opposite to i, in other words, the distributions are all reflected backwards when they encounter a solid node in the physical

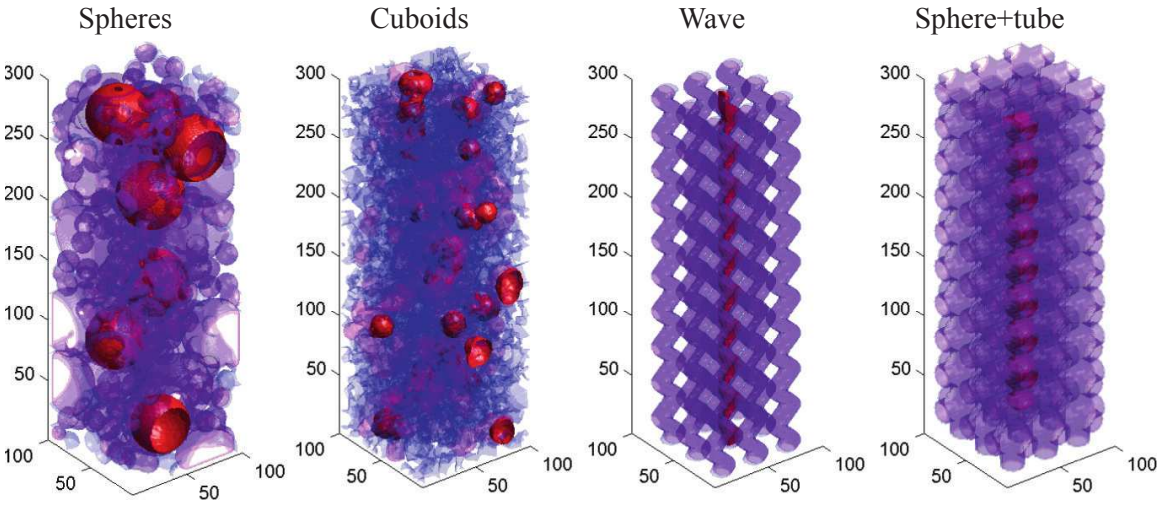

Figure 5.1: Pore-scale representation of the four porous media. Warm colors (red) show larger pores. All texture are synthetically constructed, Spheres and Rectangles are constructed with a stochastic nucleation and growth algorithm following the procedure described by Hersum and Marsh [70].

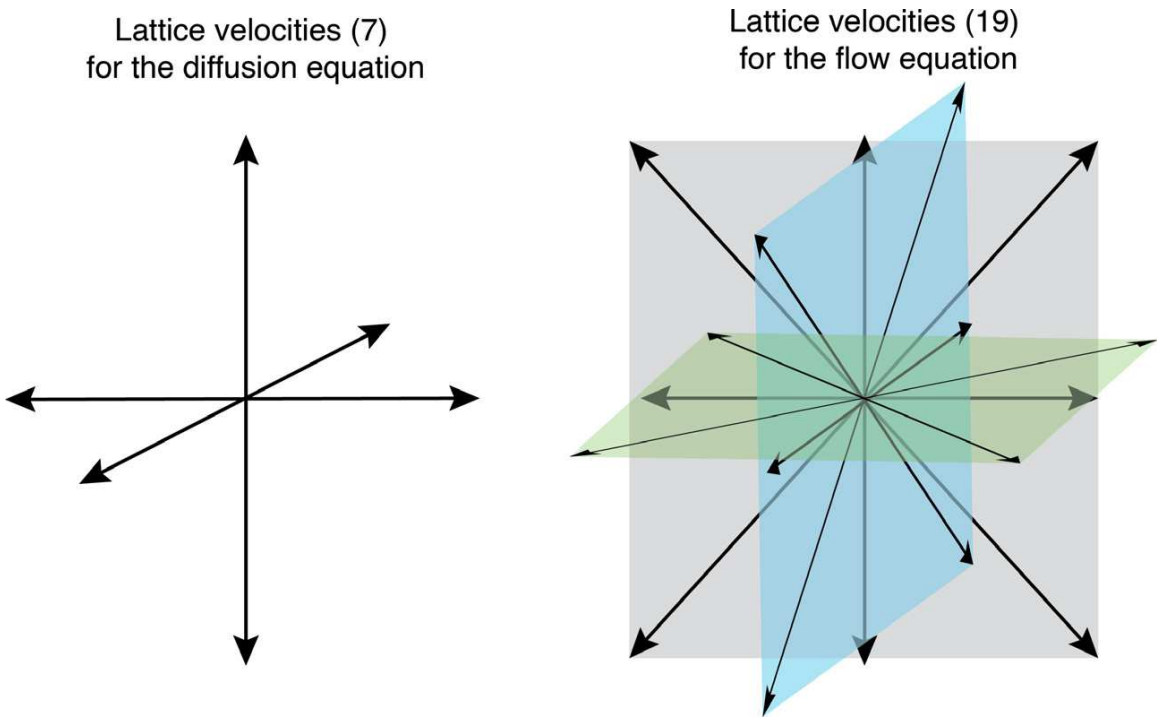

Figure 5.2: Diagram showing the velocity discretization used for the lattice Boltzmann modeling. On the left the 7 velocities $\mathbf{e}_i$ (including a rest velocity $\mathbf{e}_0$) model for the calculation of the formation factor is shown. On the right the 19 velocity model c_i used for the flow calculations at the pore-scale is illustrated.

domain [79, 80]. In these calculations, the temperature at the inlet ($z = 0$) and outlet ($z = L_z$) are fixed to 1 and 0 respectively. The calculations are run until a steady-state is reached. For more information about lattice Boltzmann models for the diffusion equation, the reader is referred to Ref. [213].

5.1.4.1 Lattice Boltzmann model for fluid flow

My pore-scale flow simulations are also based on the lattice Boltzmann method. I use the Palabos open source library (`www.palabos.org`), to compute the 3-D flow field at the pore scale in each medium. Similarly to the calculations of the formation factor discussed above, I compute the evolution of particle probability density functions $f(\mathbf{x}, \mathbf{v}, t)$ subjected to streaming (free flow) and collisions with other particles or boundaries where mass and momentum are conserved locally. The discretized form of the evolution equation for $f(\mathbf{x}, \mathbf{v}, t)$ is similar as well

$$f_i(\mathbf{x} + \mathbf{c}_i dt, t + dt) = f_i(\mathbf{x}, t) - \frac{1}{\tau_f}\left[f_i(\mathbf{x}, t) - f_i^0(\mathbf{x}, t)\right] \tag{5.6}$$

where τ_f is the relaxation time to the local equilibrium distribution functions f_i^0 and i is an index that discretizes the space of available trajectories for particles. Because of the four scalar fields that are conserved locally (one for mass and three for momentum), the particle motion is now limited to 19 directions, see Fig. 5.2. After assigning the first statistical moments of the particle probability distribution functions f_i to conserved macroscopic quantities such as local density and momentum

$$\rho(\mathbf{x}, t) = \sum_i f_i(\mathbf{x}, t), \quad \rho u(\mathbf{x}, t) = \sum_i \mathbf{c}_i f_i(\mathbf{x}, t), \tag{5.7}$$

a multiscale expansion yields a compressible version of Navier-Stokes equations [47, 48, 71]. In the expansion, the kinematic viscosity of the fluid v is identified with

$$v = \frac{\eta}{\rho} = c_s^2 dt \left(\tau_f - \frac{1}{2}\right) \tag{5.8}$$

where c_s^2 is a constant that depends on the choice of spatial discretization (1/3 here). In each calculation, pressure boundary conditions are applied at $z = 0$ and $z = L_z$. In a first

stage, steady boundary conditions are applied to obtain a steady discharge through the medium. It allows one to calculate the static permeability

$$k_0 = \frac{\eta L_z q_0}{\Delta p^0} \tag{5.9}$$

where Δp^0 is that steady pressure drop imposed on the medium and the discharge is computed with

$$q_0 = \frac{1}{V}\int_V \mathbf{v}(\mathbf{x}) \cdot \mathbf{n}_z dx^3 \tag{5.10}$$

with $\mathbf{v}(\mathbf{x})$ is the steady-state pore-scale velocity field and $\mathbf{n}_z$ the direction along the pressure gradient. After reaching a steady discharge, the outlet pressure is varied harmonically around its static value P^0_{out}

$$P_{\text{out}}(t) = P(L_z, t) = P^0_{\text{out}} + \Delta p \sin(\omega t). \tag{5.11}$$

I compute the flow field and therefore calculate the discharge with a high temporal resolution during many pressure cycles to calculate the dynamic permeability. The amplitude of the pressure fluctuations and gradients are small enough that compressibility effect remain limited in my lattice Boltzmann simulations.

5.1.4.2 Post-processing of transient discharge data

In response to the dynamic pore pressure condition, the flux q_{out} becomes

$$q_{\text{out}} = q^0_{\text{out}} + \Delta q \sin(\omega t - \varphi), \tag{5.12}$$

when the system reaches a quasi-steady state. φ is the phase lag between the flux and the imposed pressure oscillations. I fit the outlet discharge with a sine function $A\sin(\omega t + B) + C$ to obtain the amplitude Δq and the phase φ. The dynamic permeability $k(\omega)$ is calculated as,

$$k(\omega) = \frac{\eta \Delta q(\omega)}{\Delta p(\omega)/L_z}. \tag{5.13}$$

By conducting simulations over a wide range of frequency, I can establish the spectral response of each medium to the pressure oscillations.

5.1.5 Results

5.1.5.1 Expected dynamical response

I selected four porous media structures to provide a test to the predicted self-similar nature of the dynamic response of the permeability in terms of frequency [85, 181]. These textures range from about 30 to 60% porosity, the formation factors vary by a factor of 3 and the static permeability by a factor of 6. It is interesting to note that the JKD model for the dynamic permeability only depends on these three factors. I am also interested, within the limits of the number of porous media structures tested here, to investigate whether the pore-size distribution (PSD) can affect the dynamical response independently from these three parameters.

The pore-size distribution for each medium is computed with the model of Yang et al. [218], where in each pore, the largest sphere that can be fully included into the volume of the pore defines its effective radius (pore size). The results of these PSD calculations are shown in Fig. 5.3. I note that the range of pore-sizes for Rectangles, Spheres-Tubes and Wave are comparable, but that Spheres displays a significantly greater range of pore sizes with several pores with radius > 20 grid units.

The formation factors are computed according to Sec. 5.1.4, where a 3-D diffusion model is relaxed to steady-state. An example of steady-state temperature distribution in the Rectangles texture is shown in Fig. 5.4 for reference and the results are listed in Tab. 5.1. For each porous medium, I conducted between 15 and 20 simulations with different forcing frequencies to obtain the effective permeability of the medium over a range of frequency that extends over three orders of magnitude.

In Fig. 5.5a, I show the un-normalized results for three of the four media. I can clearly observe similar trends with a sudden decay of effective permeability as the forcing frequency approaches the critical frequency of each medium ω_c (see vertical lines). Once the frequency is normalized with ω_c (Fig. 5.5b) the data collapses as expected for the self-similar trend observed and documented by several authors [85, 125, 147, 176, 181]. I find an excellent agreement with the theory developed by Johnson et al. [85] and Smeulders et al. [181] irrespective to the PSD of the medium. The complex nature of the dynamic permeability is

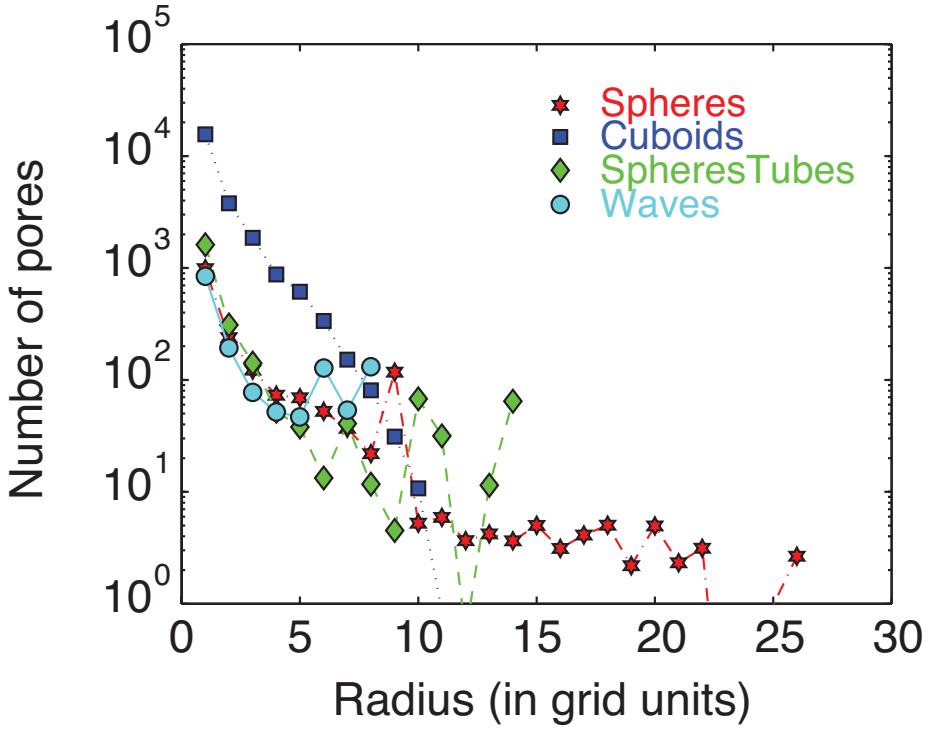

Figure 5.3: Pore-size distribution for the four media calculated from the model of Yang et al. [218]. In this model, the radius of each pore is determined by the largest sphere that can be fully included into the pore.

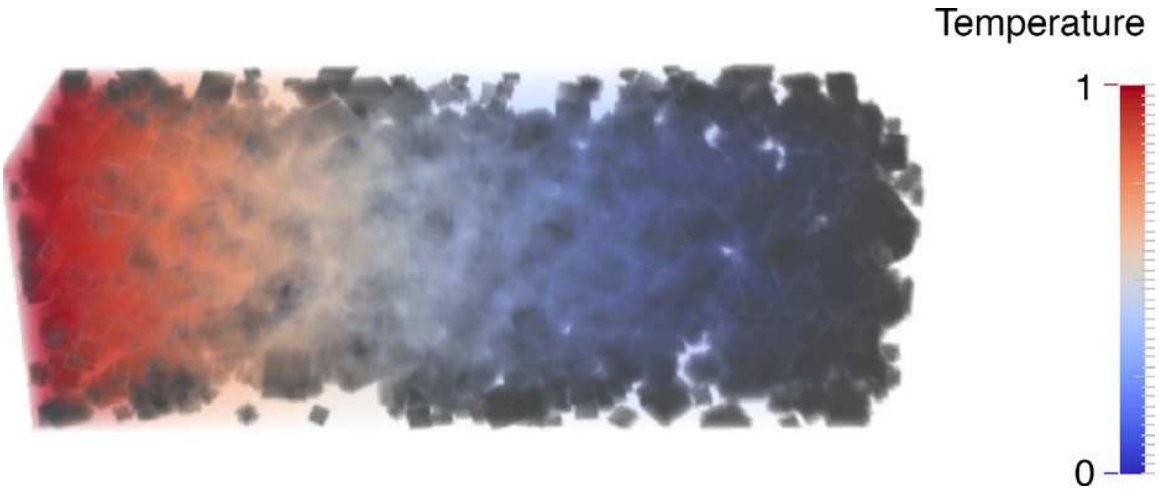

Figure 5.4: Thermal field in the porous medium (Rectangles) at steady-state. Here the solid fraction is assumed as a perfect insulator. The formation factor is computed from the effective thermal conductivity of the medium at steady-state.

better portrayed by the phase lag between the harmonic pressure forcing and the computed discharge (Fig. 5.6) and again show an excellent agreement with previous studies [85, 125, 147, 176, 181].

5.1.5.2 Anomalous behavior

I conducted the same simulations on the last porous medium (Spheres) and obtained a significantly different result. The work remains preliminary, however the runs were checked for reproducibility and the results are robust. The dynamic response of the permeability and phase lag with the harmonic forcing are similar to what I observe for the other media except for the existence of a peak at high frequency $\omega > \omega_c$ (see Figs. 5.7 and 5.8). The phase lag displays an excursion to negative phases (or in that context positive phase with $\varphi > \pi$ to satisfy causality) that coincides with the resonant permeability peak. I note that, although not shown here, I observed a similar behavior in another medium that displayed sharp heterogeneities at the pore-scale.

The existence of a permeability peak at high frequency is unexpected from the existing theory and suggests a resonance-like behavior over a narrow range of forcing frequencies. It is important to realize that neither Darcy's equation, even corrected for frequency-dependent permeability, nor the groundwater flow equation (diffusion) can cause a resonance-like behavior. Resonance occurs generally as a response to transient forcing of hyperbolic partial differential equations. In the discussion section, I present an analogy between the standard JKD theory for the dynamic permeability and electric circuits and show that this theory fails to explain the peak observed in Fig. 5.9. I discuss two possible causes for the peak in dynamic permeability: the resonance is governed by the dynamics at the continuum scale (modified Darcy flux) or by micro-structural properties.

5.1.6 Discussion

5.1.6.1 Analogy of Debye relaxation

The linear theory of flow in porous media is often compared to linear electric circuit theory because of the many analogies between the two fields. First, Ohm's law is equivalent to Darcy's law with the hydraulic conductivity replacing the electrical conductivity and

Table 5.1: Summary of the steady flow calculations.

Name	Porosity ϕ	Formation factor F	Permeability k_0 (dimensionless)	JKD critical frequency ω_c
Spheres+tubes	0.49	0.3	2.98	6.2×10^{-4}
Waves	0.21	0.11	0.48	1.4×10^{-3}
Spheres	0.61	0.15	0.89	1.05×10^{-3}
Rectangles	0.61	0.39	1.16	2.04×10^{-3}

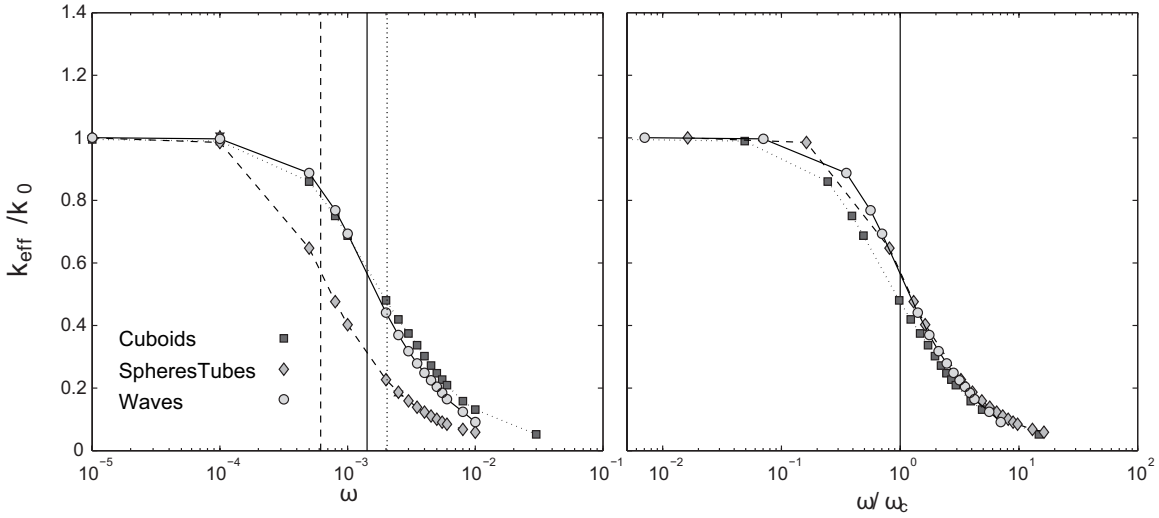

Figure 5.5: Effective (dynamic) permeability as function of frequency for three of the four porous media used in this study. Left panel shows how differences in porosity, static permeability k_0 and formation factor influence the response. The right panel shows that the rollover frequency ω_c provides a satisfying normalization factor to observe a self-similar behavior between the different media.

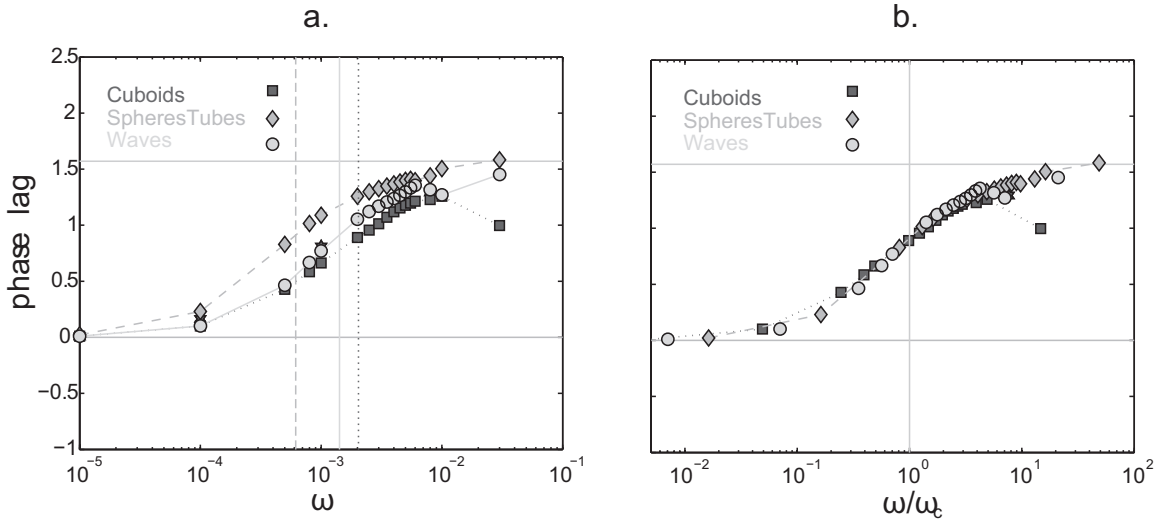

Figure 5.6: The phase lag φ between the pore pressure forcing at the outlet and the discharge in the porous medium as function of frequency (left) and normalized frequency (right). The results are consistent with previous studies.

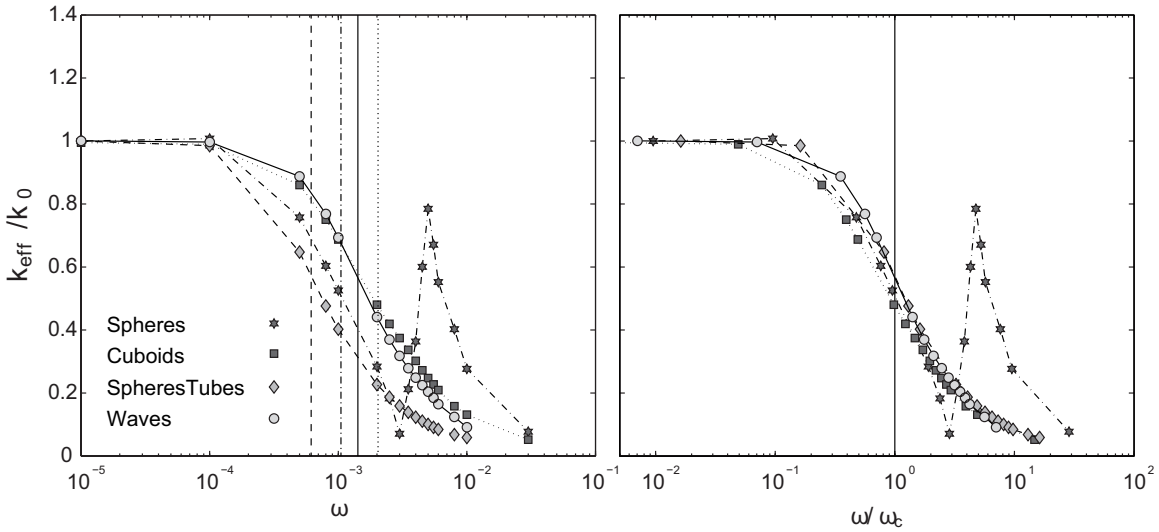

Figure 5.7: Same as Fig. 5.5 but with the last porous medium (Spheres). Note that the medium referred to as Spheres has the broadest pore-size distribution.

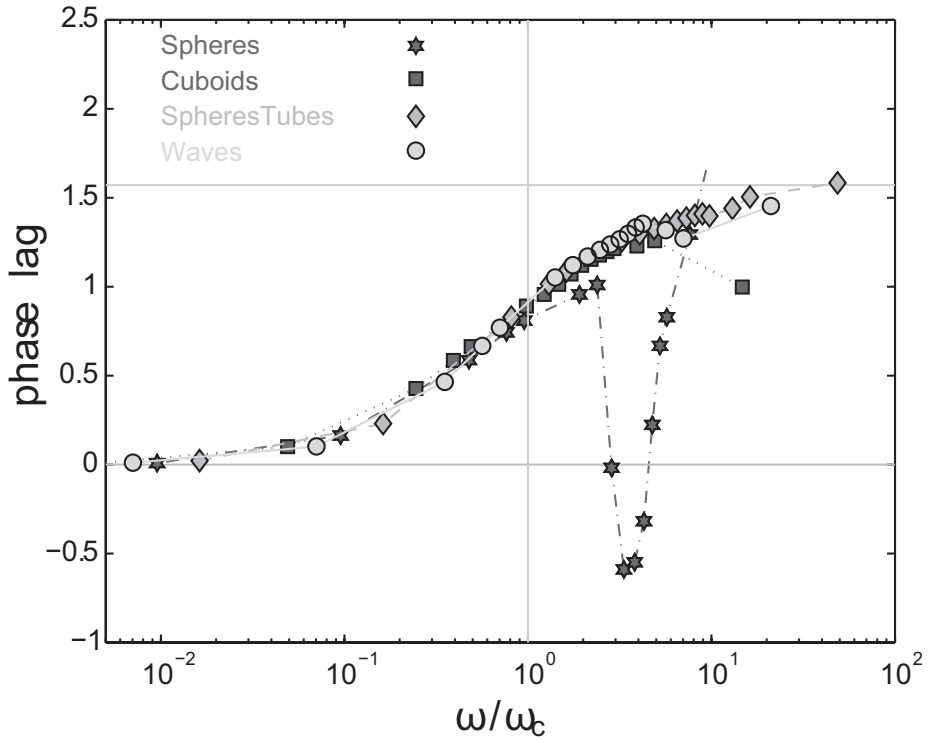

Figure 5.8: Phase lag between the pore pressure fluctuations and the discharge as function of normalized frequency for all media.

the head potential (or pseudo-potential) as defined by Hubbert [74] replacing the electrical potential. It is therefore natural to yield analogies between the dynamic permeability model presented by Johnson et al. [85] and complemented by Smeulders et al. [181] and the spectral response of electric circuits. The two equations that define the dynamic permeability and the dynamic tortuosity in the JKD model, once written in the frequency domain, are reminiscent to Ohm's law and the dynamical response of a capacitor respectively

$$\begin{aligned} \mathbf{v} &= -\frac{k(\omega)}{\eta\varphi}\nabla p \\ -i\omega\rho_f\alpha(\omega)\mathbf{v} &= -\nabla p. \end{aligned} \tag{5.14}$$

The second equation highlights the importance of inertia and shows that a phase lag exists at high frequency between the discharge $\phi\mathbf{v}$ and the pressure forcing. The $\pi/2$ phase between the current and the potential introduced by inertia is reminiscent of the effect of adding a capacitor to an electric circuit. If a resistor is set in parallel with a capacitor (see Fig. 5.9), the relative importance of the resistor and capacitor on the impedance of the circuit will be controlled by the imposed frequency and a Debye relaxation similar to the dynamical response of the permeability is obtained.

The transition from creep to inertia dominated momentum dissipation in porous media is therefore similar to the response of a parallel RC circuit. I can even push the analogy further and use it to estimate the frequency at which I expect the transition to occur. The Debye frequency is obtained by matching the Imaginary part of the capacitor impedance to that of the resistor

$$\begin{aligned} \mathrm{Im}(Z_c) &= Z_R \\ \frac{1}{\omega C} &= R \end{aligned} \tag{5.15}$$

and hence $\omega_D = 1/RC$. By analogy, the resistance in the dynamic version of Darcy's law is

$$Z_R = \frac{\eta\phi}{k(\omega)}, \tag{5.16}$$

while, using Eq. 5.14, the inertia associated with the capacitor can be defined as

$$\mathrm{Im}(Z_c) = \omega\rho_f\alpha(\omega). \tag{5.17}$$

Matching the two impedance allows one to retrieve the general form of the critical frequency of the JKD model

$$\omega_c = \frac{\eta\phi}{\rho_f \alpha_\infty k_0}. \tag{5.18}$$

This analogy is useful because it also provides some clues as to what is problematic with the results that display resonance-like features.

5.1.6.2 Resonance and the importance of hyperbolic effects

One of the limitations of Darcy's law is that it represents a continuum approximation of a steady-state flow through a porous medium. The justification for using a time-independent momentum closure equation is that the Reynolds number that characterizes the flow is $\ll 1$. Interestingly, regardless of this approximation, one can still derive a time-dependent mass conservation equation (a simple form of the groundwater flow equation) from Darcy's law that describes the pressure or head distribution in time and space in the porous medium

$$\frac{1}{K_f}\frac{\partial p}{\partial t} = -\frac{k}{\eta}\frac{\partial^2 p}{\partial x^2} \tag{5.19}$$

where for simplicity the flow is assumed perpendicular to gravity, the permeability is homogeneous and K_f refers to the fluid's bulk modulus. To be consistent with the theory developed by Johnson et al. [85] and Smeulders et al. [181], the solid matrix is viewed as incompressible for the sake of this argument. Eq. 5.19 is a diffusion equation with the hydraulic diffusivity $D_h = K_f k/\eta$. The diffusion equation is parabolic and, consequently, the pore pressure can propagate at an infinite speed from the boundaries inside the domain. Consider an initial Dirac delta function of elevated pore pressure centered at $\mathbf{x} = 0$ at $t = 0$. At any $t = dt$, for any small dt, the pressure profile that results from Eq. 5.19 will have finite (non-zero) pressure values except at $x \to \pm\infty$. The propagation of pressure is therefore instantaneous.

In reality, I know that it will take a finite time for pressure to propagate a finite distance in a porous medium. It is therefore necessary to introduce a transient term to modify Darcy's equation (even in the frequency domain, but I will restrict the analysis to the time domain here). A similar argument has been developed for heat transfer and the development

of heat waves. Cattaneo [26] and Vernotte [204] arrived independently at the conclusion that a proper account of heat transfer by conduction should include an additional term in Fourier's law to consider that there is a finite time τ for the propagation of heat that depends on material properties. Following the same strategy, I arrive at the following definition for the transient Darcy's equation that satisfy a finite speed of pressure propagation

$$\tau \frac{\partial q}{\partial t} + q = -\frac{k}{\eta} \frac{\partial p}{\partial z} \tag{5.20}$$

where q is the discharge in the z-direction. Although this equation is different from Biot's equations and the equations used by Johnson et al. [85] and Smeulders et al. [181], it is important to note some similarities. First this equation is quite similar to the definition of unsteady Stokes flows and it is therefore not a novel concept. Also, in Biot's model, two separate but coupled equations were used to describe the displacement of each phase (fluid and solid) and Biot used an unsteady Stokes equation for the flow field that is not identical but quite similar to Eq. 5.20. The Cattaneo-Vernotte (CV) term in Eq. 5.20 (time derivative) introduces a phase lag for a finite value of τ, in agreement with the JKD model. The main difference here is that both Darcy's flux and the CV terms are balancing the pressure forcing in Eq. 5.19. The partitioning between the inertial term and the darcian behavior depends on the value of the relaxation time τ and the forcing frequency ω, it is therefore not identical to Eq. 5.14.

The addition of a transient or unsteady term to the flux equation is not entirely novel, it is important to draw attention to its effect on the mass conservation equation. I argue that when Eq. 5.20 is introduced in the continuity equation I retrieve a simple hyperbolic Telegraph equation

$$\frac{\tau}{K_f} \frac{\partial^2 p}{\partial t^2} + \frac{1}{K_f} \frac{\partial p}{\partial t} = \frac{k}{\eta} \frac{\partial^2 p}{\partial x^2}. \tag{5.21}$$

If the relaxation time $\tau \ll 1$, then the parabolic groundwater flow equation is retrieved. One can directly conclude that this hyperbolic equation admits the propagation of damped waves that travel with a finite velocity $c = (K_f F/\rho_f)^{1/2}$, where I identified the relaxation time τ with $\rho_f k_0/\eta = 1/\omega$. This means that my model is consistent to that of JKD where the transition between inertia and viscous dominated regimes occurs around the rollover

frequency ω_c. The adequate boundary conditions with respect to my study are

$$\begin{aligned} p(0,t) &= p_1 \\ p(L_z,t) &= \Delta p^0 + \Delta p \sin(\omega t) \end{aligned} \tag{5.22}$$

where Δp^0 is the static pressure difference across the sample and Δp is the amplitude of the harmonic pressure perturbation. Using sine transforms

$$p(z,t) = \sum_{n=1}^{\infty} S_n(t) \sin(n\pi z/L_z), \tag{5.23}$$

the mass conservation equation unfolds into n second order non-homogeneous ODE

$$\frac{d^2 S_n}{dt^2} + \frac{1}{\tau}\frac{dS_n}{dt} + \frac{n^2\pi^2}{L_z^2}\frac{kK_f}{\eta\tau} S_n = \frac{2n\pi}{L_z^2}\frac{kK_f}{\eta\tau}\left[p(0,t+(-1)^{n+1}p(L_z,t)\right]. \tag{5.24}$$

The homogeneous equations which do not include the harmonic forcing yield solutions

$$S_n^h(t) = A_n \exp\left[-\frac{\gamma}{2}\left(1+\sqrt{1-4\omega_n^2\tau^2}\right)t\right] + B_n \exp\left[-\frac{\gamma}{2}\left(1-\sqrt{1-4\omega_n^2\tau^2}\right)t\right] \tag{5.25}$$

where A_n and B_n are constant that are constrained by the initial and boundary conditions, and the characteristic frequencies $\omega_n = n^2\pi^2 kK_f/\eta L_z^2$ and finally $\gamma = 1/\tau$. These solutions are dissipative (damping) and the damping increases when $\tau \to 0$, which is consistent with the diffusive behavior of the equation in this limit.

Because the harmonic forcing has no influence over the homogeneous solution it is more important to study the particular solution for resonance effects. Because of the harmonic forcing, it is convenient to write the particular solutions as

$$S_n^p(t) = C_n \sin(\omega t) + D_n \cos(\omega t). \tag{5.26}$$

The coefficients C_n and D_n are obtained after inserting Eq. 5.26 into Eq. 5.24

$$\begin{aligned} C_n &= \frac{2(-1)^{n+1}\tau^2\left[(\omega_n')^2-\omega^2\right]\omega_n'}{\omega^2+\tau^2\left[(\omega_n')^2-\omega^2\right]^2} \\ D_n &= \frac{2(-1)^n\tau\omega\omega_n'}{n\pi\left[\omega^2+\tau^2\left[(\omega_n')^2-\omega^2\right]^2\right]} \end{aligned} \tag{5.27}$$

where the characteristic frequency of the medium ω_n' is defined by

$$\omega_n' = \sqrt{\frac{w_n}{\tau}}. \tag{5.28}$$

The overall amplitude the waves associated with the particular solution in response to the forcing at frequency ω is

$$X_n = \sqrt{C_n^2 + D_n^2} = 2\omega_n' \tau \left[\frac{\frac{\omega}{n\pi} - \tau \left[(\omega_n')^2 - \omega^2 \right]}{\omega^2 + \tau^2 \left[(\omega_n')^2 - \omega^2 \right]^2} \right] \tag{5.29}$$

which implies a finite resonance when the forcing frequency ω approaches (but not equals) ω_n'. The actual solution for the resonant frequency requires finding the roots of a fifth order polynomial $f(\omega)$ that also depends on the choice of relaxation time τ and the order of the harmonic considered n. It is beyond the scope of the present work to provide an analysis of this polynomial. It is however instructive to reflect on the amplitude of the particular solution as the forcing approaches resonance $\omega \to \omega_n'$

$$X_n(\omega_n') = \frac{2\tau}{n\pi} \tag{5.30}$$

which shows that the amplitude of high frequency harmonics may become small. Only the lowermost modes may display visible resonance peaks. Moreover, in the limit where $\tau \to 0$, no resonance is observed, which is consistent with the character of the partial differential equation in that limit.

My hyperbolic model for the mass conservation in a porous medium subjected to transient forcing therefore admits a resonant behavior if the relaxation time t becomes important, i.e., when $\omega\tau > 1$. Alternatively, resonance may occur when the forcing frequency approaches $n\pi c/L_z$, where c is the pressure wave propagation speed that depends on the compressibility of the fluid and the formation factor of the medium. There are obviously some simplifying assumptions in this model. For instance, I have assumed that τ was independent of frequency and I use the asymptotic limits for the permeability (k_0) and the dynamic tortuosity to identify what governs the relaxation time using the standard equations for dynamic permeability. I therefore assume that τ is controlled by the physical properties of the porous medium and pore fluid and that it does not depend on the applied forcing. This assumption, although not justified, is consistent with the theory developed for heat wave propagation in heterogeneous media [136, 137, 139].

In the light of this hyperbolic description of the mass balance in porous media, I can estimate the expected range of frequency that should display resonance for the different

porous media. A satisfying model should be able to explain the peak observed with the Spheres topology and be consistent with the absence of resonance observed for the three other media. I first compute ω'_n for $n = 1$ for all media. The actual resonance is not expected to take place exactly at ω'_n, but from a visual inspection of the roots of the polynomial $f(\omega)$ the actual position of the resonance is $\omega'_n < \omega* < 2\omega'_n$. In Fig. 5.10, I compare the set of forcing frequencies tested in my simulations to ω'_n. The approximate range of frequency where the continuum hyperbolic mass balance equation predicts a resonant effect is consistent with my results with the Spheres medium. However, I note that my calculations should have allowed one to observe a resonant peak in each medium. This informs one that while the continuum-scale hyperbolic model may be consistent for one of my medium at high frequency, the lack of resonance in the other media indicates that it is not sufficient to explain my results.

One could argue that the absence of resonance reflects that the amplitude of the particular solution is negligible and that the resonance is therefore difficult to measure. The hyperbolic model is generally consistent with the transient Stokes equation at the base of the theory of linear poroelasticity developed by Biot, however it does not provide a satisfying explanation for my pore-scale simulations.

Alternatively one can argue that pore-scale processes control the existence of the resonant peak. The porous media constructed by a stochastic process (Spheres and Rectangles) display more heterogeneity in terms of pore scale structures. More specifically, the Spheres medium was built with a broader pore-size distribution than the other three media. In heterogeneous media, at the pore-scale, one should expect the plane wave assumption for the pressure propagation at the continuum scale to fail. In media that display competing pathways with different hydraulic responses, pore pressure gradients can become significant perpendicular to the main direction of propagation, and mass/pressure exchanges between different pathways may significantly affect the stress propagation. The visualization of the pore pressure distribution in the Spheres medium over time during one period can yield important information about the propagation of stress transients in the porous medium. Fig. 5.11 shows snapshots of the pore-pressure field. I observe pressure waves propagating

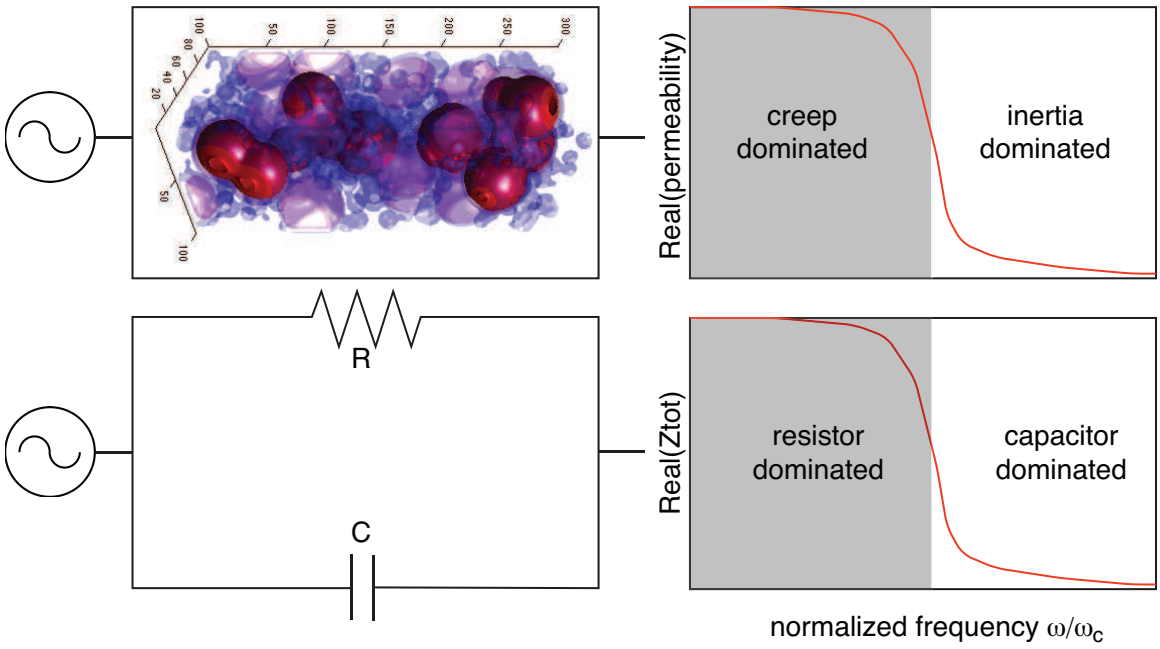

Figure 5.9: Analogy between the dynamic permeability model of Johnson et al. [85] and RC electric circuits in parallel. The spectral response of the effective permeability is similar to the spectral response of the overall impedance of the electric circuit.

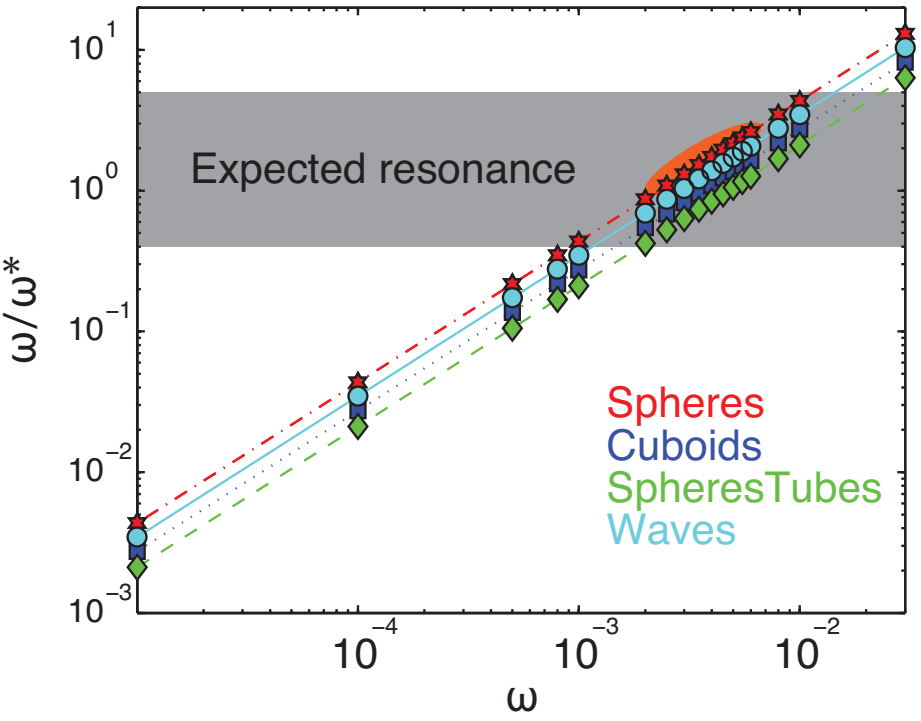

Figure 5.10: Comparison between the sampled forcing frequency used in my simulations and the estimated range for the resonant frequency of the hyperbolic forced mass conservation equation $\omega*$. I observe that my sampling should have allowed one to observe resonance in all four media. The orange ellipse marks the region where I observe the resonance for the data in red.

from the outlet (right) into the medium. An important feature worth noting is that far a fixed distance from the dynamic boundary (outlet) the pore pressure can vary significantly spatially. A possible explanation for the resonant behavior is that a heterogeneous porous medium can be viewed as a collection of connected primary and secondary pathways for the fluid and by extension pressure wave propagation. One clearly observes from Fig. 5.11 that pressure fluctuations can propagate further into the medium along the main flow pathways forming some important pressure gradients perpendicular to the main flow direction. This should lead to significant mass exchanges between connected pathways with different transient responses to stress propagation.

The resonant behavior may be associated with the existence of a finite time-delay for the pore pressure to relax between primary and secondary pathways. If the response time for the pore pressure exchange between competing but connected pathways approaches the period of the forcing, I argue that resonance may possibly occur. Because these features in the Spheres medium are sub-REV, it could explain the shortcomings of the continuum-scale interpretation to explain resonance. It is interesting to reflect on the major differences between my study and that of Pazdniakou and Adler [147] where they do not observe resonance. Pazdniakou and Adler [147] introduce the forcing as a homogenous oscillatory perturbation of a bulk force in the fluid and consider periodic and, therefore, infinite media. The homogeneous forcing applied in their study does not allow the build-up of significant pore scale pressure gradients as the fluid responds uniformly to the perturbation instantaneously. There is no transport of the information on the changing pore-pressure from the boundaries of the domain (there are no boundaries) and therefore no finite time response of the domain to the excitation. This could explain the different results between the two studies.

In the future, I plan on developing more highly heterogeneous structures at the pore scale and test whether resonance is promoted by pore-scale heterogeneities. In parallel, I suggest that an idealized theoretical model that decomposes the porous medium as a collection of regions according the fluid's mobility (dual and multirate mass transfer models by Harvey and Gorelick [69, 101, 149]). Such a framework including a finite relaxation time

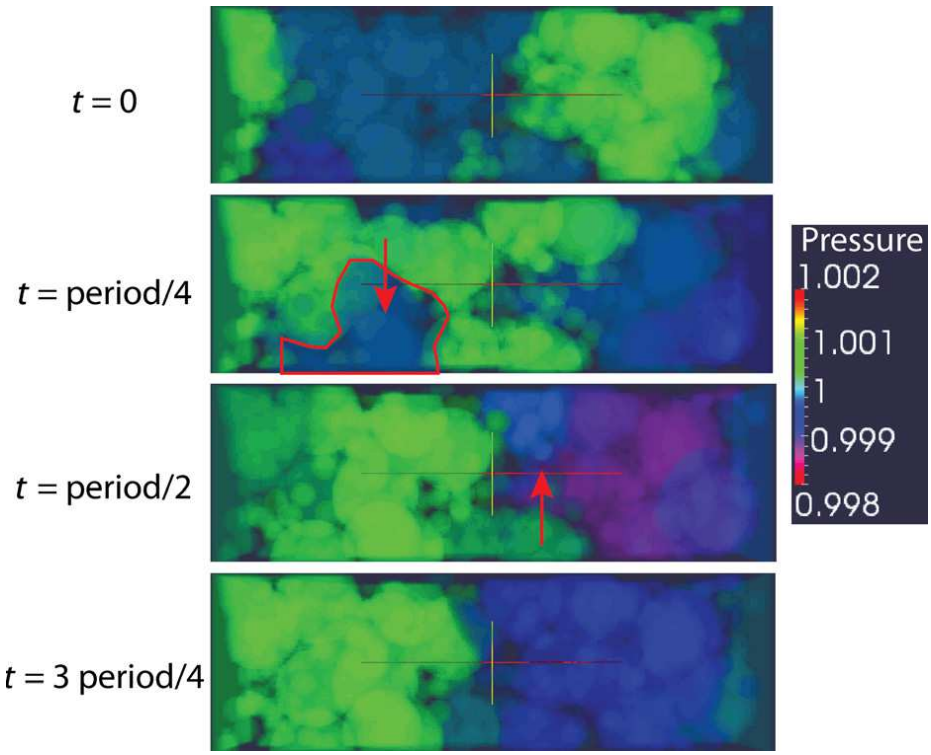

Figure 5.11: 3-D visualization of the pore-pressure field (normalized) at the forcing frequency corresponding to the maximum of the resonance peak in the Spheres medium. The four images show the temporal evolution of the pressure field every quarter period. Note the regions with large lateral pore pressure gradients (the imposed gradient is left to right) highlighted in red. It shows that flow pathways with different hydraulic connectivity have different response time to the forcing and that large pore-scale pore pressure imbalance can emerge, violating the assumption of planar pressure wave propagating from the outlet.

for pressure (leakage) between the more mobile and less mobile subsets of the medium could provide a framework to test if pore-scale heterogeneity can influence a significant departure to the theory of JKD and even lead to resonant effects.

5.1.7 Conclusions

The propagation of pore-pressure transients in saturated porous media is complex at high frequency, when the short wavelength can interact with the heterogeneous structure of the medium. Over the last three decades, successful models for the dynamic response of porous media to harmonic pressure forcing have been developed and tested. They highlight that only three continuum scale descriptors of the complex pore structure are important in homogeneous and isotropic media to characterize the spectral response of permeability. These descriptors are the porosity of the medium, its formation factor and its static permeability. I have constructed four synthetic porous medium from the pore-scale with different porosity, formation factors and permeability. Using a lattice Boltzmann method to compute the fluid flow at the pore-scale I find a very good agreement between my results and the theory for porous media with relatively narrow pore size distributions.

The medium that shows the broadest range of pore sizes however has a distinctive response to the imposed pressure transients. I observe a feature that resembles a resonance peak for the effective permeability at high frequency. Drawing from analogies with electric circuits and heat wave models, I postulate that the resonance feature is either governed by processes that operate at the continuum scale or by pore scale processes that arise because of significant pore-scale heterogeneity. The development of a mass conservation equation at the continuum scale that corrects for the finite time required for pore pressure to propagate in the medium allows for resonance behavior to take place. It predicts resonance over the correct range of frequency for the case where my numerical results display resonant features. It however fails to explain the absence of resonance observed for the other media. Based on my numerical results I argue that the resonance I observe is rather caused by pore-scale processes, whereby significant local pore pressure gradients can form between heterogeneous

flow pathways characterized by different response timescales to the imposed pressure excitations. Future studies focused on the distribution of pore pressure in heterogeneous media will potentially shed light on the dynamical processes that control the existence and the factors that govern the resonance of highly heterogeneous and saturated porous media.

CHAPTER VI

CONCLUSIONS AND RECOMMENDATIONS

6.1 Summary

This dissertation has mainly contributed towards quantifying volatile degassing processes. Degassing and the behavior of bubbly suspensions under shear (another aspect of the research presented here) are two fundamental aspects that govern the ascent of magmas to the surface and their behavior during eruptions. Key contributions are as follows:

1. In Chap. 2, I carried out numerical simulations for the mass balance of sulfur in degassing magmas. I found that the excess sulfur can mostly come from isobaric crystallization processes in crystal-rich magmas. This contrasts with eruptions involving crystal-poor magmas, where I argue that open system processes (recharge of gases from below and bubble accumulation) play a dominant role on the sulfur mass balance.

2. In Chap. 3, I propose a method where volatile (H_2O and CO_2) diffusion profiles around bubbles quenched in pyroclasts can be used to infer the non-linear nature of the decompression rate experienced by magmas as they rise to the surface. I found that (1) when magmas ascend following different decompression paths, the disequilibrium states of H_2O and CO_2 between bubbles and the melt are different; (2) the effective average magma decompression rate is overestimated if one assumes a constant decompression rate.

3. Chap. 4 extends the bubble dynamics models proposed Chaps. 2 and 3 by taking into account the hydrodynamical interactions between bubbles, e.g., bubble deformation and coalescence. Bubbles are allowed to deform, i.e., they are not restrained to be spherical. Bubble dynamics calculations based on this new model is conducted to replicate Ostwald ripening and bubble deformation under simple shear flow conditions

over a range of capillary numbers. This new generation of bubble dynamics model is complex but has the potential to allow one to better understand the mechanical coupling between bubbles and melt during magma ascent.

4. Chap. 5 represents part of my Ph.D. work that is not directly related to the chemical and dynamical coupling between bubbles and melts. In this chapter, the dynamical response of saturated porous media to transient stresses is studied using a pore-scale modeling approach. The influence of the porous media topology on its dynamical response to dynamic stresses is explored and it is shown that small degrees of heterogeneity (pore size and shapes) can have a large impact on the dynamic permeability of the medium and by extension on seismic attenuation (at high frequency).

6.2 Recommendations for future work

Some possible extensions of the work presented in this dissertation and future directions are discussed below.

6.2.1 Further improvement of the spherical cell bubble growth model for magmas

In Chap. 2 and 3, the bubble growth model is formulated under isothermal conditions. These models work under a suite of assumptions such as,

- Decompression model
  - linear decompression rate
  - constant bubble/melt partition coefficient for sulfur
  - constant sulfur diffusivity
- Second boiling
  - linear crystallization rate
  - linear fit of bubble/melt partition coefficient for sulfur
  - constant melt/solid partition coefficient for water and sulfur
  - constant sulfur diffusivity and no redox constraint on the sulfur species

These assumptions can be refined as more experimental data are published. However, for most of these assumptions, the results I obtain will only be adjusted slightly as some of these assumptions are quite robust (e.g., linear crystallization rate for second boiling simulations).

Moreover, in the current model, sulfur speciation in the melt is not included, because in Chap. 2, most subduction zone volcanism that exhibit large excess sulfur are oxidized system, and sulfate is considered to be dominant species in these oxidized melts. Over a range of redox conditions applicable to arc magmas, it is possible that multiple sulfur species can coexist in the melt (S^{2-} and S^{6+}) [167]. When the oxygen fugacity fO_2 is greater than NNO + 1, pyrrhotite is almost depleted and the bubble/melt partition coefficient is largely determined by the solublity of anhydrite. In reduced magmas ($fO_2 < NNO + 1$), the bubble/melt partition coefficient could approach 1, while at oxidized state ($fO_2 > NNO + 1$), the bubble/melt partition coefficient is almost 1000. The oxygen fugacity of a melt is also varying with respect to crystallization and degassing and it would then be important to include sulfur speciation in these degassing models. Sulfur speciation would also allow one to consider stable S isotopes in those calculations, which would provide information about the kinetics and state of the magma during degassing.

6.2.2 Bubble hydrodynamical interactions and volatile kinetics

The model proposed in Chap. 4 can reproduce the mass transfer for Ostwald ripening and bubble deformation under simple shear flows. There are several improvements for this model that could be addressed in the future.

3D expansion The model in Chap. 4 only represents a 2D model for bubble dynamics, which means that what the model simulates is actually a cylinder instead of a 3D bubble. However, in some cases, such as rising bubbles of large Eo number (ratio of the gravitational force to the surface tension force) and low Ga number (ratio of the gravitational force to the viscous force), 2D simulations could provide results that are not consistent with 3D simulations, yet fail to describe the inherent bubble dynamics [201].

Compressibility Most of the existing lattice Boltzmann BGK models (LBGK) can be viewed as compressible schemes to simulate incompressible fluid flows. The compressible effect might lead to some undesirable errors in numerical simulations [66]. The LBM model in Chap. 4 also relies on such a compressible scheme. Without abrupt change of ambient pressure, such scheme works well. However, a more interesting problem for volcanologist is to study volatile degassing when bubbly magma is under decompression. In such case, a compressible LBGK scheme for the melt may fail to provide correct results. Therefore, an imcompressible LBGK scheme [66] is called upon to solve such problems.

High performance computing The current model in Chap. 4 is implemented as a sequential scheme, and a single test run for 20 bubbles in a 200×100 grid box in Fig. 4.13 takes $2 \sim 3$ days to get the results. It represents a simulation of a bubbly flow of a volume fraction of 14 vol.%. In the future, this number could be larger, and based upon the current the computing efficiency, the running time for each case could be weeks. Thus, efficiently parallelizing the current model is important in order to shorten the computing time especially to model a large system. LBM is an ideal candidate for parallelization.

Integration with other numerical methods As compared to the finite-difference methods (FDM) and finite-element methods (FEM), LBM is a relatively novel scheme. It is a powerful tool to study complex fluid flow problems including single and multiphase flow in complex geometries. However, when dealing with highly irregular interfaces, the errors that are generated from the calculation of the local normal direction and curvature could cause large errors in the system. While an irregular interface is common in multiphase flow, e.g., a cluster of bubble in a viscous melt, scheme that can track the interface geometry accurately would allow more sophisticated calculation of interface stresses between bubbles and melt, which would be important to study fragmentation processes, for example. The boundary integral method (BIM) [150] can be used to estimate the interface geometry and the physical values at the interface.

BIM has been used to simulate bubble evolution in a gravity field with various ambient flow conditions, and it is considered to be able to provide more accurate result at the bubble/melt interface. By combining the BIM to track the interface and LBM (calculating the ambient melt and volatile diffusion in the melt), it may be possible to improve the understanding of bubble dynamics in deforming melts significantly.

APPENDIX A

NUMERICAL SCHEMES FOR THE DECOMPRESSION MODEL

$$t^{n+1} = t^n + dt \tag{A.1}$$

$$P_a^{n+1} = 1 - \dot{P}t^{n+1} \tag{A.2}$$

$$R^{n+1} = (R^n - dt\frac{\Sigma}{\Theta_V \eta_{eff}^n})(1 - dt\frac{P^n - P_a^n}{\Theta_V \eta_{eff}^n})^{-1} \tag{A.3}$$

$$r_i^{n+1} = ((r_{0i}^3 - R_0^3) + (R^{n+1})^3)^{1/3}, 0 \leq i \leq N \tag{A.4}$$

$$F_{w,i}^{n+1} = D_{w,i}^{n+1}\frac{2(r_i^{n+1})^2}{C_{w,i} - C_{w,i-1}}, 1 \leq i \leq N-1 \tag{A.5}$$

$$F_{w,N}^{n+1} = 0 \tag{A.6}$$

$$C_{w,i}^{n+1} = C_{w,i}^n + \frac{dt}{\Theta_{Dw}}\frac{3(F_{w,i+1}^{n+1} - F_{w,i}^{n+1})}{(r_{i+1}^{n+1})^3 - (r_i^{n+1})^3}, 1 \leq i \leq N-1 \tag{A.7}$$

$$C_{w,0}^{n+1} = K_H\sqrt{P^n} \tag{A.8}$$

$$F_{w,0}^{n+1} = F_{w,1}^{n+1} - \frac{\Theta_{Dw}}{3dt}((r_1^{n+1})^3 - (r_0^{n+1})^3)(C_{w,0}^{n+1} - C_{w,0}^n) \tag{A.9}$$

$$M_w^{n+1} = M_w^n + 3\rho_m dt\frac{F_{w,0}^{n+1}}{\Theta_{Dw}} \tag{A.10}$$

$${}^1F_{s,i}^{n+1} = D_{s,i}^{n+1}\frac{2(r_i^{n+1})^2}{C_{s,i} - C_{s,i-1}}, 1 \leq i \leq N-1 \tag{A.11}$$

$${}^1F_{s,N}^{n+1} = 0 \tag{A.12}$$

$${}^1C_{s,i}^{n+1} = C_{s,i}^n + \frac{dt}{\Theta_D}\frac{3(F_{s,i+1}^{n+1} - F_{s,i}^{n+1})}{(r_{i+1}^{n+1})^3 - (r_i^{n+1})^3}, 1 \leq i \leq N-1 \tag{A.13}$$

$${}^1C_{s,0}^{n+1} = K_s^n C_{s,b} \tag{A.14}$$

$${}^1F_{s,0}^{n+1} = F_{s,1}^{n+1} - \frac{\Theta_D}{3dt}((r_1^{n+1})^3 - (r_0^{n+1})^3)(C_{s,0}^{n+1} - C_{s,0}^n) \tag{A.15}$$

$${}^1M_s^{n+1} = M_s^n + 3\rho_m dt\frac{F_{s,0}^{n+1}}{\Theta_D} \tag{A.16}$$

$$M^{n+1} \approx M_w^{n+1} \tag{A.17}$$

$$P^{n+1} = M_w/(R^{n+1})^3 \tag{A.18}$$

$$dt < \Theta_V \left| \frac{(P_a^n - P^n)(R^3)^n - 3\rho_m(r_1^3 - r_0^3)C_{w,0}^n}{3\rho_m F_{w,1}^n} \right| \tag{A.19}$$

$$dt < \min\left(\frac{R^{n+1}\Theta_V \eta_{eff}^{n+1}}{\Sigma}, \frac{\Theta_V \eta_{eff}^{n+1}}{|P^{n+1} - P_a^{n+1}|} \right) \tag{A.20}$$

$$dt < \frac{\Theta_{Dw}}{6} \min\left[(r_{i+1}^{n+1})^3 - (r_i^{n+1})^3) \frac{r_{i+1}^{n+1} - r_{i-1}^{n+1}}{D_{w,i}^{n+1}(r_i^{n+1})^2} \right] \tag{A.21}$$

Above is the numerical scheme for the decompression model, and the non-dimentiona process is the same as those in Ref. [44]. The diffusion equations are solved by the finite volume schemes, detailed derivation can be found in Ref. [44]. A flow chart of this decompression model was shown in Fig. A.1. Temperature is needed to calculate the gas density ρ from the ideal gas law, and later this $\hat{\rho}$ would be used as the density unit to quantify dimensionless magma density ρ_m. Eqs. A.19, A.20, and A.21 are required to calculate dt at each time step to make sure: 1, bubbles can grow; 2, the radius of bubble is always greater than 0; 3, the volatile concentration is also greater than zero.

[1]Equations added in this work

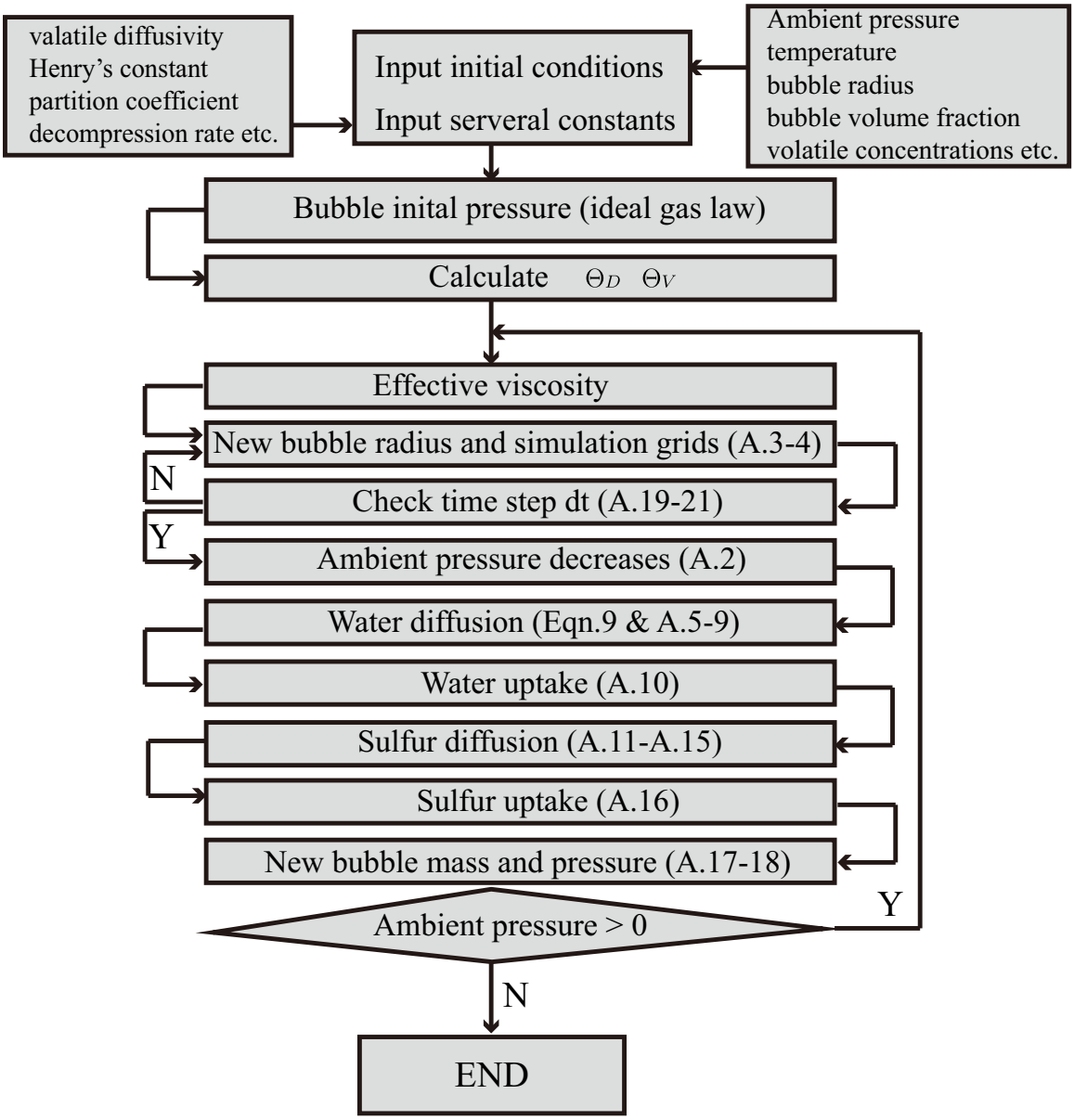

Figure A.1: Flowchart for decompression calculations.

APPENDIX B

NUMERICAL SCHEMES FOR THE SECOND BOILING MODEL

$$t^{n+1} = t^n + dt \tag{B.1}$$

$${}^2F_m^{n+1} = F_{m,ini} - \dot{\chi} dt \tag{B.2}$$

$$R^{n+1} = \left(\frac{M^{n+1}}{P^{n+1}}\right)^{1/3} \tag{B.3}$$

$${}^2S^{n+1} = ((S_0^3 - R_0^3)F_m^{n+1} + (R^{n+1})^3)^{1/3} \tag{B.4}$$

$${}^2r_i^{n+1} = ((r_{0i}^3 - R_0^3)F_m^{n+1} + (R^{n+1})^3)^{1/3}, 0 \le i \le N \tag{B.5}$$

$$P^{n+1} = (P_a + \frac{\Sigma}{R^{n+1}}) \tag{B.6}$$

$${}^2\lambda^{n+1} = (K_w^* - 1)\frac{dF_m}{F_m^n} \tag{B.7}$$

$${}^2\lambda_s^{n+1} = (K_s^* - 1)\frac{dF_m}{F_m^n} \tag{B.8}$$

$${}^2C_{w,i}^{n+1} = (1 + \lambda^{n+1})K_H\sqrt{P^{n+1}}, 1 \le i \le N-1 \tag{B.9}$$

$$C_{w,0}^{n+1} = CH\sqrt{P^{n+1}} \tag{B.10}$$

$${}^2\lambda_1^{n+1} = 1 - (1 + \lambda^{n+1})\frac{F_m^{n+1}}{F_m^n} \tag{B.11}$$

$${}^2M_{w,shell}^{n+1} = \rho_m \sum_{n=0}^{N-1} C_{w,i}^{n+1}((r_{i+1}^{n+1})^3 - (r_i^{n+1})^3)) \tag{B.12}$$

$${}^2M_{w,solid}^{n+1} = \lambda_1\rho_m \sum_{n=0}^{N-1} C_{w,i}^{n+1}((r_{i+1}^{n+1})^3 - (r_i^{n+1})^3)) \tag{B.13}$$

$${}^2M_w^{n+1} = M_{w,total} - M_{w,shell}^{n+1} - M_{w,solid}^{n+1} \tag{B.14}$$

$${}^2C_{s,i}^{'} = (1 + \lambda^{n+1})C_{s,i}^n, 0 \le i \le N-1 \tag{B.15}$$

$${}^2F_{s,i}^{n+1} = D_{s,i}^{n+1}\frac{2(r_i^{n+1})^2}{C_{s,i} - C_{s,i-1}}, 1 \le i \le N-1 \tag{B.16}$$

$${}^2F_{s,N}^{n+1} = 0 \tag{B.17}$$

$${}^2C_{s,i}^{n+1} = C_i^{'} + \frac{dt}{\Theta_D}\frac{3(F_{s,i+1}^{n+1} - F_{s,i}^{n+1})}{(r_{i+1}^{n+1})^3 - (r_i^{n+1})^3}, 1 \le i \le N-1 \tag{B.18}$$

$$
\begin{aligned}
{}^2C_{s,0}^{n+1} &= K_s^n C_{s,b}^n && \text{(B.19)}\\
{}^2F_{s,0}^{n+1} &= F_{s,1}^{n+1} - \frac{\Theta_D}{3dt}((r_1^{n+1})^3 - (r_0^{n+1})^3)(C_{s,0}^{n+1} - C_{s,0}^n(1+\lambda_s^{n+1})) && \text{(B.20)}\\
{}^2M_s^{n+1} &= M_s^n + 3\rho_m dt \frac{F_{s,0}^{n+1}}{\Theta_D} && \text{(B.21)}\\
{}^2C_{s,b}^{n+1} &= \frac{M_s^{n+1}}{M_s^{n+1} + M_w^{n+1}} && \text{(B.22)}\\
M^{n+1} &\approx M_w^{n+1} && \text{(B.23)}\\
dt &< \min\left(\frac{R^{n+1}\Theta_V \eta_{eff}^{n+1}}{\Sigma}, \frac{\Theta_V \eta_{eff}^{n+1}}{|P^{n+1} - P_a^{n+1}|}\right) && \text{(B.24)}\\
dt &< \frac{\Theta_{Ds}(1+\lambda^{n+1})}{6} \min\left[(r_{i+1}^{n+1})^3 - (r_i^{n+1})^3)\frac{r_{i+1}^{n+1} - r_{i-1}^{n+1}}{D_{s,i}^{n+1}(r_i^{n+1})^2}\right] && \text{(B.25)}
\end{aligned}
$$

Above is our second boiling scheme, in which we used the melt fraction F_m instead of crystallinity χ. A flow chart is shown if Fig. B.1. The derivations of Eqs. B(7–17) are from the conservation of the total water and sulfur mass respectively. And similar to the decompression scheme, in order to stabilize the simulation, the time step dt should satisfy only need to satisfy Eqs. B(23–24) are required to calculate dt at each time step to make sure: 1, the radius of bubble is always greater than 0; 2, the volatile concentration is also greater than zero.

[2]Equations added in this work

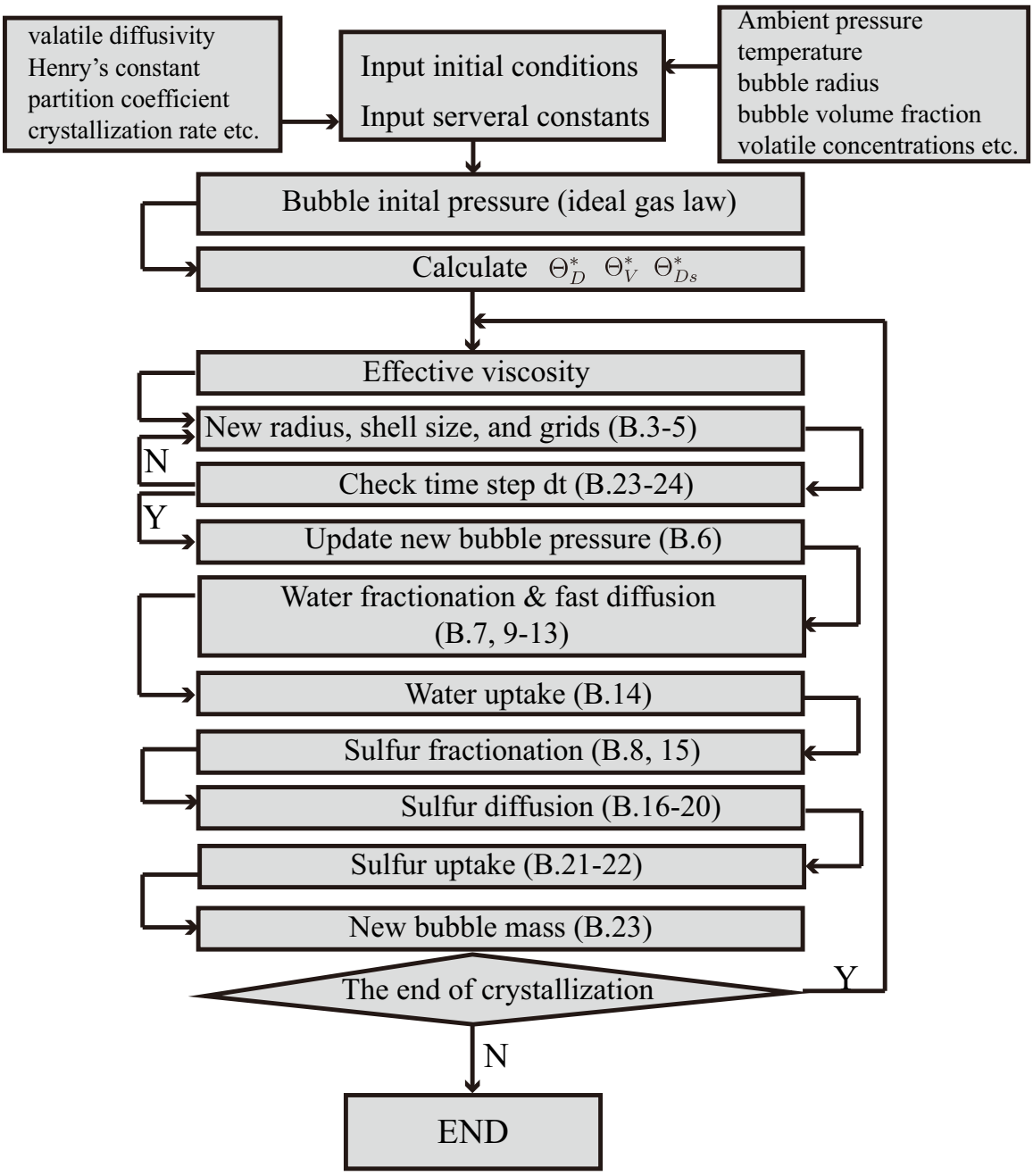

Figure B.1: Flowchart for simulating second boiling

.

APPENDIX C

NOTATION LIST FOR CHAPTER 2

b	coefficient for diffusivity (12.574).
$C^n_{w,i}$	water concentration at r_i at nth step.
$C^n_{s,i}$	sulfur concentration at r_i at nth step.
$C^{'}_{s,i}$	sulfur concentration at r_i at nth step after fractionation.
$\langle C_s \rangle$	average sulfur concentration in the melt shell.
D_{wi}	initial water diffusivity ($3.16 \times 10^{-11} m^2 \cdot s^{-1}$).
D_{si}	initial sulfur diffusivity ($5 \times 10^{-14} m^2 \cdot s^{-1}$).
$D^n_{w,i}$	water initial diffusivity at r_i at nth step.
E^{dry}_{η}	activation energy for the viscosity ($3.045\ J \cdot mole^{-1}$).
E_{Dw}	activation energy for the water diffusivity ($87300 J \cdot mole^{-1}$).
$F^n_{w,i}$	water flux at r_i at nth step.
$F_{m,ini}$	initial melt fraction.
F^n_m	melt fraction at nth step.
$F^n_{s,i}$	sulfur flux at r_i at nth step.
M^n	bubble mass at nth step.
M^n_w	water mass in gas phase at nth step.
$M^n_{w,shell}$	water mass in melt phase at nth step.
$M^n_{w,solid}$	water mass in solid phase at nth step.
k_{η}	volatile correction coefficient for viscosity.
K_H	Henry's constant ($3.44 \times 10^{-6} kg^{-1/2} m^{1/2}$).
K_s	sulfur partition coefficient between the gas and melt.
$\langle K_s \rangle$	effective sulfur partition coefficient between the gas and melt.
K^w_*	water partition coefficient between the solid and melt.
K^s_*	sulfur partition coefficient between the solid and melt.

P	bubble pressure.
$\dot{P}$	decompression rate.
P_a	ambient pressure (Pa).
P_i	initial ambient pressure ($10^8 P_a$ for decompression and $2 \times 10^8 P_a$ for second boiling).
r	radial distance to the bubble-melt interface.
R	bubble radius.
R_{gas}	ideal gas constant ($8.31 J \cdot mole^{-1} \cdot K^{-1}$).
S	the radius of the melt region.
t	time.
dt	time step.
T	melt temperature (K).
η	melt viscosity.
η_{eff}	melt effective viscosity.
ρ_m	melt density ($2354 kg \cdot m^{-3}$).
ρ	bubble gas density.
α_i	initial bubble volume fraction (0.041 for decompression and 0.001 for second boiling).
χ	crystallinity.
$\dot{\chi}$	crystallization rate.
$\Delta\chi$	interval of crystal content that magma experienced during second boiling.
σ	bubble surface tension ($0.1 J \cdot m^{-2}$).
Σ	dimensionless bubble surface tension.

APPENDIX D

NOTATION LIST FOR CHAPTER 4

A	surface area of gas-melt interface surfaces.
B_o	Bond number.
c_Π	amplitude of the disjoining pressure.
c_Π	lattice speed in LBM model.
C	concentration of dissolved water content.
C_b	concentration of dissolved water content at the bubble-melt interface.
d_{range}	range of the disjoining pressure.
d_{int}	distance between interacting interfaces neighbor objects.
D	parameter of deformation of bubbles.
D_{H_2O}	diffusion coefficient of the dissolved volatile.
$\mathbf{e}_i$	lattice velocity in i direction of LBM model.
f_i	distribution function in i direction of D2Q9 model.
F_i	body force in i direction on f_i.
g_i	distribution function in i direction of D2Q4 model.
G	Gibbs free energy.
H	distance between two walls in simulation model of shear effect on bubbles.
n	moles of gas molecules.
p_g	gas pressure.
r	bubble radius.
R	ideal gas constant.
S	Henry's constant.
t	time.
t_{dec}	decompression timescale.
t_{vis}	viscosity timescale.
t_c	drainage time ($B_o < 0.25$).
t_g	drainage time ($B_o > 0.25$).
t_d	experimental normalized drainage time.
T	temperature.
U_w	bottom wall velocity in simulation model of shear effect on bubbles.
V	gas volume.

w_i	lattice weights in LBM model.
ρ	density.
ν	kinetic viscosity.
μ	dynamic viscosity.
ϵ	strain.
$\dot{\epsilon}$	strain rate.
τ_F	relaxation time for melt in LBM model.
τ_G	relaxation time for gas in LBM model.
κ	curvature of gas-melt interface.
σ	surface tension.
Π	disjoining pressure.
δ	critical thickness of the melt film between bubbles.
δ_i	initial melt film thickness.
Δ_ρ	density difference betwwen the bubble and the ambient fluid.
θ	orientation of bubbles, angle between the long axis of bubble and the shear flow.
t	time
t_{dec}	decompression timescale
t_{vis}	viscosity timescale
t_c	drainage time ($B_o < 0.25$)
t_g	drainage time ($B_o > 0.25$)
t_d	experimental normalized drainage time
T	temperature
U_w	bottom wall velocity in simulation model of shear effect on bubbles
V	gas volume
ρ	density
ν	kinetic viscosity
μ	dynamic viscosity
ϵ	strain
$\dot{\epsilon}$	strain rate
κ	curvature of gas-melt interface
σ	surface tension
Π	disjoining pressure
δ	critical thickness of the melt film between bubbles
δ_i	initial melt film thickness
Δ_ρ	density difference betwwen the bubble and the ambient fluid
θ	orientation of bubbles, angle between the long axis of bubble and the shear flow

REFERENCES

[1] Alletti, M., Baker, D. R., and Freda, C., "Halogen diffusion in a basaltic melt," *Geochim. Cosmochim. Acta*, vol. 71, no. 14, pp. 3570–3580, 2007.

[2] Anderson, A. T., "Chlorine, sulfur, and water in magmas and oceans," *Geol. Soc. Am. Bull.*, vol. 85, no. 9, pp. 1485–1492, 1974.

[3] Anderson, A. T., "Some basaltic and andesitic gases," *Rev. Geophys.*, vol. 13, no. 1, pp. 37–55, 1975.

[4] Anderson, A. T., "Hourglass inclusions: theory and application to the Bishop Rhyolitic Tuff," *Am. Mineral.*, vol. 76, no. 3–4, pp. 530–547, 1991.

[5] Andres, R. J., Rose, W. I., Kyle, P. R., Desilva, S., Francis, P., Gardeweg, M., and Roa, H. M., "Excessive sulfur-dioxide emission from chilean volcanos," *J. Volcanol. Geotherm. Res.*, vol. 46, no. 3–4, pp. 323–329, 1991.

[6] Attar, E. and Körner, C., "Lattice Boltzmann method for dynamic wetting problems," *J. Colloid Interface Sci.*, vol. 335, no. 1, pp. 84–93, 2009.

[7] Bacon, C. R., "Crystallization of accessory phases in magmas by local saturation adjacent to phenocrysts," *Geochim. Cosmochim. Acta*, vol. 53, no. 5, pp. 1055–1066, 1989.

[8] Baker, D. R., Lang, P., Robert, G., Bergevin, J.-F., Allard, E., and Bai, L., "Bubble growth in slightly supersaturated albite melt at constant pressure," *Geochim. Cosmochim. Acta*, vol. 70, no. 7, pp. 1821–1838, 2006.

[9] Baker, L. L. and Rutherford, M. J., "Sulfur diffusion in rhyolite melts," *Contrib. Mineral. Petrol.*, vol. 123, no. 4, pp. 335–344, 1996.

[10] Beermann, O., Botcharnikov, R. E., Holtz, F., Diedrich, O., and Nowak, M., "Temperature dependence of sulfide and sulfate solubility in olivine-saturated basaltic magmas," *Geochim. Cosmochim. Acta*, vol. 75, no. 23, pp. 7612–7631, 2011.

[11] Bentley, B. J. and Leal, L. G., "An experimental investigation of drop deformation and breakup in steady, two-dimensional linear flows," *J. Fluid Mech.*, vol. 167, pp. 241–283, June 1986.

[12] Berryman, J. G., "Dynamic permeability in poroelasticity," *Stanford Explor. Project*, vol. 113, pp. 1–454, Aug. 2003.

[13] Bhatnagar, P. L., Gross, E. P., and Krook, M., "A model for collision processes in gases. I. Small amplitude processes in charged and neutral one-component systems," *Phys. Rev.*, vol. 94, pp. 511–525, May 1954.

[14] Biot, M. A., "Theory of propagation of elastic waves in a fluid-saturated porous solid. I. Low-frequency range," *J. Acoust. Soc. Am.*, vol. 28, pp. 168–178, Mar. 1956.

[15] Biot, M. A., "Theory of propagation of elastic waves in a fluid-saturated porous solid. II. Higher-frequency range," *J. Acoust. Soc. Am.*, vol. 28, pp. 179–191, Mar. 1956.

[16] Biot, M. A., "Generalized theory of acoustic propagation in porous dissipative media," *J. Acoust. Soc. Am.*, vol. 34, pp. 1254–1264, Sept. 1962.

[17] Blower, J. D., Keating, J. P., Mader, H. M., and Phillips, J. C., "Inferring volcanic degassing processes from vesicle size distributions," *Geophys. Res. Lett.*, vol. 28, no. 2, pp. 347–350, 2001.

[18] Bluth, G. J. S., Schnetzler, C. C., Krueger, A. J., and Walter, L. S., "The contribution of explosive volcanism to global atmospheric sulphur dioxide concentrations," *Nature*, vol. 366, no. 6453, pp. 327–329, 1993.

[19] Bluth, G. J. S., Doiron, S. D., Schnetzler, C. C., Krueger, A. J., and Walter, L. S., "Global tracking of the so_2 clouds from the June, 1991 Mount Pinatubo eruptions," *Geophys. Res. Lett.*, vol. 19, no. 2, pp. 151–154, 1992.

[20] Borisova, A., Toutain, J.-P., Dubessy, J., Pallister, J., Zwick, A., and Salvi, S., "H_2O-CO_2-S fluid triggering the 1991 Mount Pinatubo climactic eruption (Philippines)," *Bull. Volcanol.*, vol. 76, no. 2, pp. 1–9, 2014.

[21] Burgisser, A. and Gardner, J. E., "Experimental constraints on degassing and permeability in volcanic conduit flow," *Bull. Volcanol.*, vol. 67, no. 1, pp. 42–56, 2004.

[22] Carn, S. A. and Bluth, G. J. S., "Prodigious sulfur dioxide emissions from Nyamuragira volcano, DR Congo," *Geophys. Res. Lett.*, vol. 30, no. 23, 2003.

[23] Carroll, M. R. and Rutherford, M. J., "Sulfide and sulfate saturation in hydrous silicate melts," *J. Geophys. Res.: Solid Earth*, vol. 90, no. S02, pp. C601–C612, 1985.

[24] Carroll, M. R. and Rutherford, M. J., "The stability of igneous anhydrite: Experimental results and implications for sulfur behavior in the 1982 El Chichon trachyandesite and other evolved magmas," *J. Petrol.*, vol. 28, no. 5, pp. 781–801, 1987.

[25] Carroll, M. R. and Webster, J. D., "Solubilities of sulfur, noble gases, nitrogen, chlorine, and fluorine in magmas," *Rev. Mineral. Geochem.*, vol. 30, no. 1, pp. 231–279, 1994.

[26] Cattaneo, C. and Kampé de Fériet, J., *Sur une forme de l'équation de la chaleur éliminant le paradoxe d'une propagation instantanée*. Paris: Gauthier-Villars, 1958.

[27] Chambefort, I., Dilles, J. H., and Kent, A. J. R., "Anhydrite-bearing andesite and dacite as a source for sulfur in magmatic-hydrothermal mineral deposits," *Geology*, vol. 36, no. 9, pp. 719–722, 2008.

[28] Chesner, C. A. and Luhr, J. F., "A melt inclusion study of the Toba Tuffs, Sumatra, Indonesia," *J. Volcanol. Geotherm. Res.*, vol. 197, no. 1–4, pp. 259–278, 2010.

[29] Churakov, S. and Gottschalk, M., "Perturbation theory based equation of state for polar molecular fluids: I. Pure fluids," *J. Volcanol. Geotherm. Res.*, vol. 67, no. 13, pp. 2397–2414, 2003.

[30] Costa, F., Scaillet, B., and Gourgaud, A., "Massive atmospheric sulfur loading of the AD 1600 Huaynaputina eruption and implications for petrologic sulfur estimates," *Geophys. Res. Lett.*, vol. 30, no. 2, p. 1068, 2003.

[31] Costa, F., Scaillet, B., and Pichavant, M., "Petrological and experimental constraints on the pre-eruption conditions of holocene dacite from Volcán San Pedro (36°S, Chilean Andes) and the importance of sulphur in silicic subduction-related magmas," *J. Petrol.*, vol. 45, no. 4, pp. 855–881, 2004.

[32] Criswell, C. W., "Chronology and pyroclastic stratigraphy of the May 18, 1980, eruption of Mount St. Helens, Washington," *J. Geophys. Res.: Solid Earth*, vol. 92, no. B10, pp. 10237–10266, 1987.

[33] Dasgupta, R. and Hirschmann, M. M., "The deep carbon cycle and melting in earth's interior," *Earth Planet. Sci. Lett.*, vol. 298, no. 1–2, pp. 1–13, 2010.

[34] de Hoog, J. C. M., Koetsier, G. W., Bronto, S., Sriwana, T., and van Bergen, M. J., "Sulfur and chlorine degassing from primitive arc magmas: Temporal changes during the 1982–1983 eruptions of Galunggung (West Java, Indonesia)," *J. Volcanol. Geotherm. Res.*, vol. 108, no. 1–4, pp. 55–83, 2001.

[35] de Silva, S. L. and Zielinski, G. A., "Global influence of the AD 1600 eruption of Huaynaputina, Peru," *Nature*, vol. 393, no. 6684, pp. 455–458, 1998.

[36] Debrégeas, G., Gennes, P.-G. d., and Brochard-Wyart, F., "The life and death of "bare" viscous bubbles," *Science*, vol. 279, pp. 1704–1707, Mar. 1998.

[37] DeHoff, R. T., "A geometrically general theory of diffusion controlled coarsening," *Acta Metall. Mater.*, vol. 39, pp. 2349–2360, Oct. 1991.

[38] Devine, J. D., Sigurdsson, H., Davis, A. N., and Self, S., "Estimates of sulfur and chlorine yield to the atmosphere from volcanic eruptions and potential climatic effects," *J. Geophys. Res.: Solid Earth*, vol. 89, no. B7, pp. 6309–6325, 1984.

[39] Dixon, J. E., Clague, D. A., and Stolper, E. M., "Degassing history of water, sulfur, and carbon in submarine lavas from Kilauea Volcano, Hawaii," *J. Geol.*, vol. 99, no. 3, pp. 371–394, 1991.

[40] Druitt, T. and Bacon, C., "Petrology of the zoned calcalkaline magma chamber of Mount Mazama, Crater Lake, Oregon," *Contrib. Mineral. Petrol.*, vol. 101, no. 2, pp. 245–259, 1989.

[41] Edmonds, M., Pyle, D., and Oppenheimer, C., "A model for degassing at the Soufriére Hills Volcano, Montserrat, West Indies, based on geochemical data," *Earth Planet. Sci. Lett.*, vol. 186, no. 2, pp. 159–173, 2001.

[42] Faroughi, S. A. and Huber, C., "Unifying the relative hindered velocity in suspensions and emulsions of nondeformable particles," *Geophys. Res. Lett.*, vol. 42, no. 1, pp. 53–59, 2015.

[43] Fine, G. and Stolper, E., "The speciation of carbon dioxide in sodium aluminosilicate glasses," *Contrib. Mineral. Petrol.*, vol. 91, no. 2, pp. 105–121, 1985.

[44] Forestier-Coste, L., Mancini, S., Burgisser, A., and James, F., "Numerical resolution of a mono-disperse model of bubble growth in magmas," *Appl. Math. Modelling*, vol. 36, no. 12, pp. 5936–5951, 2012.

[45] Frankel, N. A. and Acrivos, A., "The constitutive equation for a dilute emulsion," *J. Fluid Mech.*, vol. 44, pp. 65–78, Oct. 1970.

[46] Freda, C., Baker, D. R., and Scarlato, P., "Sulfur diffusion in basaltic melts," *Geochim. Cosmochim. Acta*, vol. 69, no. 21, pp. 5061–5069, 2005.

[47] Frisch, U., dHumieres, D., Hasslacher, B., Lallemand, P., Pomeau, Y., and Rivet, J. P., "Lattice gas hydrodynamics in two and three dimensions," *Complex Sys.*, vol. 1, Jan. 1987.

[48] Frisch, U., Hasslacher, B., and Pomeau, Y., "Lattice-gas automata for the Navier-Stokes equation," *Phys. Rev. Lett.*, vol. 56, pp. 1505–1508, Apr. 1986.

[49] Gaetani, G. A. and Watson, E. B., "Open system behavior of olivine-hosted melt inclusions," *Earth Planet. Sci. Lett.*, vol. 183, no. 12, pp. 27–41, 2000.

[50] Gaonac′h, H., Lovejoy, S., Stix, J., and Scherzter, D., "A scaling growth model for bubbles in basaltic lava flows," *Earth Planet. Sci. Lett.*, vol. 139, pp. 395–409, Apr. 1996.

[51] Gaonac'h, H., Lovejoy, S., and Schertzer, D., "Scaling vesicle distributions and volcanic eruptions," *Bull. Volcanol.*, vol. 67, pp. 350–357, Apr. 2005.

[52] Gardner, J. E., Hilton, M., and Carroll, M. R., "Bubble growth in highly viscous silicate melts during continuous decompression from high pressure," *Geochim. Cosmochim. Acta*, vol. 64, no. 8, pp. 1473–1483, 2000.

[53] Gardner, J. E., "Heterogeneous bubble nucleation in highly viscous silicate melts during instantaneous decompression from high pressure," *Chem. Geol.*, vol. 236, no. 1–2, pp. 1–12, 2007.

[54] Gardner, J. E., Carey, S., Sigurdsson, H., and Rutherford, M. J., "Influence of magma composition on the eruptive activity of Mount St. Helens, Washington," *Geology*, vol. 23, no. 6, pp. 523–526, 1995.

[55] Gardner, J. E., Hilton, M., and Carroll, M. R., "Experimental constraints on degassing of magma: Isothermal bubble growth during continuous decompression from high pressure," *Earth Planet. Sci. Lett.*, vol. 168, no. 1–2, pp. 201–218, 1999.

[56] Gardner, J. E., Thomas, R. M. E., Jaupart, C., and Tait, S., "Fragmentation of magma during Plinian volcanic eruptions," *Bull. Volcanol.*, vol. 58, no. 2, pp. 144–162, 1996.

[57] Gerlach, T. M., Westrich, H. R., Casadevall, T. J., and Finnegan, D. L., "Vapor saturation and accumulation in magmas of the 1989–1990 eruption of Redoubt volcano, Alaska," *J. Volcanol. Geotherm. Res.*, vol. 62, no. 1–4, pp. 317–337, 1994.

[58] Gerlach, T. M., Westrich, H. R., and Symonds, R. B., *Preeruption vapor in magma of the climactic Mount Pinatubo eruption: Source of the giant stratospheric sulfur dioxide cloud*. Fire and Mud: Eruptions and Lahars of Mount Pinatubo, Philippines, Seattle: Univ. of Wash. Press, 1996.

[59] Giggenbach, W. F., *Chemical composition of volcanic gases*, book section 7, pp. 221–256. Springer Berlin Heidelberg, 1996.

[60] Giordano, D., Russell, J. K., and Dingwell, D. B., "Viscosity of magmatic liquids: A model," *Earth Planet. Sci. Lett.*, vol. 271, no. 14, pp. 123–134, 2008.

[61] Gonnermann, H. M. and Manga, M., "Explosive volcanism may not be an inevitable consequence of magma fragmentation," *Nature*, vol. 426, no. 6965, pp. 432–435, 2003.

[62] Gonnermann, H. M. and Manga, M., "Nonequilibrium magma degassing: Results from modeling of the CA. 1340 A.D. eruption of Mono Craters, California," *Earth Planet. Sci. Lett.*, vol. 238, no. 1–2, pp. 1–16, 2005.

[63] Gonnermann, H. M. and Manga, M., "The fluid mechanics inside a volcano," *Annu. Rev. Fluid Mech.*, vol. 39, pp. 321–356, 2007.

[64] Gualda, G. A., Ghiorso, M. S., Lemons, R. V., and Carley, T. L., "Rhyolite-melts: A modified calibration of melts optimized for silica-rich, fluid-bearing magmatic systems," *J. Petrol.*, vol. 53, no. 5, pp. 875–890, 2012.

[65] Guo, S., Bluth, G. J. S., Rose, W. I., Watson, I. M., and Prata, A. J., "Re-evaluation of SO_2 release of the 15 June 1991 Pinatubo eruption using ultraviolet and infrared satellite sensors," *Geochem. Geophys. Geosyst.*, vol. 5, no. 4, p. Q04001, 2004.

[66] Guo, Z., Shi, B., and Wang, N., "Lattice BGK model for incompressible Navier-Stokes equation," *J. Comput. Phys.*, vol. 165, no. 1, pp. 288–306, 2000.

[67] Gurenko, A. A., Belousov, A. B., Trumbull, R. B., and Sobolev, A. V., "Explosive basaltic volcanism of the Chikurachki volcano (Kurile arc, Russia): Insights on pre-eruptive magmatic conditions and volatile budget revealed from phenocryst-hosted melt inclusions and groundmass glasses," *J. Volcanol. Geotherm. Res.*, vol. 147, no. 3–4, pp. 203–232, 2005.

[68] Han, C. D. and King, R. G., "Measurement of the rheological properties of concentrated emulsions," *J. Rheol.*, vol. 24, pp. 213–237, Apr. 1980.

[69] Harvey, C. and Gorelick, S. M., "Rate-limited mass transfer or macrodispersion: Which dominates plume evolution at the macrodispersion experiment (MADE) site?," *Water Resour. Res.*, vol. 36, pp. 637–650, Mar. 2000.

[70] Hersum, T. G. and Marsh, B. D., "Igneous microstructures from kinetic models of crystallization," *J. Volcanol. Geoth. Res.*, vol. 154, pp. 34–47, June 2006.

[71] Higuera, F. J. and Jiménez, J., "Boltzmann approach to lattice gas simulations," *Euro. Phys. Lett.*, vol. 9, no. 7, p. 663, 1989.

[72] Hildreth, W. and Fierstein, J., "Katmai volcanic cluster and the great eruption of 1912," *Geol. Soc. Am. Bull.*, vol. 112, no. 10, pp. 1594–1620, 2000.

[73] Hinch, E. J. and Acrivos, A., "Long slender drops in a simple shear flow," *J. Fluid Mech.*, vol. 98, pp. 305–328, May 1980.

[74] Hubbert, M. K., "The theory of ground-water motion," *EOS Trans. AGU*, vol. 21, pp. 648–648, July 1940.

[75] Huber, C. and Su, Y., "A pore-scale investigation of the dynamic response of saturated porous media to transient stresses," *Geofluids*, vol. 15, no. 1-2, pp. 11–23, 2015.

[76] Huber, C., Su, Y., Nguyen, C. T., Parmigiani, A., Gonnermann, H. M., and Dufek, J., "A new bubble dynamics model to study bubble growth, deformation, and coalescence," *J. Geophys. Res.: Solid Earth*, vol. 119, no. 1, pp. 216–239, 2014.

[77] Huber, C., Bachmann, O., and Dufek, J., "Crystal-poor versus crystal-rich ignimbrites: A competition between stirring and reactivation," *Geology*, vol. 40, no. 2, pp. 115–118, 2012.

[78] Huber, C., Bachmann, O., and Manga, M., "Two competing effects of volatiles on heat transfer in crystal-rich magmas: Thermal insulation vs defrosting," *J. Petrol.*, vol. 51, no. 4, pp. 847–867, 2010.

[79] Huber, C., Chopard, B., and Manga, M., "A lattice Boltzmann model for coupled diffusion," *J. Comput. Phys.*, vol. 229, pp. 7956–7976, Oct. 2010.

[80] Huber, C., Parmigiani, A., Chopard, B., Manga, M., and Bachmann, O., "Lattice Boltzmann model for melting with natural convection," *Int. J. Heat Fluid Flow*, vol. 29, pp. 1469–1480, Oct. 2008.

[81] Humphreys, M. C. S., Menand, T., Blundy, J. D., and Klimm, K., "Magma ascent rates in explosive eruptions: Constraints from H_2O diffusion in melt inclusions," *Earth Planet. Sci. Lett.*, vol. 270, no. 1–2, pp. 25–40, 2008.

[82] Hurwitz, S. and Navon, O., "Bubble nucleation in rhyolitic melts: Experiments at high pressure, temperature, and water content," *Earth Planet. Sci. Lett.*, vol. 122, no. 3, pp. 267–280, 1994.

[83] Ingebritsen, S. E. and Manning, C. E., "Permeability of the continental crust: Dynamic variations inferred from seismicity and metamorphism," in *Frontiers in Geofluids* (Yardley, B., Craignning, and Garven, G., eds.), pp. 193–205, Wiley-Blackwell, 2010.

[84] Jakubowski, R. T., Fournelle, J., Welch, S., Swope, R. J., and Camus, P., "Evidence for magmatic vapor deposition of anhydrite prior to the 1991 climactic eruption of Mount Pinatubo, Philippines," *Am. Mineral.*, vol. 87, no. 8–9, pp. 1029–1045, 2002.

[85] Johnson, D. L., Koplik, J., and Dashen, R., "Theory of dynamic permeability and tortuosity in fluid-saturated porous media," *J. Fluid Mech.*, vol. 176, pp. 379–402, Mar. 1987.

[86] Johnson, E. R., Kamenetsky, V. S., McPhie, J., and Wallace, P. J., "Degassing of the H_2O-rich rhyolites of the Okataina volcanic center, Taupo volcanic zone, New Zealand," *Geology*, vol. 39, no. 4, pp. 311–314, 2011.

[87] Jugo, P. J., "Sulfur content at sulfide saturation in oxidized magmas," *Geology*, vol. 37, no. 5, pp. 415–418, 2009.

[88] Jugo, P. J., Wilke, M., and Botcharnikov, R. E., "Sulfur k-edge xanes analysis of natural and synthetic basaltic glasses: Implications for s speciation and s content as function of oxygen fugacity," *Geochim. Cosmochim. Acta*, vol. 74, no. 20, pp. 5926–5938, 2010.

[89] Kelley, K. A. and Cottrell, E., "Water and the oxidation state of subduction zone magmas," *Science*, vol. 325, no. 5940, p. 605, 2009.

[90] Keppler, H., "The distribution of sulfur between haplogranitic melts and aqueous fluids," *Geochim. Cosmochim. Acta*, vol. 74, no. 2, pp. 645–660, 2010.

[91] Klimm, K., Kohn, S. C., and Botcharnikov, R. E., "The dissolution mechanism of sulphur in hydrous silicate melts. II: Solubility and speciation of sulphur in hydrous silicate melts as a function of FO_2," *Chem. Geol.*, vol. 322–323, no. 250–267, pp. 250–267, 2012.

[92] Körner, C., Thies, M., Hofmann, T., Thürey, N., and Rüde, U., "Lattice Boltzmann model for free surface flow for modeling foaming," *J. Statis. Phys.*, vol. 121, no. 1, pp. 179–196, 2005.

[93] Larsen, J. F., Denis, M.-H., and Gardner, J. E., "Experimental study of bubble coalescence in rhyolitic and phonolitic melts," *Geochim. Cosmochim. Acta*, vol. 68, no. 2, pp. 333–344, 2004.

[94] Larsen, J. F. and Gardner, J. E., "Experimental constraints on bubble interactions in rhyolite melts: implications for vesicle size distributions," *Earth Planet. Sci. Lett.*, vol. 180, no. 12, pp. 201–214, 2000.

[95] Larsen, J. F. and Gardner, J. E., "Experimental study of water degassing from phonolite melts: implications for volatile oversaturation during magmatic ascent," *J. Volcanol. Geotherm. Res.*, vol. 134, no. 12, pp. 109–124, 2004.

[96] Lautze, N. C., Sisson, T. W., Mangan, M. T., and Grove, T. L., "Segregating gas from melt: an experimental study of the Ostwald ripening of vapor bubbles in magmas," *Contrib. Mineral. Petrol.*, vol. 161, no. 2, pp. 331–347, 2011.

[97] Lensky, N. G., Navon, O., and Lyakhovsky, V., "Bubble growth during decompression of magma: Experimental and theoretical investigation," *J. Volcanol. Geotherm. Res.*, vol. 129, no. 1–3, pp. 7–22, 2004.

[98] Lensky, N. G., Lyakhovsky, V., and Navon, O., "Radial variations of melt viscosity around growing bubbles and gas overpressure in vesiculating magmas," *Earth Planet. Sci. Lett.*, vol. 186, no. 1, pp. 1–6, 2001.

[99] L'Heureux, I., "A new model of volatile bubble growth in a magmatic system: Isobaric case," *J. Geophys. Res.: Solid Earth*, vol. 112, p. B12208, Dec. 2007.

[100] Lifshitz, I. M. and Slyozov, V. V., "The kinetics of precipitation from supersaturated solid solutions," *J. Phys. Chem. Solids*, vol. 19, pp. 35–50, Apr. 1961.

[101] Liu, G., Zheng, C., and Gorelick, S. M., "Evaluation of the applicability of the dual-domain mass transfer model in porous media containing connected high-conductivity channels," *Water Resour. Res.*, vol. 43, p. W12407, Dec. 2007.

[102] Liu, Y., Anderson, A. T., and Wilson, C. J. N., "Melt pockets in phenocrysts and decompression rates of silicic magmas before fragmentation," *J. Geophys. Res.: Solid Earth*, vol. 112, no. B6, 2007.

[103] Liu, Y. and Zhang, Y., "Bubble growth in rhyolitic melt," *Earth Planet. Sci. Lett.*, vol. 181, no. 12, pp. 251–264, 2000.

[104] Liu, Y., Zhang, Y., and Behrens, H., "Solubility of H_2O in rhyolitic melts at low pressures and a new empirical model for mixed H_2O–CO_2 solubility in rhyolitic melts," *J. Volcanol. Geotherm. Res.*, vol. 143, no. 1–3, pp. 219–235, 2005.

[105] London, D., Hervig, R., and Morgan, G. V. I., "Melt-vapor solubilities and elemental partitioning in peraluminous granite-pegmatite systems: Experimental results with Macusani glass at 200 MPa," *Contrib. Mineral. Petrol.*, vol. 99, no. 3, pp. 360–373, 1988.

[106] Ludwig, K., *SQUID 2: A User's Manual*, vol. 12. Berkeley Geochron. Ctr. Spec. Pub., Apr 2009.

[107] Luhr, J. F., "Experimental phase-relations of water-saturated and sulfur-saturated arc magmas and the 1982 eruptions of El-Chichon volcano," *J. Petrol.*, vol. 31, no. 5, pp. 1071–1114, 1990.

[108] Luhr, J. F., Carmichael, I. S. E., and Varekamp, J. C., "The 1982 eruptions of El-Chichon volcano, chiapas, mexico - mineralogy and petrology of the anhydrite-bearing pumices," *J. Volcanol. Geotherm. Res.*, vol. 23, no. 1–2, pp. 69–108, 1984.

[109] Luhr, J. F. and Logan, M. A. V., "Sulfur isotope systematics of the 1982 El Chichón trachyandesite: An ion microprobe study," *Geochim. Cosmochim. Acta*, vol. 66, no. 18, pp. 3303–3316, 2002.

[110] Luhr, J. F. and Melson, W. G., *Mineral and glass compositions in June 15, 1991, pumices: Evidence for dynamic disequilibrium in the dacite of Mount Pinatubo*, pp. 733–750. 1996.

[111] Lyakhovsky, V., Hurwitz, S., and Navon, O., "Bubble growth in rhyolitic melts: experimental and numerical investigation," *Bull. Volcanol.*, vol. 58, pp. 19–32, Sept. 1996.

[112] Macdonald, R., Smith, R. L., and Thomas, J. E., *Chemistry of the subalkalic silicic obsidians*. US Government Printing Office Washington, DC, 1992.

[113] Mandeville, C. W., Carey, S., and Sigurdsson, H., "Magma mixing, fractional crystallization and volatile degassing during the 1883 eruption of Krakatau volcano, Indonesia," *J. Volcanol. Geotherm. Res.*, vol. 74, no. 3–4, pp. 243–274, 1996.

[114] Mandeville, C. W., Webster, J. D., Tappen, C., Taylor, B. E., Timbal, A., Sasaki, A., Hauri, E., and Bacon, C. R., "Stable isotope and petrologic evidence for open-system degassing during the climactic and pre-climactic eruptions of mt. Mazama, Crater Lake, oregon," *Geochim. Cosmochim. Acta*, vol. 73, no. 10, pp. 2978–3012, 2009.

[115] Manga, M. and Loewenberg, M., "Viscosity of magmas containing highly deformable bubbles," *J. Volcanol. Geotherm. Res.*, vol. 105, pp. 19–24, Jan. 2001.

[116] Manga, M., Castro, J., Cashman, K. V., and Loewenberg, M., "Rheology of bubble-bearing magmas," *J. Volcanol. and Geotherm. Res.*, vol. 87, pp. 15–28, Dec. 1998.

[117] Mangan, M. and Sisson, T., "Delayed, disequilibrium degassing in rhyolite magma: Decompression experiments and implications for explosive volcanism," *Earth Planet. Sci. Lett.*, vol. 183, no. 3–4, pp. 441–455, 2000.

[118] Mangan, M. T. and Cashman, K. V., "The structure of basaltic scoria and reticulite and inferences for vesiculation, foam formation, and fragmentation in lava fountains," *J. Volcanol. Geotherm. Res.*, vol. 73, pp. 1–18, Sept. 1996.

[119] Mangan, M. T., Cashman, K. V., and Newman, S., "Vesiculation of basaltic magma during eruption," *Geology*, vol. 21, pp. 157–160, Feb. 1993.

[120] Mason, B., Pyle, D., and Oppenheimer, C., "The size and frequency of the largest explosive eruptions on earth," *Bull. Volcanol.*, vol. 66, no. 8, pp. 735–748, 2004.

[121] Mastin, L. G., "Insights into volcanic conduit flow from an open-source numerical model," *Geochem. Geophys. Geosys.*, vol. 3, no. 7, pp. 1–18, 2002.

[122] Matthews, S. J., Sparks, R. S. J., and Gardeweg, M. C., "The piedras grandes-soncor eruptions, Lascar volcano, Chile; evolution of a zoned magma chamber in the central andean upper crust," *J. Petrol.*, vol. 40, no. 12, pp. 1891–1919, 1999.

[123] McMillan, P. F., "Water solubility and speciation models," *Rev. Mineral. Geochem.*, vol. 30, no. 1, pp. 132–156, 1994.

[124] Minnis, P., Harrison, E., Stowe, L., Gibson, G., Denn, F., Doelling, D., and Smith, W., "Radiative climate forcing by the Mount Pinatubo eruption," *Science*, vol. 259, no. 5100, pp. 1411–1415, 1993.

[125] Müller, T. M. and Sahay, P. N., "Stochastic theory of dynamic permeability in poroelastic media," *Phys. Rev. E*, vol. 84, p. 026329, Aug. 2011.

[126] Navon, O., Chekhmir, A., and Lyakhovsky, V., "Bubble growth in highly viscous melts: theory, experiments, and autoexplosivity of dome lavas," *Earth Planet. Sci. Lett.*, vol. 160, no. 34, pp. 763–776, 1998.

[127] Nemchin, A. A., Giannini, L. M., Bodorkos, S., and Oliver, N. H. S., "Ostwald ripening as a possible mechanism for zircon overgrowth formation during anatexis: theoretical constraints, a numerical model, and its application to pelitic migmatites of the tickalara metamorphics, northwestern australia," *Geochim. Cosmochim. Acta*, vol. 65, no. 16, pp. 2771–2788, 2001.

[128] Newhall, C. G. and Self, S., "The volcanic explosivity index (VEI) — An estimate of explosive magnitude for historical volcanism," *J. Geophys. Res.: Oceans Atmos.*, vol. 87, no. NC2, pp. 1231–1238, 1982.

[129] Newman, S. and Lowenstern, J. B., "Volatilecalc: A silicate melt–H_2O–CO_2 solution model written in visual basic for excel," *Comput. Geosci.*, vol. 28, no. 5, pp. 597–604, 2002.

[130] Nguyen, C. T., Gonnermann, H. M., Chen, Y., Huber, C., Maiorano, A. A., Gouldstone, A., and Dufek, J., "Film drainage and the lifetime of bubbles," *Geochem. Geophys. Geosyst.*, vol. 14, pp. 3616–3631, Sept. 2013.

[131] Ni, H. and Zhang, Y., "H_2O diffusion models in rhyolitic melt with new high pressure data," *Chem. Geol.*, vol. 250, no. 1–4, pp. 68–78, 2008.

[132] Okumura, S., Nakamura, M., Takeuchi, S., Tsuchiyama, A., Nakano, T., and Uesugi, K., "Magma deformation may induce non-explosive volcanism via degassing through bubble networks," *Earth Planet. Sci. Lett.*, vol. 281, pp. 267–274, May 2009.

[133] Okumura, S., Nakamura, M., and Tsuchiyama, A., "Shear-induced bubble coalescence in rhyolitic melts with low vesicularity," *Geophys. Res. Lett.*, vol. 33, p. L20316, Oct. 2006.

[134] Okumura, S., Nakamura, M., Tsuchiyama, A., Nakano, T., and Uesugi, K., "Evolution of bubble microstructure in sheared rhyolite: Formation of a channel-like bubble network," *J. Geophys. Res.: Solid Earth*, vol. 113, no. B7, pp. n/a–n/a, 2008.

[135] Oppenheimer, C., Fischer, T. P., and Scaillet, B., *4.4 - Volcanic Degassing: Process and Impact*, pp. 111–179. Oxford: Elsevier, 2014.

[136] Ordonez-Miranda, J., Alvarado-Gil, J. J., and Yang, R., "Effective thermal conductivity of metal-dielectric composites at the non-dilute limit," *Int. J. Thermophys.*, vol. 33, pp. 2118–2124, Nov. 2012.

[137] Ordonez-Miranda, J. and Alvarado-Gil, J. J., "On the stability of the exact solutions of the dual-phase lagging model of heat conduction," *Nanoscale Res. Lett.*, vol. 6, p. 327, Dec. 2011.

[138] Ostwald, W., Bodenstein, M., Clusius, K., Bonhoeffer, K. F., and Falkenhagen, H., *Zeitschrift für physikalische Chemie*. Akademische Verlagsgesellschaft Geest & Portig, 1897. Google-Books-ID: WwhLAAAAYAAJ.

[139] Özişik, M. N. and Tzou, D. Y., "On the wave theory in heat conduction," *J. Heat Transfer*, vol. 116, pp. 526–535, Aug. 1994.

[140] Palais, J. M. and Sigurdsson, H., *Petrologic evidence of volatile emissions from major historic and pre-historic volcanic eruptions*, vol. 52 of *Geophys. Monogr. Ser.*, pp. 31–53. Washington, DC: AGU, 1989.

[141] Pallister, J. S., Hoblitt, R. P., Meeker, G. P., Knight, R. J., and Siems, D. F., *Magma mixing at mount pinatubo: Petrographic and chemical evidence from the 1991 deposits*, pp. 687–731. Philippine Institute of Volcanology and Seismology, 1996.

[142] Pallister, J. S., Hoblitt, R. P., and Reyes, A. G., "A basalt trigger for the 1991 eruptions of pinatubo volcano?," *Nature*, vol. 356, no. 6368, pp. 426–428, 1992.

[143] Papale, P., "Dynamics of magma flow in volcanic conduits with variable fragmentation efficiency and nonequilibrium pumice degassing," *J. Geophys. Res.: Solid Earth*, vol. 106, no. B6, pp. 11043–11065, 2001.

[144] Park, Y. and Hanson, B., "Experimental investigation of Ostwald-ripening rates of forsterite in the haplobasaltic system," *J. Volcanol. Geotherm. Res.*, vol. 90, no. 12, pp. 103–113, 1999.

[145] Parmigiani, A., Faroughi, S., Huber, C., Bachmann, O., and Su, Y., "Bubble accumulation and its role in the evolution of magma reservoirs in the upper crust," *Nature*, vol. 532, pp. 492–495, Apr. 2016.

[146] Parmigiani, A., Huber, C., Bachmann, O., and Chopard, B., "Pore-scale mass and reactant transport in multiphase porous media flows," *J. Fluid Mech.*, vol. 686, pp. 40–76, 2011.

[147] Pazdniakou, A. and Adler, P. M., "Dynamic permeability of porous media by the lattice Boltzmann method," *Adv. Water Resour.*, vol. 62, Part B, pp. 292–302, Dec. 2013.

[148] Pearce, N. J. G., Perkins, W. T., Westgate, J. A., Gorton, M. P., Jackson, S. E., Neal, C. R., and Chenery, S. P., "A compilation of new and published major and trace element data for NIST SRM 610 and NIST SRM 612 glass reference materials," *Geostand. Newsletter*, vol. 21, no. 1, pp. 115–144, 1997.

[149] Porta, G., Chaynikov, S., Riva, M., and Guadagnini, A., "Upscaling solute transport in porous media from the pore scale to dual- and multicontinuum formulations," *Water Resour. Res.*, vol. 49, pp. 2025–2039, Apr. 2013.

[150] Pozrikidis, C., *Boundary integral and singularity methods for linearized viscous flow*. Cambridge University Press, 1992.

[151] Pride, S., Tromeur, E., and G. Berryman, J., "Biot slow-wave effects in stratified rock," *Geophys.*, vol. 67, pp. 271–281, Jan. 2002.

[152] Prousevitch, A. A., Sahagian, D. L., and Anderson, A. T., "Dynamics of diffusive bubble growth in magmas: Isothermal case," *J. Geophys. Res.: Solid Earth*, vol. 98, no. B12, pp. 22283–22307, 1993.

[153] Proussevitch, A. and Sahagian, D., "Bubbledrive-1: A numerical model of volcanic eruption mechanisms driven by disequilibrium magma degassing," *J. Volcanol. Geotherm. Res.*, vol. 143, no. 1–3, pp. 89–111, 2005.

[154] Proussevitch, A. A. and Sahagian, D. L., "Dynamics and energetics of bubble growth in magmas: Analytical formulation and numerical modeling," *J. Geophys. Res.: Solid Earth*, vol. 103, no. B8, pp. 18223–18251, 1998.

[155] Pyle, D. M., Beattie, P. D., and Bluth, G. J. S., "Sulphur emissions to the stratosphere from explosive volcanic eruptions," *Bull. Volcanol.*, vol. 57, no. 8, pp. 663–671, 1996.

[156] Qian, Y. H., D'Humières, D., and Lallemand, P., "Lattice BGK models for Navier-Stokes equation," *EPL (Europhys. Lett.)*, vol. 17, no. 6, p. 479, 1992.

[157] Rallison, J. M., "Note on the time-dependent deformation of a viscous drop which is almost spherical," *J. Fluid Mech.*, vol. 98, pp. 625–633, June 1980.

[158] Read, W. G., Froidevaux, L., and Waters, J. W., "Microwave limb sounder measurement of stratospheric SO_2 from the Mt. Pinatubo volcano," *Geophys. Res. Lett.*, vol. 20, no. 12, pp. 1299–1302, 1993.

[159] Robock, A., "Cooling following large volcanic eruptions corrected for the effect of diffuse radiation on tree rings," *Geophys. Res. Lett.*, vol. 32, no. 6, p. L06702, 2005.

[160] Rust, A. C. and Manga, M., "Effects of bubble deformation on the viscosity of dilute suspensions," *J. Non-Newtonian Fluid Mech.*, vol. 104, pp. 53–63, Apr. 2002.

[161] Rutherford, M. J., Sigurdsson, H., Carey, S., and Davis, A., "The May 18, 1980, eruption of Mount St. Helens: 1. Melt composition and experimental phase equilibria," *J. Geophys. Res.: Solid Earth*, vol. 90, no. B4, pp. 2929–2947, 1985.

[162] Rutherford, M. J., "Magma ascent rates," *Rev. Mineral. Geochem.*, vol. 69, no. 1, pp. 241–271, 2008.

[163] Rutherford, M. J. and Hill, P. M., "Magma ascent rates from amphibole breakdown: An experimental study applied to the 1980–1986 Mount St. Helens eruptions," *J. Geophys. Res.: Solid Earth*, vol. 98, no. B11, pp. 19667–19685, 1993.

[164] S., M., "Chemistry of volcanic gases," *Bull. Volcanol. Soc. Japan*, vol. 20, 1975.

[165] Saal, A. E., Hauri, E. H., Langmuir, C. H., and Perfit, M. R., "Vapour undersaturation in primitive mid-ocean-ridge basalt and the volatile content of Earth's upper mantle," *Nature*, vol. 419, no. 6906, pp. 451–455, 2002.

[166] Satoh, H., Saito, G., Shinohara, H., and Yamaguchi, Y., "Sulfur source for the 1991-1995 unzen eruption: Evidence from melt inclusions in pyroxenes," *Geophys. Res. Lett.*, vol. 30, no. 23, 2003.

[167] Scaillet, B., Clemente, B., Evans, B. W., and Pichavant, M., "Redox control of sulfur degassing in silicic magmas," *J. Geophys. Res.: Solid Earth*, vol. 103, no. B10, pp. 23937–23949, 1998.

[168] Scaillet, B., Luhr, J. F., and Carroll, M. R., *Petrological and volcanological constraints on volcanic sulfur emissions to the atmosphere*, vol. 139, pp. 11–40. Washington, D. C.: American Geophysical Union, 2004.

[169] Scaillet, B. and MacDonald, R., "Experimental and thermodynamic constraints on the sulphur yield of peralkaline and metaluminous silicic flood eruptions," *J. Petrol.*, vol. 47, no. 7, pp. 1413–1437, 2006.

[170] Self, S., Gertisser, R., Thordarson, T., Rampino, M. R., and Wolff, J. A., "Magma volume, volatile emissions, and stratospheric aerosols from the 1815 eruption of Tambora," *Geophys. Res. Lett.*, vol. 31, no. 20, p. L20608, 2004.

[171] Self, S. and King, A. J., "Petrology and sulfur and chlorine emissions of the 1963 eruption of Gunung Agung, Bali, Indonesia," *Bull. Volcanol.*, vol. 58, no. 4, pp. 263–285, 1996.

[172] Self, S., Widdowson, M., Thordarson, T., and Jay, A. E., "Volatile fluxes during flood basalt eruptions and potential effects on the global environment: A deccan perspective," *Earth Planet. Sci. Lett.*, vol. 248, no. 1–2, pp. 518–532, 2006.

[173] Sharma, K., Blake, S., Self, S., and Krueger, A. J., "SO_2 emissions from basaltic eruptions, and the excess sulfur issue," *Geophys. Res. Lett.*, vol. 31, no. 13, p. L13612, 2004.

[174] Shaw, A., Hauri, E., Fischer, T., Hilton, D., and Kelley, K., "Hydrogen isotopes in Mariana arc melt inclusions: Implications for subduction dehydration and the deep-Earth water cycle," *Earth Planet. Sci. Lett.*, vol. 275, no. 1, pp. 138–145, 2008.

[175] Shaw, H. R., "Viscosities of magmatic silicate liquids; an empirical method of prediction," *Am. J. Sci.*, vol. 272, no. 9, pp. 870–893, 1972.

[176] Sheng, P. and Zhou, M.-Y., "Dynamic permeability in porous media," *Phys. Rev. Lett.*, vol. 61, pp. 1591–1594, Oct. 1988.

[177] Shinohara, H., "Excess degassing from volcanoes and its role on eruptive and intrusive activity," *Rev. Geophys.*, vol. 46, no. 4, p. RG4005, 2008.

[178] Sigurdsson, H., Carey, S., Palais, J. M., and Devine, J., "Pre-eruption compositional gradients and mixing of andesite and dacite magma erupted from nevado del ruiz volcano, colombia in 1985," *J. Volcanol. Geotherm. Res.*, vol. 41, no. 1–4, pp. 127–151, 1990.

[179] Simkin, T., "Terrestrial volcanism in space and time," *Ann. Rev. Earth Planet. Sci.*, vol. 21, pp. 427–452, 1993.

[180] Sisson, T. W. and Bacon, C. R., "Gas-driven filter pressing in magmas," *Geology*, vol. 27, no. 7, pp. 613–616, 1999.

[181] Smeulders, D. M. J., Eggels, R. L. G. M., and Dongen, M. E. H. V., "Dynamic permeability: reformulation of theory and new experimental and numerical data," *J. Fluid Mech.*, vol. 245, pp. 211–227, Dec. 1992.

[182] Sparks, R. S. J., "The dynamics of bubble formation and growth in magmas: A review and analysis," *J. Volcanol. Geotherm. Res.*, vol. 3, no. 12, pp. 1–37, 1978.

[183] Stein, D. J. and Spera, F. J., "Rheology and microstructure of magmatic emulsions: theory and experiments," *J. Volcanol. Geotherm. Res.*, vol. 49, pp. 157–174, Jan. 1992.

[184] Stenchikov, G. L., Kirchner, I., Robock, A., Graf, H.-F., Antua, J. C., Grainger, R. G., Lambert, A., and Thomason, L., "Radiative forcing from the 1991 Mount Pinatubo volcanic eruption," *J. Geophys. Res.: Atmos.*, vol. 103, no. D12, pp. 13837–13857, 1998.

[185] Stolper, E. and Newman, S., "The role of water in the petrogenesis of Mariana trough magmas," *Earth Planet. Sci. Lett.*, vol. 121, no. 34, pp. 293–325, 1994.

[186] Stone, H. A., "Dynamics of drop deformation and breakup in viscous fluids," *Annu. Rev. Fluid Mech.*, vol. 26, no. 1, pp. 65–102, 1994.

[187] Streck, M. J. and Wacaster, S., "Plagioclase and pyroxene hosted melt inclusions in basaltic andesites of the current eruption of Arenal volcano, Costa Rica," *J. Volcanol. Geotherm. Res.*, vol. 157, no. 1–3, pp. 236–253, 2006.

[188] Su, Y. and Huber, C., "The effect of non-linear decompression history on H_2O/CO_2 vesiculation in rhyolitic magmas," *J. Geophys. Res.: Solid Earth*, in press, DOI: 10.1002/2016JB013812, 2017.

[189] Su, Y., Huber, C., Bachmann, O., Zajacz, Z., Wright, H., and Vazquez, J., "The role of crystallization-driven exsolution on the sulfur mass balance in volcanic arc magmas," *J. Geophys. Res.: Solid Earth*, vol. 121, no. 8, pp. 5624–5640, 2016.

[190] Suga, S., "Numerical schemes obtained from lattice Boltzmann equations for advection diffusion equations," *Int. J. Modern Phys. C*, vol. 17, no. 11, pp. 1563–1577, 2006.

[191] Symonds, R. B., Rose, W. I., Bluth, G. J. S., and Gerlach, T. M., "Volcanic-gas studies; methods, results, and applications," *Rev. Mineral. Geochem.*, vol. 30, no. 1, pp. 1–66, 1994.

[192] Taran, Y. A., Pokrovsky, B., and Dubik, Y. M., "Isotopic composition and origin of water in andesitic magmas," in *Dokl. Acad. Sci. USSR*, vol. 304, pp. 440–443.

[193] Taylor, G. I., "The viscosity of a fluid containing small drops of another fluid," *Proc. Royal Soc. London A: Math. Phys. Eng. Sci.*, vol. 138, pp. 41–48, Oct. 1932.

[194] Terzaghi, K., "Plastic equilibrium in a semi-infinite mass with a plane surface," in *Theoretical Soil Mechanics*, pp. 26–41, John Wiley & Sons, Inc., 1943.

[195] Thordarson, T., Miller, D. J., Larsen, G., Self, S., and Sigurdsson, H., "New estimates of sulfur degassing and atmospheric mass-loading by the 934 AD Eldgjá eruption, Iceland," *J. Volcanol. Geotherm. Res.*, vol. 108, no. 1–4, pp. 33–54, 2001.

[196] Thordarson, T., Self, S., Óskarsson, N., and Hulsebosch, T., "Sulfur, chlorine, and fluorine degassing and atmospheric loading by the 1783–1784 AD Laki (Skaftár Fires) eruption in Iceland," *Bull. Volcanol.*, vol. 58, no. 2–3, pp. 205–225, 1996.

[197] Toramaru, A., "BND (bubble number density) decompression rate meter for explosive volcanic eruptions," *J. Volcanol. Geotherm. Res.*, vol. 154, no. 3–4, pp. 303–316, 2006.

[198] Toramaru, A., "Vesiculation process and bubble size distributions in ascending magmas with constant velocities," *J. Geophys. Res.: Solid Earth*, vol. 94, no. B12, pp. 17523–17542, 1989.

[199] Toramaru, A., "Numerical study of nucleation and growth of bubbles in viscous magmas," *J. Geophys. Res.: Solid Earth*, vol. 100, pp. 1913–1931, Feb. 1995.

[200] Traversi, R., Becagli, S., Castellano, E., Marino, F., Rugi, F., Severi, M., Angelis, M. d., Fischer, H., Hansson, M., Stauffer, B., Steffensen, J. P., Bigler, M., and Udisti, R., "Sulfate spikes in the deep layers of EPICA-Dome C ice core: Evidence of glaciological artifacts," *Environ. Sci. Tech.*, vol. 43, no. 23, pp. 8737–8743, 2009.

[201] Tripathi, M. K., Sahu, K. C., and Govindarajan, R., "Dynamics of an initially spherical bubble rising in quiescent liquid," *Nature Comm.*, vol. 6, p. 6268, 2015.

[202] Ueda, A. and Itaya, T., "Microphenocrystic pyrrhotite from dacite rocks of Satsuma-Iwojima, southwest Kyushu, Japan and the solubility of sulfur in dacite magma," *Contrib. Mineral. Petrol.*, vol. 78, no. 1, pp. 21–26, 1981.

[203] Verhoogen, J., "Mechanics of ash formation," *Am. J. Sci.*, vol. 249, no. 10, pp. 729–739, 1951.

[204] Vernotte, P., "Les paradoxes de la théorie continue de l'équation de la chaleur," *Comptes Rendus de l'Académie des Sciences*, vol. 246, pp. 3154–3155, 1958.

[205] Wagner, C., "Theorie der Alterung von Niederschlägen durch Umlösen (Ostwald-Reifung)," *Zeitschrift fr Elektrochemie, Berichte der Bunsengesellschaft fr physikalische Chemie*, vol. 65, pp. 581–591, Sept. 1961.

[206] Wallace, P. J., "Volcanic SO_2 emissions and the abundance and distribution of exsolved gas in magma bodies," *J. Volcanol. Geotherm. Res.*, vol. 108, no. 1–4, pp. 85–106, 2001.

[207] Wallace, P. J., "Volatiles in subduction zone magmas: Concentrations and fluxes based on melt inclusion and volcanic gas data," *J. Volcanol. Geotherm. Res.*, vol. 140, no. 1–3, pp. 217–240, 2005.

[208] Watson, E. B., "Diffusion in volatile-bearing magmas," *Rev. Mineral. Geochem.*, vol. 30, no. 1, pp. 371–411, 1994.

[209] Westrich, H. R., Eichelberger, J. C., and Hervig, R. L., "Degassing of the 1912 katmai magmas," *Geophys. Res. Lett.*, vol. 18, no. 8, pp. 1561–1564, 1991.

[210] Westrich, H. R. and Gerlach, T. M., "Magmatic gas source for the stratospheric SO_2 cloud from the June 15, 1991, eruption of Mount Pinatubo," *Geology*, vol. 20, no. 10, pp. 867–870, 1992.

[211] Whitney, J. A. and Stormer, J. C., "Igneous sulfides in the fish canyon tuff and the role of sulfur in calc-alkaline magmas," *Geology*, vol. 11, no. 2, pp. 99–102, 1983.

[212] Wilke, M., Jugo, P. J., Klimm, K., Susini, J., Botcharnikov, R., Kohn, S. C., and Janousch, M., "The origin of S4+ detected in silicate glasses by XANES," *Am. Mineral.*, vol. 93, no. 1, pp. 235–240, 2008.

[213] Wolf-Gladrow, D. A., *Lattice-gas cellular automata and lattice Boltzmann.* Springer, 2005.

[214] Wong, T., Wielicki, B. A., Lee, R. B., Smith, G. L., Bush, K. A., and Willis, J. K., "Reexamination of the observed decadal variability of the Earth radiation budget using altitude-corrected ERBE/ERBS nonscanner WFOV data," *J. Climate*, vol. 19, no. 16, pp. 4028–4040, 2006.

[215] Wright, H. M., Folkes, C. B., Cas, R. A. F., and Cashman, K. V., "Heterogeneous pumice populations in the 2.08-Ma Cerro Galán Ignimbrite: Implications for magma recharge and ascent preceding a large-volume silicic eruption," *Bull. Volcanol.*, vol. 73, no. 10, pp. 1513–1533, 2011.

[216] Wright, H. M., Bacon, C. R., Vazquez, J. A., and Sisson, T. W., "Sixty thousand years of magmatic volatile history before the caldera-forming eruption of Mount Mazama, Crater Lake, Oregon," *Contrib. Mineral. Petrol.*, vol. 164, no. 6, pp. 1027–1052, 2012.

[217] Yamada, K., Emori, H., and Nakazawa, K., "Time-evolution of bubble formation in a viscous liquid," *Earth Planets Space*, vol. 60, no. 6, pp. 661–679, 2008.

[218] Yang, Z., Peng, X.-F., Lee, D.-J., and Chen, M.-Y., "An image-based method for obtaining pore-size distribution of porous media," *Environ. Sci. Tech.*, vol. 43, pp. 3248–3253, May 2009.

[219] York, D., "Least squares fitting of a straight line with correlated errors," *Earth Planet. Sci. Lett.*, vol. 5, pp. 320–324, Jan. 1968.

[220] Zajacz, Z., Candela, P. A., Piccoli, P. M., and Sanchez-Valle, C., "The partitioning of sulfur and chlorine between andesite melts and magmatic volatiles and the exchange coefficients of major cations," *Geochim. Cosmochim. Acta*, vol. 89, pp. 81–101, 2012.

[221] Zajacz, Z., Candela, P. A., Piccoli, P. M., Sanchez-Valle, C., and Wälle, M., "Solubility and partitioning behavior of Au, Cu, Ag and reduced S in magmas," *Geochim. Cosmochim. Acta*, vol. 112, pp. 288–304, 2013.

[222] Zellmer, G. F., Edmonds, M., and Straub, S. M., "Volatiles in subduction zone magmatism," *Geological Society, London, Special Publications*, vol. 410, no. 1, pp. 1–17, 2015.

[223] Zhang, Y., "A criterion for the fragmentation of bubbly magma based on brittle failure theory," *Nature*, vol. 402, no. 6762, pp. 648–650, 1999.

[224] Zhang, Y., Ni, H., and Chen, Y., "Diffusion data in silicate melts," *Rev. Mineral. Geochem.*, vol. 72, no. 1, pp. 311–408, 2010.

[225] Zhang, Y., Xu, Z., Zhu, M., and Wang, H., "Silicate melt properties and volcanic eruptions," *Rev. Geophys.*, vol. 45, no. 4, 2007.

[226] Zielinski, G. A., "Stratospheric loading and optical depth estimates of explosive volcanism over the last 2100 years derived from the greenland ice sheet project 2 ice core," *J. Geophys. Res.: Atmos.*, vol. 100, no. D10, pp. 20937–20955, 1995.

[227] Zou, Q., "On pressure and velocity boundary conditions for the lattice Boltzmann BGK model," *Phys. Fluids*, vol. 9, pp. 1591–1598, June 1997.